THESIS

EULERIAN AND LAGRANGIAN ANALYSES OF BIOAEROSOL TRANSPORT IN THREE DEEP CONVECTIVE STORM MORPHOLOGIES

Submitted by

Charles M. Davis

Department of Atmospheric Science

In partial fulfillment of the requirements

For the Degree of Master of Science

Colorado State University

Fort Collins, Colorado

Spring 2025

Master's Committee:

Advisor: Susan C. van den Heever

Sonia M. Kreidenweis
Shantanu Jathar

ABSTRACT

EULERIAN AND LAGRANGIAN ANALYSES OF BIOAEROSOL TRANSPORT IN THREE DEEP CONVECTIVE STORM MORPHOLOGIES

In this thesis, we investigate the entrainment and transport of aerosol particles in a representative isolated deep convective storm, supercell, and squall line using idealized high-resolution mesoscale model simulations. We focus our investigation on the extent to which air from rainy surface regions, which have been noted in the literature to be sites of aerosolization of biological particles, is able to enter and subsequently be transported within these storm morphologies. We also investigate the residence time in supersaturated environments experienced by these parcels as they are entrained.

The first part of this study quantifies the magnitude and timing of entrainment of air from the surface, and from rainy surface regions specifically, in all three storm morphologies. We use inert tracer quantities to constrain the timing with which rainy (referred to as rain-sourced tracers) and other surface air (referred to as fixed-source tracers) is entrained into the storms, and the fraction of each storm's updraft that is composed of air from these regions. At its peak, the isolated convective storm entrains the greatest proportion of surface-based air seen in any of the storms. However, it also attains the smallest concentrations of rain-sourced tracer and the smallest proportion of rain-sourced tracer in its updraft, indicating that significantly less of its entrained surface air originates in regions of potential rain-induced aerosolization of bioaerosols. The squall line and supercell attain greater values of both these quantities and sustain them for longer periods, indicating that more air in their updrafts originates in rainy regions. For light rain

(>= 1 mm/hr), the squall line and supercell entrain comparable concentrations of air from rainy regions, but for heavy rain (>= 40 mm/hr) the squall line entrains significantly more.

The second part of this work investigates the specific pathways by which surface air is entrained into these storms as well as the environments experienced by entrained surface-based air parcels. We do this by calculating parcel trajectories using the output of the aforementioned mesoscale simulations, initializing air parcels at various times within each storm's life cycle, and separately evaluating the trajectories of parcels originating in rainy and non-rainy regions. The isolated convective storm simply moves over and entrains the parcels not initialized in rainy regions into its updraft directly by its strong surface convergence. The squall line and supercell entrain non-rainy parcels by gust-front lofting, in which the circulation at the leading edge of the cold pool lofts the parcels to a level at which they can be entrained by the updraft behind the gust front. The isolated convective storm entrains parcels originating in rainy regions via the horizontal vortical circulation in the head of the cold pool, which lofts them and redirects them towards the updraft. The squall line also entrains rainy parcels by this same circulation in its cold pool. The supercell, on the other hand, entrains rainy parcels from a relatively narrow region within and just outside of the leading edge of the forward-flank downdraft's cold pool via a combination of gust front lofting and the known phenomenon of the "recycling" of some negatively buoyant air from the forward-flank downdraft's cold pool into its updraft.

We find that the time these entrained parcels spend in supersaturated environments is a strong function of storm morphology. Parcels entrained into the squall line spend nearly twice as long on average in supersaturated regions as entrained parcels in the other two storm types. This arises because the squall line parcels take longer to reach mid-levels after first being lofted by the circulation in the head of the cold pool. This longer transit time is due to the upshear tilt of the

updraft, as well as from more complex 3D variations in the structure of the gust front and updraft.

ACKNOWLEDGEMENTS

I am deeply appreciative of my advisor Sue van den Heever's support throughout this project and for her thoughtful and comprehensive feedback, which was invaluable during the writing process. I would also like to thank the other members of my committee, Sonia Kreidenweis and Shantanu Jathar, for their time and generosity in serving on my committee. I am very grateful to current and former members of the van den Heever group, who have aided me at every step of this project, whether with technical expertise or moral support: Steve Saleeby, Dr. Leah Grant, Dr. Peter Marinescu, Dr. Brenda Dolan, Dr. Rick Schulte, Dr. Randy Chase, Dr. IT Singh, Dr. Jennie Bukowski, Dr. Sean Freeman, Nick Falk, Bee Leung, Christine Neumaier, Ben Ascher, Rachael Auth, and Phoebe Lin. The experience of working on the BACS-II field campaign was integral to my development as a scientist, and I'm very appreciative of all of the members of the BACS-II drones and sondes teams not already mentioned—Jacob Escobedo, Allie Mazurek, Tyler Barbero, Bryan Heffernan, Dr. Marina Nieto-Caballero, and Lexi Sherman—as well as to Dr. Leah Grant for leading such a successful and enjoyable campaign. I would like to thank Tom Gowan for the use of his trajectory code, and to acknowledge NSF funding from grants #AGS-2105938, #AGS-2019947, and #DE-SC0021160. I am profoundly grateful for the support and camaraderie of my friends and family, as well as that of my peers in the Atmospheric Science program.

TABLE OF CONTENTS

Chapter 1 INTRODUCTION

Aerosols exert significant microphysical and radiative impacts across spatial and temporal scales ranging from those of the global climate (e.g. Lohmann and Feichter 2005) to those of individual storms (e.g. Tao et al. 2012; Stier et al. 2024). Aerosol-cloud interactions are traditionally described as either direct or indirect effects (Charlson et al. 1992; Penner et al. 2001). Aerosol direct effects refer to the explicit interaction of aerosol particles with radiation and include scattering, absorption, and emission of both shortwave and longwave radiation (Ångström 1929; Flowers et al. 1969; Coakley et al. 1983; Charlson et al. 1992). Aerosol indirect effects refer to the ability of aerosol particles to influence microphysical processes by acting as cloud-condensation nuclei (CCN) and/or ice-nucleating particles (INP), with subsequent impacts on the dynamic, precipitation and radiative processes and properties of clouds. The transport and distribution of aerosols within storms is integral to the microphysical activity of these particles, and hence the aerosol indirect effects (e.g. Andreae et al. 2004; Khain and Pokrovsky 2004; van den Heever et al. 2006). The transport of these aerosol particles within deep convective systems, and the transport of aerosolized biological particles in particular, forms the focus of this thesis.

1.1 Aerosol impacts on deep convective clouds

The full range of mechanisms by which aerosol-induced microphysical processes impact convective storms is a topic of some debate (Tao et al. 2012; Stier et al. 2024), and is also known to vary between storm morphologies (Tao et al. 2007; van den Heever et al. 2011). One of the earliest hypothesized, and later observed, aerosol-cloud interactions is a shift in the droplet size distribution of polluted (i.e. aerosol-rich) warm-phase clouds from a smaller number of larger

drops to a larger number of smaller drops for the same liquid water content (Twomey and Squires 1959). Such a shift in the droplet size distribution occurs because, under atmospheric conditions, cloud droplets require the presence of a cloud-condensation nucleus (CCN) for their formation (Aitken 1881; Köhler 1936; Pruppacher and Klett 2010). Thus, the introduction of greater concentrations of CCN shifts the droplet size distribution towards fewer and smaller droplets when a constant amount of water vapor is condensed. This effect is referred to as the Twomey effect. It is known to affect warm clouds by increasing albedo (Twomey 1977), as well as by suppressing warm rain formation and thereby extending the lifetime of the cloud (Albrecht 1989).

The effects of aerosol-cloud interaction in deep convective clouds (DCCs) are more complex than those of warm-phase shallow clouds because DCCs have mixed- and ice-phase regions, which significantly broaden the range of aerosol-induced microphysical processes and feedbacks at play. As such, the nature of aerosol-cloud interactions in DCCs depends on many factors including humidity (Fan et al. 2007; Khain et al. 2008; Grant and van den Heever 2014, 2015), wind shear (Fan et al. 2007; Lee et al. 2008; Khain et al. 2008; Fan et al. 2009), CAPE (Lee et al. 2008; Storer et al. 2010, 2014), and storm morphology (Wang 2005; van den Heever et al. 2006; Tao et al. 2007; van den Heever et al. 2011; Grant and van den Heever 2015). One area of research into aerosol-DCC interactions has investigated the effects of increased and/or spatially shifted latent heat release as a result of the introduction of more CCN/INPs. This additional latent heat release is proposed to invigorate updrafts in both liquid and mixed-phase clouds by enhancing the updraft buoyancy. The former, often referred to as “condensation invigoration” or “warm-phase invigoration”, is proposed to happen by virtue of the fact that a constant mass of water condensed into a large number of small droplets has a greater collective

surface area than the same mass of water condensed into a small number of larger droplets. Thus, in more polluted environments more water vapor is condensed into liquid water, thereby releasing more latent heat (Wang 2005; Seigel and van den Heever 2012; Seigel et al. 2013; Koren et al. 2014; Seiki and Nakajima 2014; Saleeby et al. 2015; Sheffield et al. 2015; Fan et al. 2018). In mixed- and ice-phase clouds, "cold-phase invigoration" of convective updrafts would occur by virtue of smaller droplets not precipitating out as readily as larger droplets, thus allowing more liquid water to be transported to higher altitudes where it can freeze and release the latent heat of fusion (Andreae et al. 2004; Khain et al. 2005; van den Heever et al. 2006; Rosenfeld et al. 2008; Fan et al. 2013; Storer and van den Heever 2013). However, the viability of cold phase-invigoration and the practical importance of warm-phase invigoration are both subjects of ongoing debate and investigation (Lebo 2014; Grabowski 2015, 2018; Varble 2018; Igel and van den Heever 2021; Marinescu et al. 2021; Romps et al. 2023; Varble et al. 2023). Nonetheless, while the range of mechanisms by which they do so is not a settled question, the fact that the presence of a larger number of CCN does affect the microphysics (and, subsequently, dynamics and radiative response) of deep convective storm systems is well-demonstrated in the literature.

Another mechanism by which aerosols in the atmosphere exert microphysical influence on clouds is by acting as ice-nucleating particles (INPs). Supercooled liquid water in the atmosphere will remain in the liquid phase at temperatures warmer than about -38°C in the absence of an ice-nucleating particle (INP) (Mendenhall and Ingersoll 1908; Vonnegut 1948; Vali 1971; DeMott et al. 1997, 1998, 2010; Pruppacher and Klett 2010; Kanji et al. 2017). INPs are generally sparse throughout the atmosphere, with observed concentrations ranging from about 0.1 to 500 L^{-1} in the free troposphere, and estimates of the proportion of the global aerosol

population that can act as INP ranging from <1-30 particles per million (Rogers et al. 1998; DeMott et al. 2003a, 2010, 2011). However, only a small number of ice crystals are initially required to glaciate an entire cloud; this results from the fact that the saturation vapor pressure over ice is lower than that over water at all temperatures below 0°C, and so ice crystals grow via deposition at the expense of liquid water via the so-called Wegener-Bergeron-Findeisen process (Findeisen 1938; Korolev and Isaac 2003; Korolev 2007; Pinsky et al. 2014). Additionally, "ice multiplication" can occur in clouds via a set of mechanisms known collectively as secondary ice production (SIP), which is thought to be of atmospheric significance in that it explains long-observed discrepancies between concentrations of ice crystals and INPs in clouds (Koenig 1963; Mossop et al. 1970; Hallett and Mossop 1974; Mossop 1985; Korolev et al. 2004; Pinsky et al. 2014; Lawson et al. 2015; DeMott et al. 2016) In this way, a small number of INPs can have decisive effects on the development of a single cloud or storm. Additionally, some types of aerosols, including mineral dust, can act as both a CCN (Twohy et al. 2009) and an INP (DeMott et al. 2003b; Twohy and Poellot 2005). The effects of ice nucleation are far ranging, impacting processes ranging from radiative transfer and cloud electrification to the chemistry of the troposphere (Kanji et al. 2017). Ice nucleation is also significant for weather and climate by virtue of the fact that most precipitation on earth is initiated in the ice phase (Lau and Wu 2003).

1.2 Microphysical characteristics and emission mechanisms of bioaerosols

There are many different types of aerosolized particles (i.e. solid particles that have been made airborne) in the earth's atmosphere, and biological aerosol particles comprise a significant fraction of the earth's total aerosol burden (Jaenicke 2005). Several types of biological particles are known to have subsets that are microphysically active, including pollen (Pope 2010), bacteria

(Franc and DeMott 1998), and fungi (Fröhlich-Nowoisky et al. 2015). These particles can be microphysically active in the warm phase, acting as CCN (Ariya et al. 2009; Sun and Ariya 2006), and some may also act as INPs (Morris et al. 2004; Creamean et al. 2013; Akila et al. 2018; Creamean et al. 2018; McCluskey et al. 2018; Creamean et al. 2019). However, the microphysical impact of bioaerosols is not only from the addition of more INPs to the atmosphere, but also from the temperatures at which these particles are able to nucleate ice.

Different types of particles that act as INPs have different temperatures at which they become "ice-active", i.e. able to nucleate ice. Mineral dust is typically thought to be the most significant ice-active particle because it has very large terrestrial emission rates and is generally effective at nucleating ice (DeMott et al. 2003b; Twohy and Poellot 2005; DeMott et al. 2010; Koehler et al. 2010; Corr et al. 2016; Kanji et al. 2017). However, the temperature at which mineral dust is able to nucleate ice depends on many factors including composition and particle size, and many dust particles only become ice-active at temperatures below about -15°C (Hoose and Möhler 2012). Bioaerosols, on the other hand, are known to be the most ice-active class of particles in that they are able to nucleate ice at the warmest temperatures (Després et al. 2012; Hoose and Möhler 2012; Joly et al. 2014; Morris et al. 2014). This characteristic means that the presence of a small number of bioaerosols has, in theory, the potential to initiate the glaciation of a cloud at significantly warmer conditions than those at which it would otherwise freeze, with subsequent impacts upon the development of convective systems via the aerosol-cloud interactions previously discussed.

It is well-documented in the literature that rainfall events can cause sharp increases in the concentration of ice-nucleating particles in their vicinity, with the earliest observations of this phenomenon dating back to at least 1966 (Isono and Tanaka 1966). More recent studies have

demonstrated that this increase may be primarily composed of bioaerosols (Huffman et al. 2013), which has been established both through observing the particles' freezing temperature dependence and its change with treatments intended to deactivate biological particles (Testa et al. 2021) and through culturing of air samples (Heo et al. 2014). This increase in the concentration of ice-active biological particles is thought to be due to their aerosolization by rain through several mechanisms:

- Tiny bubbles are formed inside a raindrop as it strikes soil; these bubbles then burst when they reach the air-droplet interface, ejecting very small droplets which contain bacteria from the soil (Joung et al. 2017)
- Raindrops striking plant leaves can aerosolize plant detritus (Tobo et al. 2013) and/or fungal spores (Jones and Harrison 2004)
- The high humidity associated with rain events can cause pollen grains to rupture into sub-pollen particles by osmotic pressure (Hughes et al. 2020; Stone et al. 2021)

While these specific aerosolization mechanisms have been identified, neither the emission mechanisms of bioaerosols in general, nor the fluxes produced by these mechanisms, are well-described as yet (Xie et al. 2020). However, soil is known to be the leading terrestrial source of aerosolized biological particles (Xie et al. 2020), and so there is ample reason to investigate the transport and subsequent microphysical effects of the bioaerosols it produces.

Previous research on the topic of bioaerosol-cloud interactions has found conflicting evidence for the influence of bioaerosols on convective storms in practice. Diehl et al. (2002) introduced pollen into a vertical wind chamber containing supercooled water and found that it nucleated ice at warm temperatures. Wozniak et al. (2018) simulated pollen and the rupture of pollen into subpollen particles (SPPs) in a regional model and found significant precipitation

suppression by the aforementioned Twomey effect under clean continental background conditions as a result of the SPPs' nucleation activity. By contrast, Patade et al. (2022) found that bioaerosols' influence on ice concentrations in a simulated squall line was minimal compared to the contributions of homogeneous nucleation, secondary ice production, and the sedimentation of ice crystals to lower and warmer vertical levels where the potential contributions of bioaerosols as INP are thought to be most significant. Hoose et al. (2010) found that bioaerosols did not contribute meaningfully to ice concentrations in a global climate model integrated for five years of simulation time, while noting that this does not imply that bioaerosols cannot meaningfully influence ice nucleation at smaller spatial or temporal scales.

Thus, the lack of consensus as to the ability of bioaerosols to influence storms and the developing understanding of their rain-induced aerosolization mean that there are many open questions that hinge on these topics. Our focus in this thesis will be on the transport of these particles in deep convective storms. We now outline our understanding of aerosol transport in DCCs generally before examining existing work on the transport of bioaerosols specifically.

1.3 Aerosol transport in deep convective storms

The origins of the air and particles that are entrained into convective updrafts and storms has been a longstanding area of research. Riehl and Malkus (1958) proposed the "hot tower hypothesis" nearly 70 years ago, arguing that the ascending branch of the Hadley cell was driven by undiluted convective cores in the ITCZ that transported energy-rich air from the boundary layer to the upper troposphere and, subsequently, poleward. The advent of high-resolution cloud-resolving and mesoscale models has greatly facilitated the investigation of such questions related to the origins of air in convection and other settings, particularly through the calculation of

trajectories that use the wind field to determine the origin or destination of a parcel of air. Fierro et al. (2009) used such an approach to investigate the hot tower hypothesis, finding that this transport does indeed occur, but that the convective cores themselves are significantly diluted. They also demonstrated that more than half of the parcels initialized in the boundary layer ahead of a mature maritime squall line are lofted to at least 10 km MSL, with the primary entrainment pathway being gust front lofting into the storm's updraft. Applying a similar Lagrangian analysis of parcel trajectories in a simulation of a tropical deep convective squall line, McGee and van den Heever (2014) determined that the air in the strongest regions of the convective updrafts originates near the surface, but that most of the air that is lifted to altitudes of 10 km or more originates more than 2 km above the surface.

Research has also been conducted to understand not only the origins of entrained air in convection, but the specific pathways by which aerosols are entrained into deep convective storms. Particular emphasis within this body of work has been placed on the transport of dust. Seigel and van den Heever (2012) analyzed the pathways by which dust is entrained into a simulated supercell under several different dust emission scenarios. They found that significant concentrations of dust are entrained into the storm's updraft via gust front lofting when the dust originated ahead of the cold pool (i.e. in a dusty background environmental state), but that minimal dust is entrained into the storm's updraft when its only emission mechanism is lofting by the surface winds associated with the storm's cold pool. This is despite the fact that large concentrations of dust are lofted into the cold pool itself; the dynamics of the storm are such that the dust in the cold pool can only be in entrained into the updraft when it is first detrained from a small region at the head of the cold pool by turbulent mixing, which only occurs in small quantities. Low-level entrainment has also been investigated in shallow convective clouds.

Hoffmann et al. (2015) investigate the question of aerosol entrainment in a simulation of a shallow cumulus cloud using Lagrangian aerosols that can be tracked individually and find that most activated aerosols are entrained by the updraft at cloud base, rather than through lateral entrainment at higher levels.

Other research on convective aerosol transport has focused on the ultimate destination of particles transported by DCCs, rather than the initial entrainment of these particles. Tulet et al. (2010) used a mesoscale model to simulate an observed mesoscale convective system (MCS) over Niger and found that MCSs can transport dust aerosols to the tropopause in concentrations up to 6 particles/cm^3. They also found that the inclusion of wet dust scavenging processes in their model reduced dust concentrations in convective cores from 50 $\mu g/m^3$ to less than 1 $\mu g/m^3$. Herbener et al. (2016) similarly found that a tropical cyclone's convective updraft transports dust to the upper troposphere, but that 75x as much dust is returned to the surface via wet and dry deposition as is transported to the upper troposphere. These findings will be important for contextualizing our results; we find that a portion of both the tracers and trajectories we simulate reach the upper troposphere, but they are not subject to these processes.

A few recent modeling studies of bioaerosol-cloud interactions and transport are especially relevant to the aims of this thesis. Subba et al. (2023) modeled the transport of pollen and SPPs in a case study of a strong convective event in the Great Plains by coupling a pollen aerosol module and emission model (Zhang and Steiner 2022) to the Weather Research and Forecasting Model with Chemistry (WRF-Chem) (Grell et al. 2005). While this study describes some broad pathways taken by bioaerosols in the simulated storm, their horizontal grid spacing of 12 km is too coarse to properly resolve smaller-scale storm dynamic mechanisms such as gust-front lofting, entrainment, or turbulence, if they are resolved at all. The question of the

specific mechanisms by which these particles are entrained into the simulated storm was not the focus of the Subba et al. (2023) study and remains unanswered. Additionally, while the bioaerosols simulated in this study are microphysically active, they are not treated as INP and thus only directly influence the warm-phase microphysics of the storm. As bioaerosols are thought to function as warm-temperature INPs as previously outlined, a potentially significant microphysical impact of these particles is not simulated in this study.

Zhang et al. (2024) built upon the work of Subba et al. (2023) by analyzing the microphysical impacts of pollen and SPPs in a case study of the same convective event. A key component of this simulation is the introduction of an ice nucleation activity parameterization for pollen and SPPs that is derived from lab observations of their freezing activity at different temperatures and via different heterogeneous ice nucleation mechanisms (Matthews et al. 2023). This allows for the simulation of pollen and SPPs as ice-nucleating particles, rather than only as CCN. The authors found that the introduction of SPPs, in particular, has significant impacts on the liquid- and ice-water paths as well as on the precipitation characteristics of the system. This study focuses on the bulk/storm-averaged impacts of the introduction of these particles on the convective system, and not on identifying the pathways by which these particles are entrained from the surface into the storm itself. Additionally, the simulation in this study was run at 3km horizontal grid spacing with an 18s model timestep, both of which are too coarse to analyze the transport pathways of the simulated pollen and SPPs within an individual storm. The authors did find that the inclusion of pollen and SPPs has significant microphysical impacts on the storm they simulate.

Finally, Werchner et al. (2022) also conducted a case study simulation with pollen emission and a parameterization of its microphysical effects, but at the spatially and temporally

larger scale of continental Europe for a 10-day period. The authors find small but statistically significant shifts in the spatial distribution and size distributions of ice and cloud droplets as a result of the inclusion of SPPs as ice-nucleating aerosols. This study's focus is on the effect of the inclusion of a pollen rupturing mechanism in an operational weather model, rather than on the transport dynamics of pollen and SPPs in individual storms.

While this thesis is primarily concerned with the transport of bioaerosols for its implications on the atmosphere, the transport of these particles also has repercussions for human health. The phenomenon of thunderstorm asthma, in which previously healthy people experience acute respiratory distress during and after a thunderstorm, is thought to be driven by pollen grains being lofted by updrafts in the early stages of a thunderstorm, rupturing into SPPs in the high humidity of a cloud, and then returning to a concentrated layer at the earth's surface via the storm's downdrafts (Packe and Ayres 1985; Newson et al. 1997; D'Amato et al. 2016). This pathway is required to cause respiratory distress because pollen grains themselves are too large to penetrate the lower respiratory tract, while SPPs are small enough to do so (Taylor et al. 2002). Thus, we note that the findings of this thesis on the pathways and humidity environments experienced by air carrying biological aerosols may have further epidemiological implications, though we do not explicitly investigate these implications in this study.

In summary, as the existing evidence for bioaerosol influence on convective storms is conflicting, and as questions of the transport of bioaerosols within such storms have not been fully addressed, it is worth understanding their transport both for its own sake and for its contribution to understanding bioaerosol-cloud interactions. This thesis builds upon the existing literature on deep convective aerosol transport by extending our understanding of these storm-

scale entrainment and transport dynamics to bioaerosols, which, to our knowledge, has not previously been assessed.

1.4 Thesis outline and objectives

The overarching objective of this thesis is to investigate the entrainment and transport of air containing rain-aerosolized biological particles and other surface air in three different deep convective storm morphologies. More specifically, we seek to expand our current understanding of this transport in two ways. First, we quantify the entrainment of surface air, including the timing of its entrainment into each storm and its subsequent spatial and temporal distribution. While some of the aforementioned studies have investigated the origins of entrained air in DCCs, no estimates have been made of their entrainment of air bearing rain-aerosolized biological particles, nor that of rainy surface air more generally. We also compare these entrainment results directly between storm morphologies using a uniform methodology, which has not been done before. Second, we characterize the transport of this air by investigating the pathways by which it is entrained into each storm, as well as the air's destination once entrained. If the preceding analytical approach answers the "where", "when", and "how much" of the entrainment of this air, this approach allows us to also answer the "how". While conceptual descriptions of these pathways exist for some entrainment mechanisms in DCCs, we not only outline differences in entrainment pathways between those of surface air in general and those of rainy surface air specifically, but we also characterize the supersaturation experienced by parcels as they are entrained in each pathway. As with our quantification of the entrainment of this air, previous investigations into these pathways have not compared them directly between storm morphologies using a uniform methodology.

To achieve the first of these goals, we measure the transport of passive tracers in idealized storm simulations to quantify the extent to which surface air, and in particular air originating in surface regions where rain may be aerosolizing biological particles, is entrained into different storm types. We implement two tracer emission mechanisms to track both surface air in general and air from rainy regions specifically. The passive tracer methodology we utilize (discussed fully in the next section) allows us to not only measure concentrations and transport of air containing rain-aerosolized biological particles in each storm, but also to calculate storm-averaged quantities that explain these phenomena in terms of physical storm processes. To address the second goal question outlined above, we calculate trajectories of parcels from the surface to visualize and describe the pathways by which this entrainment occurs in a spatiotemporal, as well as a microphysical, sense. These parcel trajectories not only elucidate the pathways taken by entrained parcels, but they also allow us to differentiate the factors separating parcels that are and are not entrained. Finally, by applying these Eulerian and Lagrangian approaches together to the dynamics of three distinct deep convective storm morphologies, we gain a clearer picture of the importance of different convective morphologies in the transport of surface air in general and bioaerosol-rich surface air in particular.

We hypothesize first that the supercell will be able to entrain the most air from potentially bioaerosol-rich rainy regions (on a per-area of rainy region basis).. The re-entrainment of rain-cooled air from the forward-flank downdraft is a known mechanism of supercells, which can lift some of this negatively buoyant air because their updrafts are so strongly dynamically forced (Rotunno and Klemp 1985). It is not clear *a priori* how or to what degree the isolated convective storm and squall line entrain rainy air, which is negatively buoyant and therefore more difficult for the storm to loft. Second, we hypothesize that the three

storms we simulate, all having significantly different dynamics, will have significantly different mechanisms by which they entrain surface air, and that these mechanisms will differ between air from rainy and non-rainy regions.

Chapter 2 METHODS

Throughout this work we will use the convention of t=100 minutes, for example, to refer to the point in time 100 minutes after the start of the simulation, or t=100-105 minutes to refer to the period of time from 100 to 105 minutes after the start of the simulation. Likewise, z=5 km indicates 5 km AGL, and z=0-1 km indicates the layer from 0 km to 1 km AGL. All altitudes are given as AGL throughout this study.

2.1 Idealized model setup

To achieve our stated goals, we conduct a suite of idealized simulations using the Regional Atmospheric Modeling System (RAMS) version 6.3.04 (Cotton et al. 2003; Saleeby and van den Heever 2013; van den Heever et al. 2022). We simulate well-established representations of three deep convective storm morphologies: an isolated convective storm, a squall line, and a supercell. We use the term "isolated convective storm" throughout this work to refer to a common weakly-sheared unorganized convective storm, sometimes called an "air mass" thunderstorm. We will **not** use this term to refer to the supercell as "the supercell", although it is technically an isolated convective storm. We will also at times refer to the squall line and supercell collectively as the "more organized" storms. A conceptual model of the development of isolated convective cells has existed for at least 75 years (Byers and Braham 1949), and they have been well-studied in both observations and simulations since that time (Wilhelmson 1974; Schlesinger 1978; Szoke and Zipser 1986; Kingsmill and Wakimoto 1991; Yang et al. 2016; Moroda et al. 2021). The same is true of mid-latitude continental squall lines (Byers and Braham 1949; Newton 1950; Browning 1977; Maddox 1980; Weisman and Klemp

1984; Bluestein and Jain 1985; Smull and Houze 1987; Rotunno et al. 1988; Weisman and Rotunno 2004; Seigel and van den Heever 2013) and supercellular convection (Newton and Katz 1958; Browning 1964; Fujita and Grandoso 1968; Schlesinger 1978; Lilly 1982, 1983; Davies-Jones 1984; Grant and van den Heever 2014). These three morphologies comprise the majority of summertime convective storms in the continental midlatitudes (Cotton et al. 2010), and thus are likely to be most responsible for rain-induced aerosolization of biological particles in these regions.

For all three storms, we use a horizontal grid spacing of 500m and a stretched vertical grid with vertical grid spacing ranging from 25m at the surface to 250m at higher levels. This fine vertical grid spacing at the surface is needed to represent low-level storm processes that are important to transport, in particular the dynamics of the cold pool and the low-level convective updraft. All three storms are initialized via warm- or cold-bubble forcings in an initial Weisman and Klemp (1984) environmental profile applied horizontally uniformly over the domain **(Figure 6.1)**. Random perturbations to the potential temperature with a maximum amplitude of 0.1 K are also added throughout the domain. Such perturbations are required for the squall line initialization because it is otherwise perfectly uniform in the meridional direction. These perturbations are also applied in the initialization of the other storm simulations to ensure consistency with the treatment of the squall line. The initial environmental soundings vary between the simulated storms only in the vertical shear profile and the low-level moisture, as described in **Error! Reference source not found.**, and follow the general approach initially established in Weisman and Klemp (1984). We do not include any topography in the model domain's terrain.

The isolated convective storm and the supercell are initialized via Gaussian warm bubbles (Weisman and Klemp 1982; Seigel and van den Heever 2012; Grant and van den Heever 2014), while the squall line is initialized via a cold bubble (Weisman et al. 1997; Bryan and Morrison 2012; Seigel and van den Heever 2013) the amplitude of which is zonally Gaussian about its center and meridionally uniform (i.e. the bubble is "infinitely" long meridionally) (Seigel and van den Heever 2013; Lebo and Morrison 2014; Mulholland et al. 2021). All horizontal lateral boundary conditions are radiative, except for the meridional boundary of the squall line domain which is periodic. A Rayleigh damping layer with a 60 second timescale is applied to the upper 2km of the domain so as to prevent the reflection of any gravity waves off of the top of the domain. We employ a two-moment bin-emulating bulk microphysics scheme (Meyers et al. 1997) with seven of the eight hydrometeor species described in Saleeby and Cotton (2004) (drizzle is excluded) and an ice nucleation parameterization described in DeMott et al. (2010). The initial aerosol profile consists of sulfates and aerosols, and their concentration decreases linearly from 100 cm^{-3} at the surface to 10 cm^{-3} at 4 km AGL, above which the concentration is held constant at this value (Saleeby and van den Heever 2013).

Radiation is disabled for all three simulations. As all three storms are initialized in thermodynamically unstable environments, radiation quickly causes other convective activity all over the domain. Excluding radiative forcings thus allows us to analyze individual idealized storms with well-understood conceptual descriptions in the literature, without needing to account for the complexities introduced by additional widespread convection in the domain. Similarly, free-slip surface boundary conditions are used in order to simplify our analysis of the development of each storm without needing to consider land surface type or interactions. Both of these simplifications allow us to focus our analysis on the transport of air containing rain-

aerosolized biological particles in these storms, rather than on the intricacies of very complicated interactions between the storms and a less idealized environment. While these interactions may ultimately be relevant for aerosol transport, they are outside of the scope of this study. Further model setup details are listed in Table 5.1.

2.2 Definition of supercell right-mover

We limit our analysis of the supercell to tracer and parcels entrained into the right-mover of the supercell only, excluding the left-mover and any further storms that subsequently split off from it. We define the right mover spatially, excluding the portion of the domain above a diagonal line running from (x=0km, y=78km) to (x=424.5km, y=162.5km), where x and y are the zonal and meridional coordinates respectively. This cutoff was chosen through trial and error to cleanly isolate the right mover based on an examination of the rainfall rate, 0-1km mean updraft, 0-1km mean horizontal winds, 5km updraft, total column condensate, and 0-1km mean potential temperature deficit relative to the base state (not shown). This cutoff is applied to all figures and calculations in the results section, and the left-mover region is not included in the analysis. It is important to note, however, that tracers are still produced (as described in the section below) in the left-mover region. While we do not include this emitted tracer in any of the quantities in the results section that are functions of the total amount of tracer emitted, it is possible that tracer produced in the left-mover region could be entrained into the right-mover. This does not appear to happen to any significant degree based on our analysis of the spatial distributions of tracer and the winds over time (not shown), but we note it as a potential source of bias, as our Eulerian analysis cannot identify the gridpoint in which the tracers originated. We also note that some parcels in our trajectory analysis that are placed near the northeast corner of

the grid of parcels in a given initialization, being up to 70km away from the center of the right mover's updraft, are instead entrained into the disorganized left-mover or one of the storms that split off from it. This comprises less than 5% of parcels initialized at any single time and less than 2% of all parcels that we initialize. We treat these parcels as not entrained in all calculations that depend on whether a parcel was entrained into a storm.

2.3 Passive tracer setup

We utilize passive tracer quantities to measure the entrainment of surface air and its subsequent spatiotemporal distribution within the storms. The tracer quantities are additional variables in the numerical model that are subject only to advection and diffusion. They are best thought of as properties of the air in a grid point that can mix between air masses and move within the domain but which do not affect the motion of the air, rather than as literal particles. They are purely diagnostic and do not affect any other variables of the model. This passivity is a desirable characteristic of a tracer quantity for this study, where we use such quantities to investigate aerosol transport without considering the microphysical or radiative feedbacks of aerosols themselves. This characteristic of the tracers is thus chosen deliberately in order to isolate the problem of aerosol transport. The model can individually track an arbitrary number of separate tracer "species" which do not interact with each other. As such, we can use different tracer species to measure multiple different origins and associated transport pathways in the same simulation.

The tracers are emitted into the model domain via two different source mechanisms, which we use to measure different transport pathways. We refer to the first of these source mechanisms as *fixed-source* (FS) emission. Fixed-source emission adds tracer to all horizontal

gridpoints in the model domain at the lowest vertical level above the ground (~12 m), at a constant rate and at each timestep. We utilize tracers emitted in this way (which we will refer to as fixed-source tracers) to quantify the total amount of surface air that has been entrained into the simulated storm updrafts. We make use of the different tracer species that the model can separately track by changing the species that is emitted via this mechanism after every five minutes of simulation time. As an example, tracer species 1 (TS1) is emitted in the manner just described from t=0 minutes to t=5 minutes. At t=5 minutes, this tracer is no longer emitted, and the amount present in the simulation domain is all that will ever be emitted. Rather, another tracer species, TS2, is then emitted beginning at t=5 minutes. The per-timestep and per-gridpoint rate at which this tracer is emitted is identical to that of TS1. This tracer is emitted until t=10 minutes, after which no more of it is ever emitted, and TS3 is then emitted at the same rate from t=10 minutes to t=15 minutes. This pattern continues for the 3 hours of simulation time for all three storm morphologies (**Figure 6.2a)**. This approach has two desirable properties. First, the total fixed-source tracer emitted into the domain (i.e. the sum of the amount emitted across the fixed-source tracer species) increases at a constant rate and thus is linear in time. This facilitates comparison of fixed-source tracer concentrations between storms and across times within a storm, since the rate of increase of the total amount emitted is equal between storms when normalized by the size of the storm's simulation domain. Second, the fact that each species is emitted at a different time provides information about the time at which a parcel of air was in contact with the surface. This proves useful for analyzing the spatiotemporal distribution of tracer in each storm.

We refer to the other tracer emission mechanism as *rain-sourced emission*. Unlike the fixed-source emission, rain-sourced emission is not constant in time. It also does not occur over

the whole domain, and it does not change species in time. Rather, a rain-sourced tracer is emitted at each timestep in which the surface rain rate at a given gridpoint exceeds a specified threshold value. In this way, if the fixed-source tracer represents the degree of entrainment of all surface air, the rain-sourced tracer represents the degree of entrainment of air only from rainy regions, i.e., from regions where biological particles would be aerosolized. We emphasize that, as with the fixed-source tracer, the rain-sourced tracer is not intended to emulate actual aerosol particles, nor the aerosolization of such particles, but rather to track the location of air that would contain biological particles aerosolized by rain. The emission of rain-sourced tracer is binary in the sense that the rate does not depend on the amount by which the rainfall threshold is exceeded; the emission is either "on" or "off". The per-timestep emission rate of the rain-sourced tracers is equal to that of the fixed-source tracers in order to facilitate comparison between the two tracer categories. This emission rate itself is not physically meaningful, as it is only used for comparisons between tracer concentrations or is normalized by the total amount of tracer emitted, and is set to a value of 25,000 #/kg/s in each gridpoint. Five rain-sourced tracer species are utilized, each of which is emitted above a different surface rain rate threshold of 1 mm/hr, 5 mm/hr, 10 mm/hr, 20 mm/hr, or 40 mm/hr **(Figure 6.2b)**. These separately tracked tracer species allow us to differentiate the entrainment of air from regions of intense rainfall from that of air originating in regions of lighter rainfall rates.

In addition to tracking the tracer quantities themselves, we also track the total quantity of each tracer that has been emitted at each horizontal gridpoint and thus also, by summing over all horizontal gridpoints, over the whole domain. While the total amount of fixed-source tracer emitted could be calculated from the domain size and the emission rate, this is not the case for rain-sourced tracer, which is dependent on the presence and amount of rainfall. Furthermore, the

tracer is allowed to advect out of the domain, so it is not possible to simply sum up the domain-wide tracer concentration at the end of the simulation in order to calculate the total emitted. Tracking the total amount emitted from within the model allows us to normalize the degree of entrainment of air from rainy regions by the size and duration of the storm's rainfall, as well as to normalize fixed-source tracer concentrations by the size of the simulation domain. This facilitates equitable comparisons between the storm morphologies and between the tracers emitted by the two emission mechanisms.

2.4 Trajectory setup

In addition to passive tracers, which are run "online" (i.e. integrated into the RAMS model), we calculate air parcel trajectories "offline" using completed simulation output. A trajectory is calculated by initializing a parcel at a specific time and location in the domain, then using the wind variables output by the simulation to calculate the motion of the parcel over time. This approach requires much more frequent model output than is sufficient for the rest of the storm analysis. While most of our analysis of the storm dynamics and the tracer analysis is done using output at 5-minute intervals, we use 2 second output for the trajectory calculations in order to adequately resolve the motion of the air parcels throughout the storm systems. We test the sensitivity to this timestep by recalculating all of the trajectories computed for the supercell using output at 30, 10, 6, and 2 second timesteps. We then compare the positions of each individual parcel at the end of the simulation between the 30 s and 10 s timesteps, the 10 s and 6 s timesteps, and the 6 s and 2 s timesteps. We say that a parcel's position has converged between these pairs of simulations if the parcel's final positions are within 4 gridpoints of each other horizontally, so within 2 km, and vertically within 4 gridpoints at the finest vertical resolution,

which is 25m, so within 100m of each other. We find 95.7%, 98.9%, and 99.6% agreement in final parcel positions between the trajectories calculated using the three pairs of timesteps, respectively. Thus, while the trajectories calculated with the 6 s and 2 s timesteps converge for nearly all of the parcels and do so in a storm with high wind speeds, we use the 2 s timestep to ensure maximally accurate results. We also note that this timestep is in keeping with the range of timesteps used for trajectory calculations in the literature. A subset of timesteps used in publications examining convective storm dynamics using trajectories calculated from mesoscale model output include a 1 s timestep using data interpolated from model output at 1 minute frequency (Seigel and van den Heever 2012), a 1 minute timestep (Mulholland et al. 2019), and a 2 second timestep as the shortest timestep in a paper exploring errors arising from coarse spatiotemporal resolution in trajectory calculations in a supercell (Dahl et al. 2012). Thus, the 2 second timestep used here is in keeping with this range of previously utilized values. The trajectories are calculated using a semi-implicit discretization that is second-order accurate in space and time, and which is employed in existing publications and widely-used trajectory calculation tools (Wernli and Davies 1997; Miltenberger et al. 2013; Gowan 2018; Mulholland et al. 2019).

We initialize parcels in each simulation beginning at the time at which the z=5 km updraft velocity reaches 20% of its maximum value, which we calculate as follows. First, for each timestep in each storm, we smooth the z=5km updraft by taking a 2km x 2km windowed minimum over the values of vertical velocity at 5km altitude. At each horizontal gridpoint, the updraft at z=5km is thus at least as strong as the value returned by this calculation for 2km in any horizontal direction from that point. We then take the maximum of these values over the horizontal domain, which gives the fastest 2km x 2km updraft in that storm at that timestep at the

z=5km vertical level. We do this for each timestep in each storm, giving us each storm's maximum z=5km updraft speed vs simulation time, which we then smooth with a 15 minute windowed mean **(Figure 6.3 a-c)**. We then find the maximum value of this metric that is reached by each storm over the course of the simulation, and define a value we will call W_{20max} as 20% of that maximum value. We begin initializing parcels when the z=5km maximum updraft speed calculated above first reaches W_{20max} (indicated by the dashed vertical line in **Figure 6.3 a-c**).

Once the updraft speed reaches W_{20max}, we initialize a set of parcels every ten minutes from this time until 30 minutes before the end of the simulation. We choose to begin releasing parcels at this time, when the mid-level updraft has reached 20% of its maximum speed, simply as a uniform proxy for all three storms having reached an early stage of their development. We could initialize parcels before an updraft has developed at all, but this would add computational expense while being unlikely to offer any additional insights. We initialize each set of parcels in a grid of 100km x 100km horizontal extent at the model's lowest real vertical level (~12 m AGL). At each parcel initialization time, this grid of parcels is centered on the centroid of the horizontal points where the z=5km updraft exceeds W_{20max}. The parcels are spaced 2 km apart in x and y, and so each set of parcel initializations is comprised of 2500 parcels (i.e., 50 x 50). All parcel trajectories are run from the time they are initialized until the end of the simulation.

We center the parcels on the 5km updraft as a measure of each storm's position in the mid-levels. As the squall line in particular has an updraft that tilts upshear, defining the position of the storm using its mid-level updraft ensures that the parcels being initialized cover the entire horizontal extent of the storm. We also note that we choose to initialize the parcels in a 100km x 100km grid, which is much larger than the extent of any of the storms (except the infinite

meridional extent of the squall line), so as to make our results as insensitive as possible to the choice of the initial center point for each batch of parcels.

We define a parcel as having been entrained into a storm when it reaches an altitude of 6km. We confirm the appropriateness of this vertical level as our entrainment criterion by examining the distribution of the altitude values of all parcels in each storm at the ends of the simulations (**Figure 6.4**). The distribution is strongly bimodal for all three storms, with peaks centered around ~0-2km and ~10-14 km. We also conduct a basic sensitivity test by calculating the fraction of parcels that are ever entrained using entrainment height thresholds ranging from 5km to 8km and find changes of no more than a few percent for any storm or initialization time. Thus, we expect that our results are minimally sensitive to this choice of threshold, so long as it falls within the mid-levels of the storms.

In addition to tracking the positions of the parcels over their trajectories, we track several variables of interest taken from the RAMS simulation output along the parcels' paths. These include the Exner function, potential temperature, vapor mixing ratio, and condensate loadings of each hydrometeor species. Combined, these variables allow us to characterize various microphysical aspects of the parcels' paths such as the time spent in supersaturated environments.

2.5 Storm-relative depictions of squall line trajectories

The figures of entrainment of parcels into the squall line from rainy and non-rainy regions presented later in this paper (**Figure 6.15**) differ from those for the isolated convective storm and supercell in that they depict the *storm-relative* motion of the parcels, rather than the absolute motion of the parcels. This significantly eases the interpretation of the entrained parcels'

trajectories for the squall line in particular. The motion of the storm is calculated by first calculating the position of the centroid of the horizontal gridpoints at which the mean updraft in the layer from z=0-1 km is greater than or equal to 1 m/s, and then differencing these positions in time. We use this calculation rather than the mid-level position used to center the initialization of parcels because for this storm we are especially interested in using the trajectories to see the circulation in and near the head of the cold pool. By subtracting off the motion of the low-level updraft associated with the gust front of the cold pool, we subtract off the motion of the parcels relative to the cold pool itself more accurately, and can thus see their cold pool-relative motion. The motion of the storm in the meridional direction is proscribed to be 0 for calculating the storm-relative motion, because the storm is infinite in y with periodic boundaries and there is no V wind in the base state environmental profile. As a result, all motion of the parcels in the y direction in the figures of squall line parcel entrainment is absolute.

Chapter 3 RESULTS

3.1 Storm evolution and analysis

As mentioned in the methodology section, we simulate three different convective storm morphologies: an isolated convective storm, a squall line, and a supercell. We do so by using different bubble forcings in initial environments that vary only in their moisture amounts, the strength of their vertical wind shear, and whether the vertical wind shear is unidirectional or veers with height.

a Isolated convection

The deep isolated convective cell's development follows that of a classic convective cell (e.g. Byers and Braham 1949, Wilhelmson 1974, Schlesinger 1978). The initial warm bubble forcing has developed into an updraft stretching from very near the surface to the upper troposphere by t=65 minutes (Szoke and Zipser 1986) **(Figure 6.5 a, d)**. Relatively strong convergence at the base of the updraft is evident in the wind field. The downdrafts on either side of the main updraft are typical of this development and indicate the presence of hydrometeors, which create these downdrafts by evaporative cooling. Precipitation on the downshear side of the storm is favored in this weakly sheared system, and 20 minutes later at t=85 minutes the downdraft on this side stretches from the upper troposphere to the surface **(Figure 6.5 b, e)**. The plan view clearly shows that the downdraft has formed from what was once the updraft, which has been a hallmark of the conceptual model of isolated convection from its earliest iteration. A cold pool has also developed near the surface from the evaporative cooling of the hydrometeors falling in the downdraft by this time. The cold, dense air of the cold pool spreads laterally, and

completely cuts off the low-level inflow to the updraft by t=135 minutes **(Figure 6.5 c, f)**. The updraft decays completely shortly after this, and its remaining hydrometeors evaporate or precipitate out, at which point the cell's life cycle is over.

b Squall line

The squall line, being initialized with a horizontally homogeneous base-state environment and a cold bubble that is infinite in the meridional direction, is initially nearly completely uniform in the line-parallel (i.e. meridional) direction **(Figure 6.6 a, d, g)**. By t=70 minutes, it has formed a cold pool with the typical cleft-and-lobe structure of a density current (Simpson 1969), with a fairly strong updraft at the gust front driven by convergence, and large concentrations of hydrometeors in its updraft. At t=105 minutes, it has developed an alternating cell structure in the y direction **(Figure 6.6 b)**. Regions of strong surface downdrafts and heavy rainfall stretching ~15km behind the gust front alternate with regions of weaker downdrafts and heavy rain that only extends ~10km behind the gust front **(Figure 6.6 b)**. We observe weak ascending upper-level rear outflow, which is a common feature in a typical squall line (Weisman et al. 1988) **(Figure 6.6 e, h)**. We do not yet observe significant rear inflow. The updraft is upright at this time, which is ideal for the further development of the storm (Rotunno et al. 1988).

The divergence associated with the alternating cells of heavier rain and stronger downdrafts (Weisman et al. 1988) drives the cold pool forward in these regions, creating what we will refer to as a "convex region" in the cold pool boundary. **(Figure 6.6 c).** Between these convex regions are regions where the divergence from these alternating rain shafts meet, creating convergence and lifting at the surface rather than pushing the cold pool forward **(Figure 6.7 a)**,

leading to a "concave region" in the cold pool boundary. The updraft is tilted significantly upshear at this time **(Figure 6.6 f, i)**. The updraft is continuous from the gust front to upper levels in the concave region **(Figure 6.6 f)**, but not in the convex region, where it is broken by a downdraft bearing hydrometeors (e.g. Jorgensen et al. 1997) **(Figure 6.6 i)**. The rear inflow jet has also strengthened by this point in both the concave and convex regions, which is in keeping with the hypothesis that it is driven by a pressure deficit between the cold pool and updraft when the updraft tilts upshear (Weisman 1992). We will see later that trajectories that are entrained through convex regions versus through concave regions experience different microphysical environments.

c Supercell

The storm that forms from the initial warm bubble forcing used for the supercell develops a mid-level cyclonic/anti-cyclonic vorticity couplet (Schlesinger 1978) at around t=60 minutes and subsequently splits into left- and right-movers (Fujita and Grandoso 1968; Weisman and Klemp 1982) at about t=75 minutes (not shown). The right mover is favored due to the veering wind profile used in the environmental base state (Weisman and Klemp 1984). As mentioned in the methodology, our analysis considers only the right-mover. At t=90 minutes, the right mover has the classic comma/hook shape (Weisman and Klemp 1984), distinct rear- and forward-flank downdrafts with precipitation generally centered around the latter (Lemon and Doswell 1979; Rotunno and Klemp 1985) **(Figure 6.8 a)**, and positive mid-level vertical vorticity indicative of the mid-level mesocyclone (Davies-Jones 2015) **(Figure 6.8 d)**. The updraft is located at the leading edge of the rear-flank downdraft's cold pool. The upper-level flow is generally towards

the forward flank of the storm (Lemon and Doswell 1979). All of these characteristics agree with the classical conceptual model of a developing supercell.

By t=140 minutes, the storm is also acquiring low-level vertical vorticity (Rotunno et al. 2017) **(Figure 6.8 e)**, and the rain centered on the forward-flank downdraft is heavy and covers a large area. By t=170 minutes, this low-level vortex has reached its maximum value of vertical vorticity, which is greater than that of the mid-level mesocyclone **(Figure 6.8 f)**. The storm is fully mature by this time according to most conceptual models of classic supercells.

3.2 Tracer analysis

Unless stated otherwise, all analysis in this section on tracer analysis considers only the updraft of each storm. Any tracer concentration or mixing ratio given in the remainder of this work represents the mean in the updraft of the storm; besides where it is included for emphasis, we exclude "mean in-updraft" from references to these quantities for brevity. Model gridpoints are considered in-updraft if they have a vertical velocity of at least 1 m/s and a condensate loading of at least 0.1 g/kg.

We refer to each of the separately tracked tracers utilized in the model as a "tracer species". We also use the term "fixed-source tracer" to refer to the sum of all fixed-source tracer species. Any discussion of individual tracer species specifies explicitly that that is what is being discussed.

a Outline of metrics

We first outline several metrics that will be used throughout the discussion of the tracer analysis. The fixed-source tracer mixing ratio in a gridpoint is the product of the mass of air in

the gridpoint that was in contact with the surface and the duration for which it was in contact with the surface, divided by the mass of air in the gridpoint, i.e., in a single gridpoint we can write:

$$Mean\ FS\ tracer\ mixing\ ratio\ [\#\ kg^{-1}]$$

$$= \frac{Total\ kg\text{-}seconds\ of\ surface\ contact\ [kg * s] * Emission\ rate\ [\#\ kg^{-1}s^{-1}]}{Mass\ of\ air\ in\ gridpoint\ [kg]}$$

The rain-sourced tracer mixing ratio can be represented using the same equation but is only calculated for surface gridpoints in which the rain rate exceeds one of the given threshold values at each point in time. The most salient quantity for measuring the potential for the microphysical impact of biological particles aerosolized by rain is the mixing ratio of the rain-sourced tracers, as this is the most direct measure of the amount of air containing these particles that has been entrained into a microphysically active environment. This quantity reflects a combination of many different processes and characteristics of each storm, and some of the most salient questions we could ask to disentangle these factors are as follows:

- How much air from the surface does the storm entrain?
- What proportion of the storm's entrained surface air is from rainy regions?
- What proportion of all rainy surface air does the storm entrain?
- How much rain of a given intensity does the storm produce relative to the mass of its updraft?

To address these questions, we first define the mean rain-sourced tracer mixing ratio mathematically:

$$Mean\ RS\ mixing\ ratio[\#\ kg^{-1}] = \frac{Total\ RS\ tracer\ entrained\ [\#]}{Updraft\ mass\ [kg]}$$

We can rewrite this in two other ways which are algebraically equivalent, and which we can then map onto these physical questions:

$$Mean\ RS\ mixing\ ratio\ [\#\ kg^{-1}]$$
$$= \frac{Total\ FS\ tracer\ entrained[\#]}{Updraft\ mass\ [kg]} * \frac{Total\ RS\ tracer\ entrained[\#]}{Total\ FS\ tracer\ entrained[\#]}$$

and

$$Mean\ RS\ mixing\ ratio[\#\ kg^{-1}]$$
$$= \frac{Total\ RS\ tracer\ entrained\ [\#]}{Total\ RS\ tracer\ emitted\ [\#]} * \frac{Total\ RS\ tracer\ emitted\ [\#]}{Updraft\ mass\ [kg]}$$

We now summarize these terms and the physical questions they answer, as well as giving them names which we will use in the remainder of this study for convenience:

Table 3.1 Definition and description of physical quantities influencing the rain-sourced tracer mixing ratio.

Term	**Physical question answered**	**Name**
$\frac{Total\ FS\ tracer\ entrained[\#]}{Updraft\ mass\ [kg]}$	How much air from the surface does the storm entrain per updraft mass?	[Mean in-updraft] fixed-source mixing ratio
$\frac{Total\ RS\ tracer\ entrained[\#]}{Total\ FS\ tracer\ entrained[\#]}$	What proportion of the storm's entrained surface air is from rainy regions?	Rain-sourced tracer fraction
$\frac{Total\ RS\ tracer\ entrained\ [\#]}{Total\ RS\ tracer\ emitted\ [\#]}$	What proportion of all rainy surface air does the storm entrain?	Rain-sourced entrainment efficiency
$\frac{Total\ RS\ tracer\ emitted\ [\#]}{Updraft\ mass\ [kg]}$	How much rain of a given intensity does the storm produce per updraft mass?	Rain production efficiency

Thus, by looking at these quantities we can determine if a storm attains greater/lesser values of the rain-sourced tracer mixing ratio because, for instance, it does/does not entrain much air from the surface; it does/does not produce much rain, or much rain of a high intensity;

whether the air from the rainy regions it does produce is/is not entrained into the storm's updraft; and/or whether it produces more/less rain than the other storms on a per-updraft mass basis. We note that our "rain production efficiency" differs from the "precipitation efficiency" sometimes referred to in the literature, which is the ratio of the surface precipitation rate to the vapor flux of a storm (e.g. Browning 1977), whereas here it describes the ratio of the surface precipitation rate of a given intensity to the mass of the storm's updraft.

We will first examine the rain-sourced tracer mixing ratios themselves and then analyze these constituent quantities.

b Rain-sourced tracer mixing ratio

The rain-sourced tracer mixing ratio conveys information about the mass-time (i.e. kilograms*seconds) that air in each storm's updraft has spent in rainy surface regions. The maximum rain-sourced tracer mixing ratios across the three storm morphologies are of similar magnitudes for the tracer emitted in regions where the rainfall rate is at least 1 mm/hr, varying by at most a factor of ~2 (**Figure 6.9 j-l**). The maximum rain-sourced tracer mixing ratio increases monotonically with rainfall rate when compared in a fractional sense against that of the isolated convective storm. The supercell exhibits the same increase relative to the isolated convective storm for rainfall rates up to 20 mm/hr. This indicates that the isolated storm and the two organized storms entrain surface air from regions of light rain in similar proportions, at least in the sense of their maxima, but that the isolated convective storm entrains less surface air from regions of heavy rain than do the two organized storm morphologies. This could occur either as a result of the fact that the isolated storm produces relatively little heavy rainfall, and/or it entrains

less surface air from heavy rainfall regions. The sections following this one are devoted to answering this and analogous questions for all three storms.

The isolated convective storm reaches its maximum mixing ratio (of all rain-sourced tracer species) at t=90-95 minutes, while all of the rain-sourced tracer species in the squall line and supercell reach their maximum values much later in the storms' lifetimes (between t=145-180 minutes). As a consequence of the fact that the isolated convective cell decays while the organized storms do not **(Figure 6.11 a)**, the isolated storm's tracer mixing ratios begin decreasing across all rain thresholds shortly after reaching its maximum value. By contrast, the mixing ratios of all rain-sourced tracers show a generally upward trend through the whole duration of the organized storms.

The squall line and supercell achieve similar maximum and end-of-simulation mixing ratios to each other for each of the rain-sourced tracers emitted at the three lowest rain thresholds (1, 5, and 10 mm/hr), with the maximum values varying by less than a factor of ~1.4 and the end-of-simulation values varying by less than a factor of ~1.3. However, the squall line and supercell exhibit different mixing ratios of tracer emitted in regions of heavier rain, with the squall line reaching greater maximum values at both the 20 and 40 mm/hr thresholds by factors of ~1.9 and ~14.6, respectively. This indicates that, if bioaerosols are aerosolized by lighter rainfall rates, the per-updraft entrainment of air containing these particles is similar between the two storm morphologies, but that the squall line entrains significantly more of this air on a per-updraft basis if the aerosolization requires heavier rainfall.

c Fixed-source tracer mixing ratio

As discussed in the methods section, the fixed-source tracer mixing ratios in each storm convey information about the entrainment of all surface-based air, since fixed-source tracer is continuously produced at the surface over the entire domain at all timesteps. The isolated convective storm and the squall line's maximum values of the fixed-source tracer mixing ratios in their updrafts are within ~5% of each other, while the supercell's maximum mixing ratio is ~50% less than that of either the isolated convection or the supercell (**Figure 6.10 a-c)**. However, the isolated convective storm reaches this maximum mixing ratio earlier in the simulation than does the squall line, and so less fixed-source tracer has been emitted into the domain when it reaches its maximum. We can therefore conclude that the isolated convective storm has the greatest peak proportion of air in its updraft that originated at the surface, as the fixed-source tracer mixing ratio indicates the mass-*seconds* for which the air in a gridpoint was in contact with the surface. This generally agrees with conceptual models of each storm, where the updraft of an isolated convective cell may be fed by a single region of convergence at the surface (Byers and Braham 1949), while conceptual models of squall lines often contain a region of descending rear inflow originating at midlevels (Smull and Houze 1987), and the updrafts of supercells entrain some air from their own downdrafts originating at midlevels (Rotunno and Klemp 1985).

The supercell's fixed-source tracer concentrations are low compared to the other storms in the first ~120 minutes of the simulation, which owes to the progression of the supercell's development. The maximum 5km updraft speed has already reached its maximum strength of nearly 40 m/s by t=100 minutes **(Figure 6.3 c)**, which is much stronger than either of the other two storms. By contrast, its low level updraft at this time is weak **(Figure 6.11 c)**. At t=100

minutes, the supercell has developed a midlevel mesocyclone, with a z=6 km vertical vorticity maximum equal to ~72% of the maximum vertical vorticity it develops at this vertical level by the end of the simulation. The low-level mesocyclone is still developing at this time, as evidenced by the z=1km vertical vorticity maximum being at only ~37% of its maximum value at this time, and the strength of the surface region of low pressure associated with the updraft similarly being at only ~34% of its maximum (not shown). This follows the typical progression of supercell development (Davies-Jones 2015), where a midlevel mesocyclone develops first via tilting of streamwise horizontal vorticity by the environment's vertical shear (Rotunno and Klemp 1982), and a low-level mesocyclone subsequently develops by tilting and stretching of frictionally- and baroclinically-generated horizontal vorticity (Rotunno et al. 2017). The progression we observe also agrees with Coffer et al. (2023), who found that the midlevel mesocyclone (which also develops first in their study) entrains some midlevel air, but that the low-level mesocyclone entrains air almost entirely from the surface. Thus, the progression of the storm that we observe and the portion of surface air in its updraft are in keeping with previous work. In comparing to the squall line, Fierro et al. (2009) found that their simulated squall line entrains the majority of the parcels ahead of it and lifts them to the upper troposphere, which is difficult to directly compare quantitatively, but in a broad sense seems to agree with our finding that the squall line entrains the most surface air.

The fixed-source tracer mixing ratio in the isolated convective storm is dominated by the tracer species that are emitted early in the simulation **(Figure 6.9 a, g)**, and therefore by air that was in contact with the surface early in the simulation. The fixed-source tracer mixing ratios in the squall line and supercell updrafts are instead driven by the entrainment of newly emitted tracer as the storm progresses and comes into contact with new surface air (**Figure 6.9 b-c, h-i**).

This is also the reason that, for the squall line and supercell more than for the isolated convective storm, the mixing ratios of each individual tracer species are nearly identical beginning shortly after each species is emitted: new air from the surface is being processed by the storm, which contains all of the tracer species that have been emitted up to that point. This is not as much the case with the isolated convective storm because its updraft soon weakens and dies, and so it does not entrain as much air that is in contact with the surface at later times in the simulation.

d Rain-sourced tracer fraction

Recall that the rain-sourced tracer fraction refers to the ratio of a storm's rain-sourced tracer mixing ratio to its fixed-source tracer mixing ratio, and that this is calculated individually for each rain-sourced tracer/rainfall threshold. This quantity gives information about the proportion of surface air entrained into a storm that has been in contact with rainy regions relative to the total entrained surface air. For all rain-sourced tracers, the isolated convective storm achieves lower maximum values of the rain-sourced tracer fraction than either of the two more organized storm morphologies. This provides one aspect of the explanation for the lower rain-sourced tracer mixing ratios reached in the isolated convection: compared to the other two storms, the surface air from rainy regions that is entrained by the isolated storm is being diluted by more surface-based air that is not originating in rainy regions. This comports with the observation that the isolated convection reaches a maximum fixed-source tracer mixing ratio greater than that of the supercell and comparable to that of the squall line (**Figure 6.10 a-c**), despite being a dynamically weaker storm: the rain-sourced tracer mixing ratios it does attain are not because it is efficient at entraining air from rainy regions specifically, but because it has strong surface convergence and inflow, and because it draws air from all directions as opposed to

the organized morphologies which, as we will show in the trajectory analysis, draw air preferentially from specific directions.

Whereas the squall line and supercell both have larger maximum rain-sourced tracer fractions than the isolated convective storm across all of the rain-sourced tracer species, the differences in rain-sourced tracer fraction between the squall line and the supercell themselves depend on the rain-sourced tracer species, and hence on the rainfall rates. (Recall here that the different rain-sourced tracer species are emitted at different threshold rainfall rates.) The squall line's maximum and time-averaged tracer fractions are ~20-50% less than that of the supercell for the tracers emitted at <= 10 mm/hr of rainfall, but the squall line's tracer fractions are larger for the tracers emitted at >= 20 mm/hr of rainfall. In other words, compared to the squall line, a larger proportion of the surface air that the supercell entrains comes from regions of light rain, but the opposite is true when considering regions of heavy rain.

The rain-sourced tracer fraction, in conjunction with the rain-sourced tracer mixing ratio and the fixed-source tracer mixing ratio, allows us to describe the physical processes responsible for the differences in the entrainment of rainy air between the three storm morphologies. For instance, the squall line and supercell reach comparable mixing ratios of the three rain-sourced tracers corresponding to the lightest rainfall rates. However, we can see from their relative values of the fixed-source tracer mixing ratio (squall line > supercell) and rain-sourced tracer fraction (supercell > squall line) that these comparable values are reached through different transport dynamics. The squall line entrains more air that has been in contact with the surface (in a mass-seconds sense), but less of this air is from rainy regions. The supercell does not entrain as much air that has been in contact with the surface, but more of what has been entrained is from regions where it is or has been raining. By contrast, for the tracers emitted at heavier rainfall rates, the

squall line reaches greater in-updraft mixing ratios than the supercell, which is attributable both to its larger amount of entrained surface air *and* the fact that a larger fraction of this surface air originates from regions of heavy rain. Further, the isolated convective storm entrains a quantity of air from the surface that, at its peak, is comparable to the largest value reached by either of the more organized storms. However, it only briefly achieves rain-sourced tracer concentrations for light rain of the same order of magnitude as the other storms because a much smaller fraction of this surface air has been in contact with rainy regions of any intensity, as manifested in its much lower rain-sourced tracer fractions. For heavy rain, its rain-sourced tracer fractions are even lower, and so are the concentrations of these tracers in its updraft.

e Rain production efficiency

Having analyzed the rain-sourced tracer mixing ratios in view of the physical quantities in the first two rows of **Error! Reference source not found.**, we now turn our attention to the quantities in the latter two rows, the *rain production efficiency* and the *rain-sourced tracer entrainment efficiency*, beginning with the former. Recall that the rain production efficiency [#/kg] is defined as the domain-wide cumulative (up to a given point in time) quantity of rain-sourced tracer emitted, divided by the updraft mass (at that point in time), and that it addresses the question "What proportion of all rainy surface air does the storm entrain?". The rain production efficiency is calculated independently for each rain-sourced tracer species, as they require different rainfall rates for emission.

The isolated convective storm achieves the greatest instantaneous value of the rain production efficiency for all rain thresholds (**Figure 6.10 g-i**). As with some of the other metrics for this storm, these large values are driven by the decay of its updraft, which in this case makes

the denominator of the rain production efficiency term very small as the storm decays. These large values of the rain production efficiency are thus a reflection of the fact that the storm continues to rain after its updraft begins decaying (**Figure 6.3 a, d)**, rather than of an exceptionally large amount of rain being produced per updraft mass. A more salient measure than the maximum value of the isolated convective storm's rain production efficiency is its rain production efficiency at t=100 minutes (**Figure 6.10 g**), when its updraft mass (**Figure 6.10 a**) and the size of its rainy region (**Figure 6.3 d**) are both near their peak. As this is indicative of the isolated convective storm having reached a mature stage in its development, we compare the values of the isolated storm's rain production efficiency at t=100 minutes against the end-of-simulation values of the other storms, when their updraft masses and rainfall peak, and they exhibit characteristics indicating their maturity as discussed in section 3.1. The isolated storm's rain production efficiency compared in this way to that of the squall line, and expressed as a percentage, ranges from 50% for the lightest rain to 25% for the heaviest rain and decreases monotonically between the two. Similarly, its rain production efficiencies compared in this way are less than half those of the supercell for rainfall rates <= 20 mm/hr, and ~80% of the supercell's for rainfall rates >= 40 mm/hr. This indicates that the squall line and supercell produce rain more efficiently than does the isolated convective storm for all rain intensities, but that this difference is most pronounced for heavy rain (excepting the heaviest rainfall rates in the supercell).

At the end of the simulation when both storms are mature, the squall line and the supercell's rain production efficiencies for rainfall rates <= 10 mm/hr are each within ~25% of the other storm's value (**Figure 6.10 h-i)**. The squall line approaches these values earlier in the simulation than does the supercell, exhibiting a plateau-like shape when plotted against time

(**Figure 6.10 h)**. From t=75 minutes to t=180 minutes (**Figure 6.10 b)**, the supercell's updraft mass increases at a rate more than twice that of the squall line (**Figure 6.10 b-c)**, and its rain production efficiencies for rainfall rates <= 10 mm/hr also grow more quickly (**Figure 6.10 k-l).** The rain production efficiency of the supercell is thus growing more rapidly than that of the squall line during this period, even though its updraft mass is also growing more quickly in a fractional sense. In other words, the supercell is not only increasing the mass of its updraft more rapidly than the squall line during this time, but it is also increasing the amount of rain falling at rates <= 10 mm/hr that it produces *per* updraft mass more rapidly. It is thus also increasing the amount of air from regions of this rainfall intensity that it can possibly entrain at a more rapid pace than the squall line during this period.

The squall line attains greater time-averaged, maximum, and end-of-simulation values of the 20 mm/hr and 40 mm/hr rain production efficiencies than does the supercell (**Figure 6.10 h-i)**. This is especially pronounced for the 40 mm/hr rain production efficiency, for which the squall line's end-of-simulation value is more than triple that of the supercell. While we note in the methodology section that our "rain production efficiency" is not equivalent to the "precipitation efficiency" used in some severe storms research, the latter quantity can still help us to contextualize our results around the former. Supercells are known to be low precipitation efficiency storms in that they convert a lesser portion of the vapor that the storm entrains into precipitation that reaches the ground than do other storm morphologies, owing to the high degree of evaporation in the relatively dry forward-flank downdraft where most precipitation is deposited (Foote and Fankhauser 1973; Browning 1977). It is thus perhaps less surprising that, despite the squall line and supercell being initialized in the same moisture environment (**Table 5.1)** and the supercell's updraft being faster (**Figure 6.11 b-c, Figure 6.3 b-c)** which we might

crudely approximate as being proportional to the moisture influx, the supercell still produces less rain per unit updraft mass than the squall line.

We will examine the impact of this factor on the actual rain-sourced tracer mixing ratios in more depth after discussing the metric in the next section, but these results tell us directly that the squall line simply produces more heavy rain per unit of updraft mass than either the supercell or the isolated convective storm. Thus, without even considering factors such as the positioning or depth of the storms' inflow regions or the positioning of rain relative to the storms' updrafts, the squall line simply has more air from these intensely rainy regions that it can possibly entrain.

f Rain-sourced tracer entrainment efficiency

Recall that the *rain-sourced tracer entrainment efficiency* refers to the proportion of the total rain-sourced tracer that has been emitted cumulatively up to a point in time that is present in the updraft of the storm instantaneously at a given point in time. This metric thus captures several factors about each storm, the interactions of which would be difficult to analyze (e.g. the location of its inflow, the speed of its updraft, the position of its rain relative to its updraft), but which combine to determine its overall ability to entrain whatever rainy air it has produced.

The isolated convective storm reaches its peak value of rain-sourced entrainment efficiency for all tracers at t=85-95 minutes (**Figure 6.10 j**), when its updraft mass is near its peak (**Figure 6.10 a)**. These large values of rain-sourced tracer entrainment efficiency are therefore *not* due to the fact that the storm's updraft has decayed and only encompasses a very small number of points, as some of the other extreme values reached by this storm are. However, these large values are still attributable to the timing of the storm's rain relative to its updraft development. The storm's total rainfall rate peaks at t=95 minutes **(Figure 6.3 d)**, and the low-

level updraft decays to near zero rapidly from t=95-105 minutes **(Figure 6.11 a)**. While the storm's total updraft mass is still relatively near its peak value at this time, essentially none of the rain-sourced tracer being produced from this time onward is entrained because there is no updraft at the surface to lift it. Thus, while the isolated convective storm can entrain surface air and produces rain, its updraft entrains less surface air from rainy regions than do the other storms because of the timing of its development. We will describe the mechanism by which rainy air is entrained into the isolated storm in the section on trajectory analysis, where we find that a difference of order ~1 K in the temperature of a parcel can affect its entrainment. The average surface potential temperature in regions of 40 mm/hr rain is 2.4 K less than that of regions of 1 mm/hr rain at t=90 minutes when the isolated convection's rain-sourced tracer entrainment efficiency is at its peak, and this temperature difference therefore physically explains some of the variation in entrainment efficiency between the rain-sourced tracers evident in **Figure 6.10 j**.

Both the squall line and supercell have significant fluctuations over time in their entrainment efficiencies across the rain-sourced tracers **(Figure 6.10 k-l)**, owing to the complicated interplay of the amount of rain that has been produced, the positioning of the rain relative to the storm's inflow, the time required for the tracer to be entrained into the updraft after its production, and the timing of the overall development of the storm itself. The squall line entrains a greater fraction of all rain-sourced tracers that are produced before t=90 minutes than the supercell We can understand why this is based on the rain-sourced tracer entrainment factors we have looked at previously: the supercell has both a lower proportion of surface air in its updraft that originated in rainy regions **(Figure 6.10 e-f)**, as well as a smaller proportion of air in its updraft that originated at the surface that than that of the squall line (and even of the isolated convective storm) during this window of time **(Figure 6.10 b-c).** This results physically from the

later development of its low-level mesocyclone and associated low-level updraft, as discussed in section 3.1c. From about t=120 minutes onward, when the supercell's low-level updraft has strengthened **(Figure 6.11 c)**, the supercell entrains rain-sourced tracer from regions of light rain more efficiently, while the squall line entrains tracer from regions of heavy rain more efficiently **(Figure 6.10 k-l)**.

We can now explain the trends in the rain-sourced tracer mixing ratios in a second way, using the rain production efficiency and the rain-sourced tracer entrainment efficiency. The comparable values between the squall line and supercell of the mixing ratio for the tracers produced in regions with <= 10 mm/hr rainfall rates (**Figure 6.9 k, l**) arise because the squall line produces more light rain per unit updraft mass (at most 1.24x the supercell), but entrains proportionally less of the tracer that this rain produces (at least 0.8x the supercell). These differences are relatively small, which also works to make the resulting rain-sourced tracer mixing ratios comparable. The squall line's larger mixing ratios for the tracers produced at 20 mm/hr and 40 mm/hr of rain arise because it produces more of this rain per updraft mass and entrains more of what it produces; for the 40 mm/hr tracer, the larger difference in mixing ratio is driven by the squall line producing ~7.5x the amount of rain of this intensity that the supercell produces per updraft mass. While the rain-sourced tracer entrainment efficiency captures several factors which interact in ways that would be difficult to isolate, the positioning of rain of different intensities relative to the updraft plays an important role in driving the differences in this metric between the squall line and supercell. The squall line's heaviest rain is positioned close behind the gust front, which we will see in our trajectory analysis is favorable for its entrainment. By contrast, the supercell has a distinct gradient in rainfall rates where the strongest rainfall is tens of kilometers away from the surface updraft, and so less of this air is recirculated

into the updraft compared with the air closer to the updraft that originates from regions of lighter rainfall. The squall line also has significant along-line variation in rain strength, i.e. heavy rain and light rain are positioned more similarly with respect to the updraft than is true of the supercell. This allows it to entrain air from regions of multiple intensities of rainfall.

The maximum value of the rain-sourced tracer mixing ratios attained at about t=90 minutes in the isolated convective storm arises because that is the only time in its life during which it has a reasonably large (in the sense of comparable to the other storm morphologies' values) rain production efficiency *and* rain-sourced tracer entrainment efficiency. Physically, there is only a brief period between the onset of rain and the development of the cold pool, which cuts off low-level inflow to the updraft. As previously discussed, the storm continues to rain after this time as the updraft decays **(Figure 6.3 a, d)**, but the updraft at the surface is soon no longer capable of lofting air from the surface (**Figure 6.11 a**). Thus, the rain-sourced tracer entrainment efficiency plummets, along with its rain-sourced tracer mixing ratio.

g Summary of tracer analysis

We now summarize the results of the foregoing tracer analysis. Our first conclusion from this analysis is that the isolated convective storm briefly entrains air from regions of 1 mm/hr rainfall in quantities that are of the same order of magnitude as those of the two more organized storm morphologies. This maximum concentration is short-lived because the isolated convective storm's updraft begins decaying shortly after this maximum is reached. This updraft decay is initially most pronounced at the surface, thereby preventing the entrainment of further surface air. It reaches this maximum concentration of rainy air in its updraft in the first place because the proportion of air in its updraft that has been in contact with the surface at the time of this

maximum is comparable to the largest concentration of surface air seen in either of the two organized storms. Thus, even though the proportion of the surface air the isolated updraft entrains that is from *rainy* regions is smaller than that of the other storms, it reaches a comparable mixing ratio of the 1 mm/hr rain-sourced tracer because it entrains a large amount of *total* surface air. The isolated convective storm reaches lesser concentrations of the rain-sourced tracers from regions of heavy rainfall compared to the other storms both because it produces less rainfall of this intensity and because it is not able to entrain a significant portion of the air from the regions of heavy rainfall that it does produce. This again is due to the late onset of rain of this intensity relative to the decay of the storm's updraft at the surface, and the more negative buoyancy of this air.

Our second conclusion from this analysis is that the squall line and supercell entrain comparable concentrations of air from regions with rainfall rates <= 10 mm/hr, but that they do so for different reasons. The squall line entrains a larger amount of total surface air than the supercell, but a larger proportion of the surface air that the supercell entrains has been in contact with the surface in regions of this rainfall intensity. The differences in these two factors between the storms are relatively small, and they offset each other such that the two storms' time-averaged mixing ratios of the tracer emitted in regions of 1 mm/hr rainfall are within 1% of each other.

Our third conclusion is that the squall line entrains more air from regions of heavy rain into its updraft than does the supercell, and that this difference (in a ratio sense) increases monotonically with rainfall rate from 1 mm/hr to 40 mm/hr. This arises because the squall line produces more heavy rainfall per updraft mass than does the supercell, and it also entrains more of the air from the regions of heavy rain that it does produce. Relative to the supercell, the squall

line's values of both the rain produced per updraft mass and the fraction of rain-sourced tracer that is entrained into the storm also increase monotonically with rainfall rate from 1 mm/hr to 40 mm/hr.

These results indicate that the potential for bioaerosol transport of each storm depends heavily on the rainfall rate required for aerosolization of these particles. For light rain, the differences between the three storm morphologies are less pronounced. Although the isolated convective storm has only a brief time where it can entrain and transport air from these regions, the amount of air from these regions in its updraft is of the same order of magnitude as that of the organized storms. As such, the entrainment of bioaerosols aerosolized by rain into isolated convective storms is time-limited. The squall line and supercell entrain concentrations of this lightly rainy surface air in their updrafts that are similar to one another. If aerosolization of biological particles requires heavy rain, the isolated convective storm is unlikely to be either microphysically influenced by or an effective transporter of these aerosolized particles because it entrains very little of the air containing such particles. The supercell and squall line both entrain more particles than the isolated convective storm, but the squall line attains significantly greater concentrations than the supercell. Based on this finding, the squall line's potential for the transport of air containing rain-aerosolized bioaerosols is the greatest of the three storm morphologies if this aerosolization requires heavy rain.

3.3 Trajectory analysis

The results of our Eulerian tracer analysis have allowed us to characterize several aspects of deep convective storms' entrainment of air from rainy surface regions where aerosolization of biological particles may be occurring. This tracer-based approach lends itself primarily to an

analysis of the quantity and spatiotemporal distribution of this air in the updrafts of storms. However, much more can be learned about the actual pathways taken by this air as it is entrained into storms by the use of a Lagrangian approach, wherein the positions of individual *parcels* of air are tracked as they are advected with the storm's winds. This allows us to describe not only the spatial pathways taken by rainy and non-rainy surface air as it is entrained into storms, but also the microphysical environments experienced by the parcels as they are entrained. We now present results from offline trajectory calculations in six different settings, corresponding to the six combinations of parcels originating in gridpoints where the rainfall rate is above or below 1 mm/hr (the lowest threshold for rain-sourced tracer emission) in each of the three storms. We first analyze the proportion of parcels entrained within each storm. As counting the number of parcels that are entrained by a specific pathway is infeasible with the number of trajectories that we calculate and the subjective nature of defining a single "pathway", the proportion and timing of parcels entrained (coupled with the spatial origins of the entrained parcels) provides an empirical basis for characterizing the prevalence of entrainment pathways. We then describe the pathways themselves in detail in the following section.

a Proportion of parcels entrained

As discussed in the methodology section, we use a parcel reaching a height of 6 km as the criterion for having been entrained into the storm. We look at (a) whether a parcel is ever entrained into the storm, and (b) whether a parcel is entrained into the storm within 30 minutes of its initialization. The first measure is useful in a physical sense for understanding when parcels that are entrained into the storm are in contact with the surface. However, this measure is biased towards parcels with earlier initialization times which have a longer time over which to be

entrained before the mature or dissipating stages of the storms. The second measure removes this bias, as the last parcel initialization time is 30 minutes before the end of the simulation, and so this metric gives an equal window for all parcels to be entrained.

The proportion of initialized parcels that are ultimately entrained into the storms differs significantly between the storms and between times of parcel initialization (**Figure 6.12 a-c**). However, we note that direct comparisons between the proportion of parcels entrained in *different storms* are not necessarily physically meaningful; as parcels are always initialized in a 100 km x 100 km grid at each initialization, the proportion of parcels entrained into a storm will be a function of storm size. This will lead the larger storms, in this case the squall line due to its meridional extent, to have higher proportions of entrainment, which is what we observe. Thus, comparisons of the proportion of entrained parcels between storms to some degree simply reflect the size of the storm, rather than its entrainment dynamics. Rather, we will analyze the proportions of entrained parcels by initialization time and rain *within* a storm to gain information about the timing of entrainment and the differences in the degree of entrainment between rainy and non-rainy surface air.

The isolated convective storm's largest proportion of entrained non-rainy parcels occurs in the first initialization time at t=50 minutes, and decreases consistently from that point onward (**Figure 6.12 a)**. The locations of entrained parcels in **Figure 6.13 a** illustrate that the general pattern of the isolated convective storm's entrainment is that the convergence at the base of its updraft draws parcels from all directions, as will be discussed in more depth in the next section. The region from which it is able to draw parcels shrinks consistently after the first initialization time, despite that the low-level updraft is still increasing in strength; this results from the time required for the parcels that are initialized further away from the base of the updraft to travel

toward the updraft. In other words, parcels at the edge of the light orange area in **Figure 6.13 a** only have enough time to reach the updraft before it decays at the first initialization time. The extent of the region from which the storm can draw in and entrain parcels before its updraft decays then necessarily shrinks with time. This interpretation is also corroborated by the fact that the proportion of entrained parcels that are entrained within 30 minutes of their initialization increases with time. Physically, this means that the size of the region from which the isolated convective storm's strong surface convergence can draw parcels begins shrinking immediately after it develops a mid-level updraft (which is when we first initialize parcels).

The isolated convective storm's proportion of entrained parcels from rainy regions reaches 70% at the first initialization of parcels where rain is present, but this is an artificially high number driven by the small number of rainy parcels in this initialization (because the size of the storm's rainy region at this time is small) (**Figure 6.12 a)**. The proportion of rainy parcels entrained quickly declines to a small proportion of the parcels. While the exact timing is difficult to compare due to the time required for entrainment, this broadly corroborates our finding of a large spike in the isolated convective storm's rain-sourced tracer entrainment efficiency, followed by a decline to small values. We will see in the next section that the pathway by which this rain-cooled and negatively buoyant air is entrained into the isolated convective storm is very specific, and thus only a small number of rainy parcels are in the correct time and place to be entrained.

The most notable feature of the squall line's proportions of entrained parcels are that nearly none of the non-rainy parcels that the storm entrains are entrained within 30 minutes of their initialization (**Figure 6.12 b)** There are two reasons for this. First, the storm has a significant propagation speed and thus parcels that are initialized 50 km away in its direction of

motion can eventually be entrained (**Figure 6.13 b)**. However, **Figure 6.12 e** indicates that this is not the only reason; parcels entrained into the squall line also take longer to reach the entrainment height of 6km after first reaching a height of 1km as compared to entrained parcels in the other storms. We will outline the reasons for this and the impacts it has on the supersaturation environments experienced by parcels entrained into the squall line vs into the other storms in the sections to follow. We can also see that the squall line's proportion of rainy parcels entrained is comparable to its proportion of non-rainy parcels entrained **(Figure 6.12 b)**, which generally corroborates our findings from the tracer analysis that it has a high rain-sourced tracer entrainment efficiency (i.e. that it entrains a larger portion of the rainy air it produces relative to the other storms).

Of the three storms, the supercell's entrainment timing differs the most significantly between parcels initialized in rainy and non-rainy gridpoints. For most of the storm's life, it entrains about half of its non-rainy parcels within 30 minutes of their initialization. By contrast, of its rainy parcels are entrained within 30 minutes **(Figure 6.12 c)**. Unlike the isolated convective storm which has minimal bulk motion or the squall line which produces some rain in its own path of motion, the supercell's rain moves with the storm but is not directly in the path of its updraft. Thus, only rainy parcels that are initialized sufficiently near the updraft can be entrained at all; the storm's advective velocity generally "outruns" parcels that are initialized further away, as we will see in the following section. This evidently leads to parcels from rainy regions being entrained quickly if they are to be entrained at all. This interpretation also agrees with our assessment of the supercell's lower rain-sourced entrainment efficiency for heavy rain, which is positioned further away from the storm's updraft than its light rain. The longer entrainment times for its non-rainy parcels derive from the phenomenon just discussed for the

squall line: the supercell has significant bulk motion, and parcels initialized far away from the storm's present position can still be entrained if they are in its path of motion.

Having understood the broad patterns of entrainment of our simulated parcels in each storm and compared the conclusions drawn from these patterns with the conclusions drawn from the earlier tracer analysis, we now describe the specific pathways by which parcels are entrained into each storm.

b Entrainment mechanisms

We first present descriptions of the pathways taken by parcels as they are entrained into the simulated storms in order to understand the dynamical processes that drive their transport. These descriptions are based on visual analysis and therefore necessitate some interpretation. We then present quantitative results of the supersaturation environments experienced by entrained parcels in the next section. Each figure **(Figures 6.14, 6.15, 6.16)** presents a visualization of the trajectories of a subset of the parcels entrained by each storm at three different times in the storm's development, along with visualizations of relevant variables from the model output. All parcels depicted are entrained into the storm (i.e. at some point reach an altitude of 6 km), so even those in the later panels of each figure that are still near the surface at the time shown are eventually lofted. The parcels and times shown are selected to clearly and accurately represent the different pathways taken by the population of parcels as a whole as they are entrained into each storm, and parcels from multiple initializations may be present in one figure. We now assess the entrainment pathways for each storm morphology.

Note that in **Figures 6.14, 6.15,** and **6.16**, isosurface contours may be portrayed with different opacities or as wiremeshes vs solid surfaces; these are choices intended to make the

figures clearer and they do not indicate any physical characteristic. The physical values to which the isosurface contours correspond is expressed by their color, and these values are noted in the captions of each figure.

3.3.b.1 Isolated convection

The isolated convective storm initially entrains parcels relatively uniformly from an oval-shaped region surrounding the updraft, with the oval elongated along the forward-rear axis (**Figure 6.13 d)**. The storm begins producing rain at about t=75 minutes and a rainy downdraft region forms in the updraft, as is typical of an isolated convective cell (Byers and Braham 1949). As it develops this rain shaft and downdraft on its forward flank, the storm begins to preferentially entrain parcels from behind and to the sides of the updraft and entrains fewer parcels from its forward flank. This occurs because the air to the front of the updraft is both cooled by the rain and so is negatively buoyant, and because the surface divergence associated with the downdraft drives some of the surface air in the forward region away from the updraft. For a short time, the storm entrains a few parcels from its rainy region **(Figure 6.12 a)** that are near the updraft (**Figure 6.13 a)**. Both rainy and non-rainy parcels are also entrained preferentially from the southern side of the updraft as the storm develops, which results from slightly greater rainfall in the northern half of the storm, and subsequently more evaporative cooling and more negative buoyancy in this region. We now examine the mechanisms by which both non-rainy and rainy parcels are entrained.

Parcels from non-rainy regions are entrained into the isolated convective storm via direct lofting by the updraft as it passes over the surface (**Figure 6.14 a-c**). The convergence of air into the updraft base (the 0-1km mean of the divergence is shown on the surface in **Figure 6.14 a-c**) draws in parcels surrounding the updraft (**Figure 6.14 a**) in addition to those that are directly in

its path. The parcels are then lifted directly to the top of the storm by the updraft (**Figure 6.14 b**). Some parcels oscillate around the level of neutral buoyancy at the top of the storm **(Figure 6.14 c, annotation A)**, while some begin descending **(Figure 6.14 c, annotation B)** but ultimately remain at upper levels **(Figure 6.4 a)**. Additionally, it is possible to see some parcels being lofted into the updraft via a circulation in the head of the cold pool **(Figure 6.14 c, annotation C)** which we will now discuss in more depth, as it is also the mechanism by which the isolated convective storm entrains parcels from regions of rain.

Parcels in rainy regions of the isolated convective storm, which are found inside the cold pool and which are negatively buoyant, depend on the circulation within the leading edge of the cold pool to overcome this negative buoyancy and thus be entrained into the updraft (**Figure 6.14 d-f**). Parcels from rainy regions behind and on the sides of the updraft (relative to the overall stormwise motion) flow outward via divergence associated with the cold pool. These parcels are lifted and reverse direction as they reach the overturning circulation inside the head of the cold pool, as evidenced by the horizontal vorticity in this region (**Figure 6.14 d,** magnitude of z=0-1 km mean horizontal vorticity indicated with purple shading on surface). Initially called a "precipitation roll" (Wakimoto 1982), the existence of this circulation inside the head of a cold pool is a relatively well-noted phenomenon in observations and models (e.g. Wakimoto 1982; Rotunno et al. 1988; Seigel and van den Heever 2012; Solomos et al. 2012). These parcels then flow back towards the updraft (**Figure 6.14 e**). The updraft begins decaying at the surface shortly after the onset of rain (**Figure 6.3 d, Figure 6.11 a**). This process is visible in **Figure 6.14 e, annotation A**, in that the set of updraft contours associated with the updraft core (i.e. not those of the gust front) no longer extends to the surface. As the updraft decays at both the top and bottom of the storm before it does so at mid-levels (**Figure 6.11 a)**, only rainy

parcels that have experienced an initial lofting by the cold pool in this way are able to reach the updraft core and be entrained into the storm (**Figure 6.14 f**). We note that, unlike any of the other entrainment mechanism figures, **Figure 6.14 d-f** depicts *all* of the 27 parcels across all initialization times that both originate in rainy regions and are entrained into the storm. Thus, this appears to be the only pathway by which air from rainy regions is entrained into the isolated convective storm.

Many more rainy parcels in the cold pool undergo the circulation in the cold pool head just described than are actually entrained into the storm by this mechanism (not shown). The parcels that are ultimately entrained are those positioned near the updraft and towards the trailing edge of the cold pool at initialization (**Figure 6.13 d)**, and on the southern flank of the storm as previously mentioned. However, the small number of rainy parcels that are entrained into the isolated convective storm, even given the smaller size of its rainfall region relative to the other storms, corroborates that undergoing the aforementioned circulation in the head of the cold pool does not mean that a parcel will necessarily be entrained into the storm.

3.3.b.2 Squall line

Parcels originating in non-rainy regions ahead of the leading edge of the squall line are first lofted over the gust front of the cold pool via the mechanism of gust-front lofting (Fierro et al. 2009; Seigel and van den Heever 2012) (**Figure 6.15 a**), in which the cold dense air of the cold pool lifts the relatively warmer air of the environmental base state. After being lofted over the gust front, the parcels move with the overturning circulation in the leading edge of the cold pool (the z=0-1 km mean of the meridional vorticity is shown as the orange-to-purple shading on the ground in **Figure 6.15 a-c**). The parcels first descend back to just above ground level in the sinking branch of this circulation (**Figure 6.15 b, annotation A)**. They then follow its rising

branch, i.e. the circulation immediately inside the leading edge of the cold pool (**Figure 6.15 b, annotation B),** similarly to the entrained parcels that are initialized in rain in the isolated convective storm. This rising-sinking-rising motion gives their trajectories a "loop" shape when depicted in a storm-relative sense. After undergoing this circulation in the head of the cold pool, the parcels' motion is then backwards relative to the motion of the cold pool edge (**Figure 6.15 b, annotation C**).

At this point in the process of the squall line's entrainment of parcels from ahead of the cold pool, the 3-dimensional nature of the squall line begins to influence the entrainment pathways. As it matures, the squall line develops points at which the gust front bulges out in the direction of storm motion relative to the rest of the line **(Figure 6.7 a, annotation A)**, as well as regions where it does not extend as far in the direction of storm motion as the rest of the line **(Figure 6.7 a, annotation B)**. In section 3.1b we named these features convex regions and concave regions, respectively. As can be seen from the filled blue contours in **Figure 6.7 a**, the convex regions coincide in the meridional direction with the largest and most intense areas of rainfall behind the gust front. The zonal velocity (i.e. the velocity in the direction of the storm's propagation), shown in the dashed grey contours, indicates that these convex regions occur because these regions of intense rain develop a larger storm-relative velocity than do the regions between them, driven by the divergence associated with this heavier rain. The cold pool in these regions thus "runs out ahead" of the storm.

The effects that the storm-parallel heterogeneity in the cold pool and the convective structure of the updraft has on entrainment can be seen in **Figure 6.7 b.** In the regions where the cold pool is propagating more quickly, the 4 m/s updraft isosurface is discontinuous between the gust front and the updraft core behind it. This spatial disconnect between the gust front's updraft

and the mid-level updraft is a known feature of some squall lines that has been both simulated and observed (e.g. Jorgensen et al. 1997; Fierro et al. 2009; Seigel and van den Heever 2013). We further observe downdrafts in these disconnects (indicated by the pink isosurfaces in **Figure 6.7 b**) which are similar to the convective downdrafts behind the gust front observed by Uebel and Bott (2015). By contrast, the positive updraft isosurface is continuous from the gust front to the updraft core in the concave regions. The effects of this are twofold. First, the parcels that originate near the concave regions are entrained at a greater rate than parcels that are initialized near the convex regions. This can be seen in the initial storm-relative positions of parcels that are ultimately entrained into the squall line **(Figure 6.13 e)**, where the meridional regions from which the most parcels are entrained correspond to concave regions in the gust front. This is primarily because these parcels experience continual modestly strong (>= 5 m/s) lifting from the time they encounter the gust front, whereas parcels in regions where the positive updraft isosurface is discontinuous often sink back down into the cold pool or are not at a high enough vertical level to be entrained and pass beneath the updraft core (**Figure 6.7 b)**. These parcels then continue to move backwards relative to the storm at the same approximate height until the simulation ends (not shown). A secondary reason for the greater rate of entrainment of parcels originating near concave regions is that some of these regions have "tails" of low-level convergence behind them **(Figure 6.7 a, annotation C)**. As the convex regions are regions of relatively more intense rainfall, the downdrafts and evaporative cooling associated with this rainfall create stronger low-level divergence in these areas. This drives the bulging of the cold pool as mentioned earlier, but it also creates low-level *con*vergence in the concave regions where these divergent outflows meet. This convergence is weak compared to, for example, the low-level convergence at the gust front itself, but it does create updrafts of up to 2 m/s in the z=0-

1km mean that are coincident with the regions of convergence (not shown). Thus, this convergence actually strengthens the updrafts in these concave regions, thereby contributing to the spatial continuity of the updraft (**Figure 6.7 b)**. We will also see that this distinction in entrainment pathways is microphysically significant in that parcels that are entrained from convex regions spend significantly longer in supersaturated environments during their entrainment than do parcels entrained from concave regions.

Parcels originating in the rainy region within the cold pool are entrained similarly to those originating ahead of the cold pool once they have been lifted over the gust front and returned to the surface via the descending branch of the cold pool head's circulation. This can be seen in **Figure 6.15 d-f,** where all depicted parcels originate in rain, but the blue trajectories represent parcels initialized in the cold pool while the yellow trajectories represent parcels initialized in the narrow band of rain ahead of the cold pool. The parcels initialized in the cold pool are only entrained if they are initialized right behind the leading edge of the cold pool, where they undergo the previously-described overturning circulation in the cold pool head. They are then lofted to upper levels by the updraft in the same manner described for parcels originating ahead of the cold pool. The parcels from the rainy region ahead of the cold pool have similar entrainment pathways to those initialized in non-rainy regions ahead of the cold pool in that they are lifted over the gust front, lifted and recirculated in the cold pool head, and are then entrained by the updraft core.

The key features in the initial locations of parcels entrained by the squall line (**Figure 6.13 b)** are twofold. First, for rainy parcels, only the parcels initialized in the portion of the rainy region closest to the gust front are entrained. Those from further behind the gust front do not ever reach the cold pool head and undergo the requisite recirculation mechanism by which the squall

line generally entrains parcels; they instead fall further and further behind the storm as the simulation progresses. Second, the regions from which parcels are entrained exhibit clusters in the along-line (i.e. y) direction. These clusters correspond to the aforementioned concave regions where low-level convergence provides an additional source of lifting. This aids these parcels in reaching a height at which they are entrained into the higher velocity regions of the updraft and are then transported to the top of the storm.

3.3.b.3 Supercell

The primary mechanism by which parcels from outside of the cold pool of the supercell are entrained into the updraft (**Figure 6.16 a-c)** is the gust-front lofting mechanism mentioned previously. The cold, dense air of the cold pool lifts warmer surface air up and over the gust front to a level where the updraft is stronger, and the parcels are then entrained into the storm rapidly. The main way in which the entrainment of these parcels differs from that of the parcels originating outside of the squall line's cold pool is in their flow prior to the actual gust front lofting. In **Figure 6.16 b-c**, it is evident that the parcels that are still at the surface flow in an arc around the forward flank of the storm and towards the updraft. This flow is driven both by convergence at the surface associated with the updraft and by divergence at the surface associated with the forward-flank downdraft. This "recycling" of air from the forward-flank downdraft's outflow is a known phenomenon of supercells (Lemon and Doswell 1979; Rotunno and Klemp 1985; Shabbott and Markowski 2006). By contrast, as can be seen from the storm-relative initial locations of non-rainy parcels that are ultimately entrained into the supercell **(Figure 6.13 f)**, parcels from the rear-flank downdraft (RFD) are not entrained into the supercell. While these parcels are initially driven towards the general region of the updraft by its associated low-level convergence and the surface divergence of the RFD, their horizontal velocity is less

than that of the updraft, and they are essentially outrun by the storm, falling further behind in the cold pool as the storm progresses (not shown).

The trajectories depicting the entrainment of parcels originating in rainy regions (**Figure 6.16 d-f**) include parcels originating both inside the forward flank downdraft's (FFD) cold pool and in the rainy regions associated with the FFD just outside of it. Unlike the squall line and isolated convective storm, the supercell's entrainment of parcels originating in rainy regions does not depend on recirculation by the head of the cold pool. The parcels originating in rain falling outside of the cold pool are entrained in much the same way as parcels originating in non-rainy regions outside of the cold pool, in that they travel in an arc around the forward flank and towards the updraft where they are lofted into the updraft by the gust front. The entrainment of parcels that originate in rainy regions within the cold pool relies on the fact that the updraft of a supercell is strongly dynamically forced and can loft rain-cooled and negatively buoyant air that other storms cannot (Lemon and Doswell 1979; Rotunno and Klemp 1985; Shabbott and Markowski 2006); these parcels travel in a similar arcing shape within the cold pool, and are then directly entrained and lifted by the base of the updraft.

The entrainment mechanisms identified here agree well with the existing supercell literature, and in particular with the supercell dust entrainment mechanisms found in Seigel and van den Heever (2012). They find that upward dust fluxes into the updraft of their simulated supercell occur nearly entirely at the gust front of their storm's RFD cold pool, and that "[w]hile haboobs are associated with large concentrations of dust kicked up within the cold pool, the majority of this dust may not make it into the parent storm's updraft." When considering the RFD and its cold pool, we find the same result: essentially no parcels that originate in the RFD cold pool are entrained into the supercell updraft, and most entrained surface parcels originate

ahead of the storm and are entrained into the updraft by lofting at the gust front of the RFD's cold pool. However, Seigel and van den Heever (2012) focus primarily on the rear-flank downdraft and its cold pool, and not on the forward-flank downdraft nor its cold pool. This is due to the fact that drier land surfaces emit dust more easily than moister land surfaces. More precipitation is produced within the FFD compared with the RDF, resulting in more dust emission occurring in association with the RFD. Thus, our finding that up to ~25% of parcels initialized in rainy regions are entrained into the supercell **(Figure 6.12 c)**, including those originating in the cold pool of the FFD, comports with both the findings of Seigel and van den Heever (2012) and the aforementioned mechanism of recycling of air from the FFD outflow that has been identified in the literature.

c Microphysical environments of parcel trajectories

A quantity of interest for assessing the potential microphysical impact of biological particles aerosolized by rain that cannot be assessed with the tracers of 3.2, but which can be assessed with the parcel trajectory approach, is the time spent by an entrained air parcel in environments of potential microphysical activity (**Figure 6.12 g-i**). We quantify this by calculating the total time spent by entrained parcels in environments with greater than 100% relative humidity, i.e. environments that are supersaturated with respect to water. This is possible because the RAMS model does not make use of saturation adjustment as is often done in mesoscale and cloud-resolving models. Saturation adjustment approaches convert all excess water vapor (supersaturation) to liquid water in each timestep. RAMS rather prognoses condensation rates based on the environmental conditions, vertical velocity and aerosol population.

Across all three storm morphologies, the largest difference in the mean time spent in supersaturated environments between parcels initialized in non-rainy points and parcels initialized in rain is that of the isolated convective storm. During the first time at which there are any rainy parcels, the non-rainy parcels spend an average of nearly 200 s longer in supersaturated environments. These values are again driven by the isolated convective storm's small rainy region and the storm's resulting small number of rainy parcels, as well as the fact that the storm decays beginning at about t=95 minutes. The squall line has the longest mean residence time in supersaturated regions for both rainy and non-rainy parcels at nearly all initialization times. Further, while the isolated convective storm and supercell have mean residence times that vary considerably by initialization time, the squall line's mean residence time for both rainy and non-rainy parcels fluctuates with initialization time by a much smaller proportion.

Depictions of some of the squall line parcel trajectories that spend the longest time in supersaturated environments (**Figure 6.17**) indicate the general pathway by which these parcels move through this storm type. There are 157 entrained parcels across all initialization times which spend 1800 s or longer in supersaturated environments; of these, 139 are initialized in non-rainy gridpoints, and 18 are initialized in rainy gridpoints. Some of these parcels first experience a transient supersaturation as the squall line develops, in which they are lifted by the updraft at the leading edge of the cold pool, but are then transported back down to the surface by the downdraft immediately behind it **(Figure 6.17 a-b, annotations A and B)**. However, not all parcels with supersaturation times of at least 1800 s have this feature of experiencing supersaturation during lofting over the gust front, and its contribution to the overall time spent in supersaturation is small. The more significant contributor to the overall saturation time is the process in which parcels are recirculated from the head of the cold pool into the updraft.

Supersaturation generally begins around the point at which the parcels reach the top of the circulation in the cold pool head and are sent backwards in a storm-relative sense **(Figure 6.17 b, annotation C)**. Because the updraft of the squall line is tilted upshear, the strongest portion of the updraft is located further behind the leading edge of the cold pool (in a horizontal and vertical sense), and these parcels then travel backwards relative to the storm for a time, gaining in height as they do so. The parcels experience supersaturation for most or all of this time. This motion generally takes approximately 15-20 minutes for the parcels with the longest times spent in supersaturated environments, which contributes a significant portion of the total time spent in supersaturation. Finally, the parcels reach the stronger updraft core behind the gust front and are lofted to upper levels, also experiencing supersaturation as they do so.

d Summary of trajectory analysis

The foregoing analysis allows us to describe the pathways by which surface parcels from both rainy and non-rainy regions are entrained into the three storm morphologies we study in this work, an insight that the Eulerian tracer analysis alone cannot provide. We first find parcels entrained into the squall line also spend much longer in supersaturated environments and take longer to rise from z=1 km to z=6 km, owing to its upshear tilt and heterogeneity in the along-line (i.e. perpendicular to flow) direction of the storm. By contrast, a larger proportion of the parcels that the supercell entrains are entrained within 30 minutes of their initialization, and parcels entrained into the supercell do not spend as long in supersaturated environments. Such differences in time spent in supersaturated regions and time spent in transport to upper levels will have significant implications for the microphysical influence of the bioaerosols (and any aerosols) being borne by this air although, as we note in the introduction and methodology,

neither the tracers nor the trajectories we use here can be directly mapped to actual aerosol particles, and so the specifics of this microphysical influence are a topic for another work.

We also describe the pathways taken by entrained parcels in each of the storms and find that they differ both between storm morphologies and between parcels that are/are not initialized in rain. The isolated convective storm type can directly entrain non-rainy surface air by virtue of its strong surface convergence, and it primarily does so before it develops rain and an associated cold pool which work to cut off the low-level updraft inflow, thereby decaying the storm. On the other hand, the squall line and the supercell entrain non-rainy parcels from ahead of their cold pools by gust-front lofting near their updrafts. The isolated convective storm and squall line entrain rainy air with the help of the horizontal vortical circulation in the head of their cold pools, which provides parcels with some initial lofting and directs them toward the updraft. In the squall line, some rain falls ahead of the cold pool; parcels originating there are lofted at the gust front like non-rainy parcels, and then undergo the circulation just described for the rainy parcels originating within the cold pool. Along-line 3D effects in the squall line also play a role in determining whether a parcel will be entrained, as heterogeneities in rainfall create low-level downdrafts in some regions just behind the cold pool's gust front. These downdrafts create divergence at the surface, and these divergent outflows in turn create convergence where they meet, thereby generating low-level updrafts of up to 2 m/s. Thus, the localized regions associated with the downdrafts entrain fewer parcels and the regions with the updrafts strengthened by surface convergence entrain more parcels. Finally, the supercell entrains rainy parcels from just outside of and just inside of the leading edge of the forward-flank downdraft's cold pool.

These findings help further explain observations from the tracer analysis. The isolated convective storm entrains so much surface air during the period of its strongest updraft because

of the convergence associated with its low-level inflow which draws parcels from all directions, whereas the more organized storm types have specific directions relative to the storm motion from which they entrain surface air **(Figure 6.13 a-f)**. One reason that the squall line can entrain air from rainy regions so effectively, and especially so from regions of heavy rain, is that some of its rain falls ahead of the cold pool, where the surface air is less negatively buoyant than it is inside the cold pool **(Figure 6.13 b)**. The horizontal vortical circulation in the head of the cold pool helps provide further lofting after this rainy air is lofted over the gust front. The supercell entrains less air from regions of heavy rain than the squall line because the aforementioned FFD regions from which it entrains rainy air are regions of light rain. Parcels initialized in regions of heavy rain in the supercell are mostly too far away from the updraft to be entrained; the updraft's horizontal motion is faster than the advecting velocity of these regions, and thus they fall further behind the updraft and are not entrained.

Chapter 4 CONCLUSIONS

4.1 Summary and implications of key findings

This thesis had two overarching goals, which are related but worth disambiguating. The first goal was to assess the degree and spatial distribution of entrainment of air from the surface that occurs in three deep convective storm morphologies. We analyze the entrainment both of surface air overall and of surface air from regions where the potential for rain-induced aerosolization of biological particles exists. The second goal was to characterize both the pathways by which this air is entrained into each storm morphology and the supersaturations experienced by these surface air parcels as they are transported within and by each storm. We addressed the first of these goals through the analysis of the transport of inert tracer quantities in idealized simulations of an isolated convective storm, a squall line, and a supercell conducted using a cloud-resolving model, and the second by calculating and analyzing the trajectories of air parcels initialized at different times and in different locations throughout the life cycle of these simulated storms. From our results we draw the following conclusions:

1. The squall line and supercell attain and sustain greater concentrations of rain-sourced tracer across rain thresholds as compared to isolated convection. This indicates that a greater magnitude of air is entrained from rainy surface regions by the more organized storm morphologies as compared to the isolated convective storm. The isolated convective storm's rain-sourced tracer concentrations are closer to that of the organized storms for light rain than for heavy rain rates. The squall line and supercell achieve similar values for light rain, but the squall line achieves a greater concentration of tracer originating in regions of heavier rainfall. These results together indicate that the more

organized storm morphologies entrain and transport more of this potentially bioaerosol-rich rainy air than does the isolated convective cell, and that the squall line entrains more air from regions of heavy rain than does the supercell.

2. The isolated convective storm reaches a peak concentration of total surface air that is comparable to those of the other two storm morphologies. It is also able to briefly reach concentrations of lightly rainy air comparable to those of the other two storms because its surface inflow contains the largest portion of lightly rainy air at about the time when the inflow itself is strongest, owing to the timing of its updraft and rain development. The squall line and supercell entrain similar amounts of air from light rain, but for different reasons: the squall line entrains a lot of surface air, less of which is from regions of light rain, while the supercell entrains less surface air, but more is from regions of light rain. The squall line entraining large quantities of surface air is broadly consistent with the findings of Fierro et al. (2009), in which most tracked boundary layer parcels ahead of a simulated squall line are entrained and lofted to the upper troposphere. The fact that the supercell does not entrain much surface air until later in the simulation is consistent with the findings of Coffer et al. (2023), who noted that the midlevel mesovortex and its associated updraft entrain some air from above the surface, but that the low level mesocyclone (which develops later both in our simulation and in conceptual models (Davies-Jones 2015)) entrains air almost entirely from the surface. We would thus expect the proportion of surface air in the updraft to increase as the low-level mesovortex develops, which we observe.
3. The isolated convective storm entrains much lower proportions of air from regions of heavy rain into its updraft because only a very small proportion of its in-updraft surface

air is from these regions as compared to the other two storms. Physically, this occurs primarily as a consequence of the cooler and more negatively buoyant air associated with heavy rain, which is more difficult for the weaker isolated storm updraft to lift. The squall line entrains more air from regions of heavy rain both because it entrains more surface air and because a larger proportion of this entrained surface air is from regions of heavy rain compared to that of the supercell. Our trajectory analysis shows that this is because the supercell's entrained rainy air originates mainly from regions of light rain outside and just inside the leading edge of the FFD's cold pool, while the regions of heavy rain are positioned further away from both this region and the surface updraft itself, and the air from these regions cannot "catch up" to the rapidly propagating updraft. The proportions of entrained surface parcels originating in rainy air are consistent with the proportion of low-level mesocyclone inflow originating in negatively buoyant and precipitating air found in Coffer et al. (2023). By contrast, the variation in the squall line's rain intensity is primarily in the direction along the squall line, and so regions of heavy rain and light rain are positioned similarly relative to the head of the cold pool where the air from these regions is lofted. Some rain in the squall line also falls just in front of the gust front, where the strong convergence and lifting is sometimes able to loft it into the updraft core.

4. The physical mechanisms behind these results can also be understood in terms of how much rain of a given intensity a storm produces per updraft mass, and what fraction of the air from these regions (measured via tracers) is subsequently entrained. The differences in the storms' evolutions complicate this comparison, but the isolated convective storm broadly produces less rain of any intensity per updraft mass than either

of the other two storms. It is able to briefly reach comparable rain-sourced tracer concentrations for light rain at about the time of the storm's peak rain and updraft mass because it entrains a larger fraction of the air from regions of light rain at this time than do either of the other storm morphologies at any point. It produces minimal heavy rain and entrains only a small fraction of what it produces and thus is only able to entrain low concentrations of air from these regions. The squall line and supercell produce similar quantities of light rain per unit updraft mass and entrain similar fractions of the air from these regions, leading to their comparable tracer concentrations from light rain regions. The squall line both produces more regions of heavy rainfall and entrains more of the air from the regions of heavy rain that it produces, the latter occurring for the physical reasons described in the previous conclusion. It thus entrains greater concentrations of the heavy rain tracers.

5. The mechanisms by which air parcels originating at the surface are entrained into the different storm types varies widely between morphologies and by whether surface air originating in rainy or non-rainy regions is considered. Surface parcels originating in areas without rain are entrained into the isolated convective storm directly by the updraft and its associated convergent flow at the surface, but these parcels are entrained into the squall line and supercell via gust front lofting along the edges of their cold pools. Parcels from rainy regions are entrained into both the isolated convective storm and the squall line by the overturning circulations associated with the horizontal vorticity in the head of the cold pool, which provides initial lofting and subsequently redirects parcels towards the updraft core in a storm-relative sense. Many more parcels undergo this circulation than are ultimately entrained, with actual entrainment depending on a combination of the

timing and positioning with which the parcel is initialized that allows the parcels to reach the updraft core in some times and places. Rainy parcels are entrained into the supercell by the recycling of rainy air from the regions just inside and outside of the forward-flank downdraft's cold pool, some of which is then lofted by the gust front and some of which is lofted by the updraft directly from within the cold pool. These circulations are well-documented in the literature.

6. The distribution of time spent by entrained surface parcels in supersaturated environments is similar between the isolated convective storm and the supercell, with nearly all parcels spending <1000s in supersaturated regions. This average time is longer in the squall line, with over half of parcels spending 1000s-2000s in supersaturated environments. This results from inhomogeneities in the squall line in the along-line direction that cause some parcels to pass through supersaturated downdrafts after they are recirculated in the head of the cold pool. Some of the parcels that take this pathway are then not entrained, as the squall line's updraft tilts upshear and this downward motion positions the parcels below and away from the updraft. Those that are still entrained experience very long times in supersaturation along their entrainment pathway as a result. The spatial separation of the gust front updraft and the updraft core has been observed previously (e.g. Jorgensen et al. 1997; Fierro et al. 2009; Seigel and van den Heever 2013), and Uebel and Bott (2015) observed the descent of parcels from ahead of the storm into the cold pool due to convective downdrafts behind the gust front. However, to our knowledge, this is the first observation that these parcels can still be entrained into the updraft and lifted to the upper troposphere after encountering these downdrafts, and that they experience long supersaturation residence times as they do so.

As discussed in the introduction, a number of previous studies have examined various aspects of the transport of aerosols by and within DCCs (e.g. Engström et al. 2008; Froyd et al. 2009; Tulet et al. 2010; Seigel and van den Heever 2012; Herbener et al. 2016). Our findings contribute to this understanding by characterizing the method, environment, and relative quantities of the transport of air containing bioaerosols emitted during rain, a mechanism which has not yet been investigated in storm-scale transport studies. Further, we not only gain an understanding of the relevance of three different storm morphologies in transporting bioaerosol by comparing them directly, but the entrainment pathways of surface air, including in different precipitation settings, have until now not been directly compared between deep convective storm morphologies using a consistent methodology.

There are a number of limitations to the foregoing conclusions. One limitation of this study is that, by using tracers to track the locations of *air* carrying rain-aerosolized biological particles, we do not account for the effects of aerosol-specific processes that affect bioaerosol transport. One of the most significant of these processes in this context is wet deposition, which we noted in the introduction has been shown to reduce the fraction of dust entrained into deep convective storms that is then able to reach the upper troposphere (Tulet et al. 2010; Herbener et al. 2016). We have been careful throughout this study to discuss the transport of air containing bioaerosols, rather than the bioaerosols themselves, because the tracers we use cannot be directly extrapolated to bioaerosol particles for this reason.

While the storms we simulate are representative examples of their morphologies, it is surely possible to vary the initial conditions of each to some degree and still simulate a representative storm of each type, which could impact the results presented here. Chiefly, the

environmental background state of each storm (which, with the initial forcing, is the only physical variations between the simulation setups) may influence the factors that determine the rain-sourced tracer concentrations of each storm. Changes in the strength and depth of the wind shear in which a simulated squall line is initialized have been found to impact the entrainment and precipitation characteristics of the storm, as well as the strength of the updraft itself (Mulholland et al. 2021). The aforementioned study also found that the size of a squall line's updraft can affect the degree of entrainment-driven dilution of its updraft, with larger updrafts being less dilute, and thus the size of the simulated storm could impact the tracer concentrations observed through this mechanism. More generally, shear has been found to correlate negatively with the precipitation efficiency (the ratio of precipitation reaching the ground to the inflowing water vapor) of convective storms (Foote and Fankhauser 1973). Changes to the shear environment could therefore change the precipitation characteristics of the storms even in an identical moisture background state. Thus, even within a storm morphology there are factors in the simulation environment which could impact these results, and our simulations inherently represent only one possible choice of these factors for each storm, albeit a set of well-tested and analyzed environmental parameters (Weisman and Klemp 1982, 1984).

4.2 Future work

This paper contributes to an understanding of the storm-scale transport of bioaerosols in deep convective storms. This analysis opens many further questions about the transport and impact of rain-aerosolized biological particles in and on deep convective storms.

The next step in the research presented here is to represent rain-aerosolized biological particles in idealized simulations like those presented here explicitly as microphysically active

aerosol particles, rather than as inert tracers. With the deeper understanding of their transport in the absence of their microphysical influence gained by this research, their microphysical impacts on the dynamics of the storms will be easier to isolate. Explicit representations of the freezing and emission activity of pollen have recently been utilized in models (Matthews et al. 2023; Subba et al. 2023; Zhang et al. 2024), and this foundation of previous research will further facilitate this effort.

Field observations are necessary in addition to the existing pollen emission and freezing parameterizations for several reasons. First, there does not as yet exist a rain aerosolization mechanism for bioaerosols that has been implemented in a model, in part because the quantitative parameters of this emission are poorly understood. Additionally, the spike in aerosolized biological particles associated with rain is thought to consist of several types of biological material besides pollen, which may have different freezing activity. The BioAerosols and Convective Storms (BACS) field campaign collected aerosol samples and meteorological data under conditions which allow for the development of such a parameterization. These observations will be useful in developing such an aerosolization parameterization for high-resolution cloud models.

With this fuller picture of bioaerosol emission and microphysical influence implemented into a model, data from the ESCAPE (Kollias et al. 2023) and TRACER (Jensen et al. 2023) field campaigns, which collected extensive aerosol, microphysical, and meteorological data during convective events near Houston, can be utilized to construct case study simulations. Such case studies would allow for the characterization of bioaerosol transport and microphysical influences in deep convection, but with the fidelity to nature that comes with observed events

rather than idealized simulations, and would thus further deepen our understanding of the role of bioaerosols and their transport in deep convection.

Chapter 5 TABLES

Table 5.1 RAMS settings used in simulations

Model Parameter	Description		
	Isolated deep convection	**Squall line**	**Supercell**
Model	RAMS v6.3.04 (Cotton et al. 2003; Saleeby and van den Heever 2013; van den Heever et al. 2022)		
Timestep	1 s		
Output frequency	5 minutes		
Microphysics	Full bin-emulating bulk microphysics (Meyers et al. 1997)with 2 liquid and 5 ice hydrometeor species (Saleeby and Cotton 2004), ice nucleation parameterization described in DeMott et al. (2010)		
Radiation	Off		
Horizontal grid spacing	500 m		
Vertical grid spacing	Starts at 25m, stretched with a stretching ratio of 1.1 up to a max spacing of 250m and max height of 22.8km		
Turbulence	Smagorinsky (Smagorinsky 1963) with stability modifications by Lilly (1962) and Hill (1974)		
Lower boundary	Free-slip		
Horizontal boundaries	x: radiative y: radiative	x: radiative y: cyclic	x: radiative y: radiative
Top boundary	Rayleigh dampening layer applied in the upper 2km with a dissipation timescale of 60s		
Convective initiation	2 K warm bubble	-4 K cold bubble, infinite in y	2 K warm bubble
Domain size	375km x	475km x 375km	425km x 300km

	220km		
Weisman-Klemp (1984) initial profile	5 m/s shear Straight hodograph 11 g/kg max vapor MR	15 m/s shear Straight hodograph 13 g/kg max vapor MR	34 m/s shear Curved hodograph 13 g/kg max vapor MR
Initial aerosol profile	Sulfates and dust; concentration decreases linearly from 100 cm^{-3} at the surface to 10 cm^{-3} at 4km AGL, constant at 10 cm^{-3} above 4km AGL		

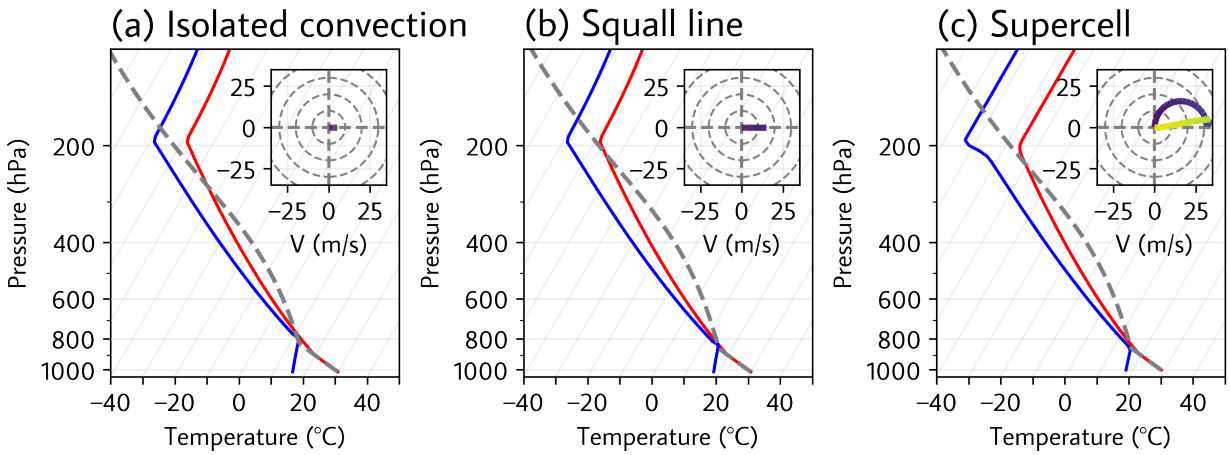

Figure 6.1 The Weisman-Klemp (1984) sounding was used to initialize all the simulations. The only variations between storms are in the low-level moisture, the strength of the vertical shear, and whether the vertical shear is unidirectional or veering with height. Values of these parameters for each storm are given in Table 5.1.

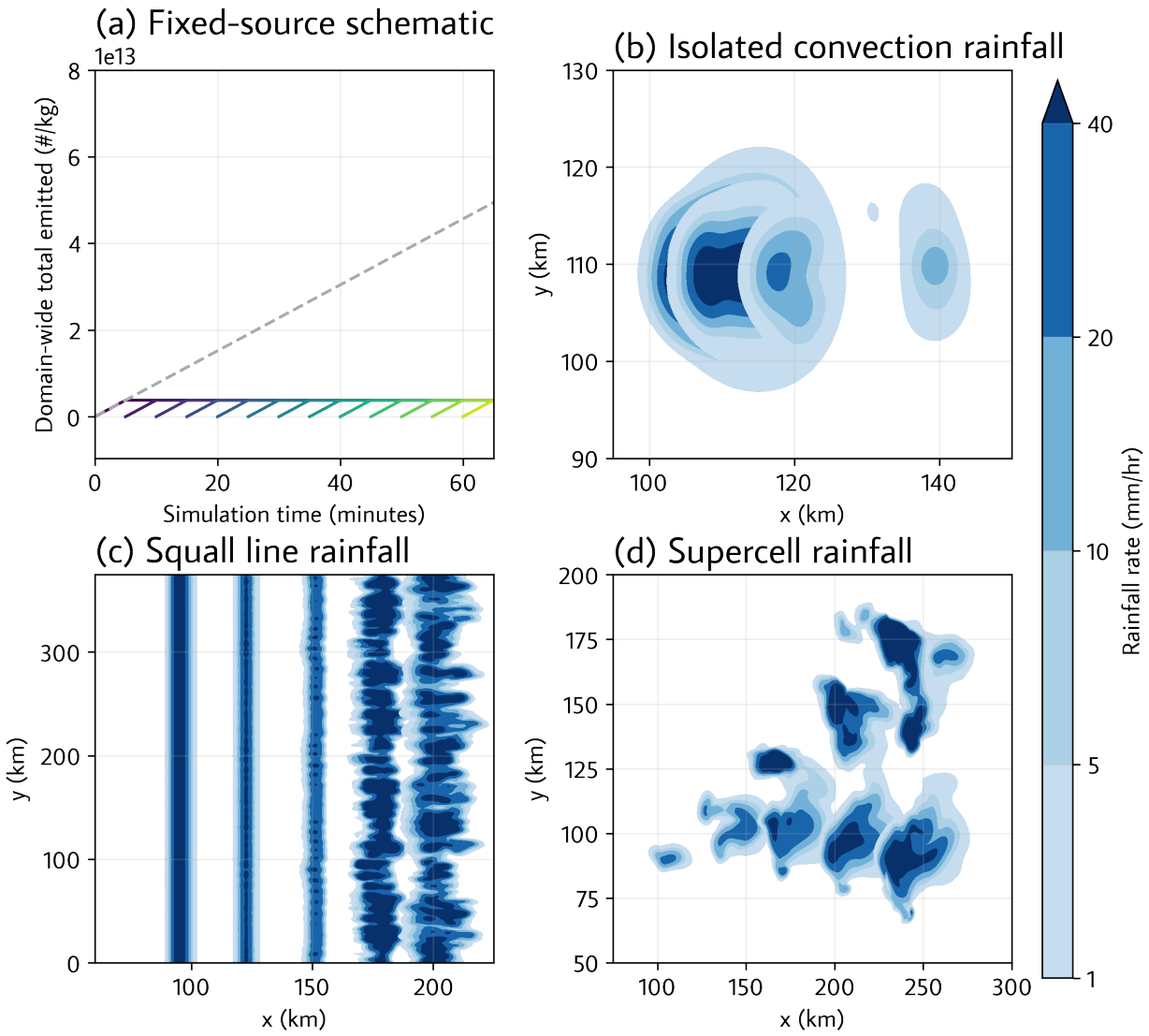

Figure 6.2 Schematics of the fixed-source and rain-sourced tracer emissions. Panel (a) shows the total amount of fixed-source tracer emitted in the whole domain vs time. Each colored line represents a different tracer species. The grey dashed line is the sum of the colored lines and therefore shows the total fixed-source tracer emitted, which is linear in time. Panels (b-d) are plan views of contours of the surface rain rate at 30-minute intervals in each storm. The five shades of blue correspond to regions where the surface rain rate exceeds each of the five rain-sourced tracer emission rain rate thresholds, and therefore to regions where each tracer species is being emitted at that point in time.

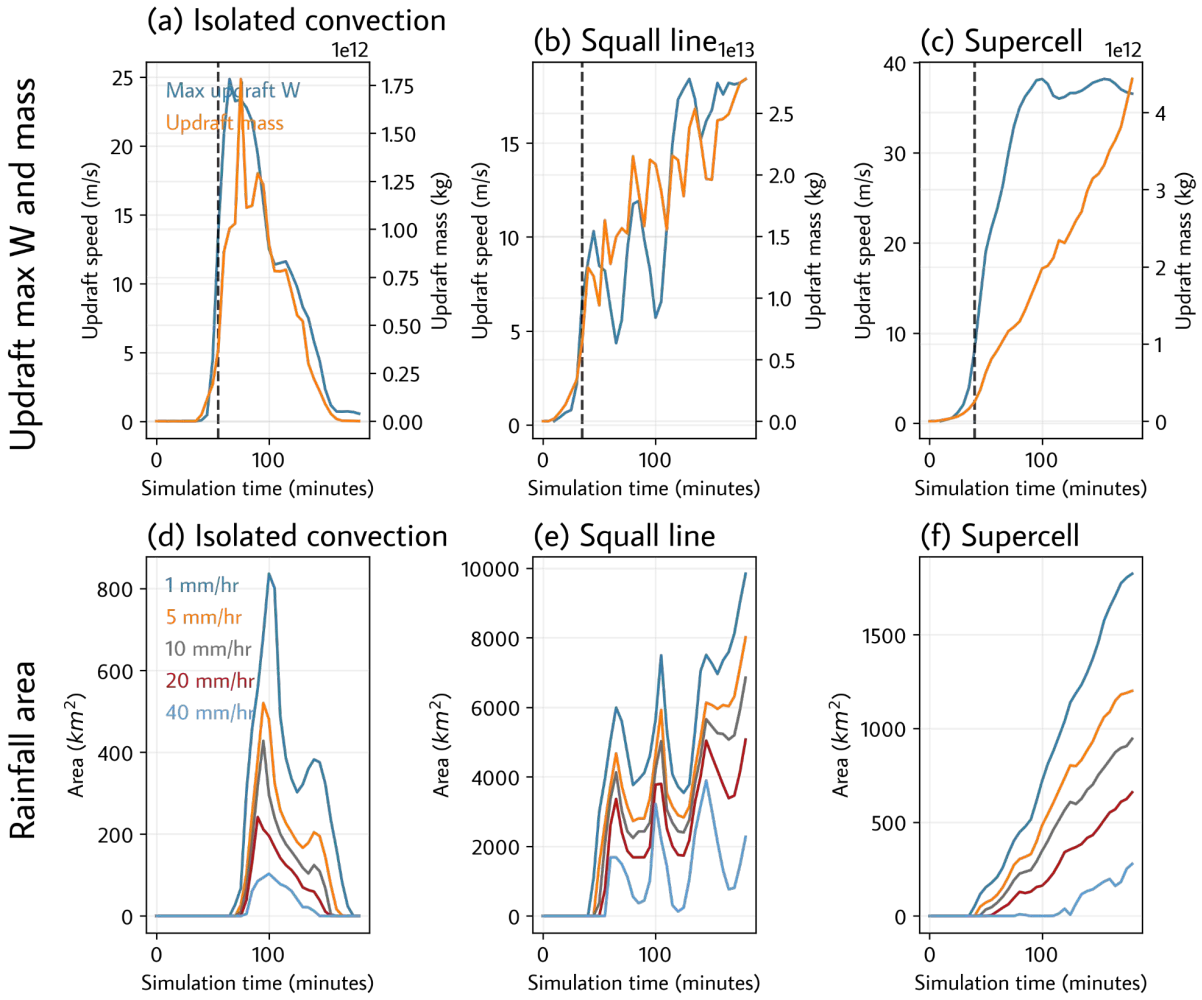

Figure 6.3 Storm-averaged measures of development for each storm. Panels (a-c) show the total updraft mass in gold and the maximum z=5km updraft speed (as defined in the methodology) in blue for each storm across time. The dashed vertical line indicates the time at which this updraft speed first exceeds W_{20max}, which is the time at which parcels are first initiated. Updraft speed values are on the left side of the y axis of each panel, and updraft mass values are on the right. Panels (d-f) show the total area of the domain in each simulation where the rainfall rate meets or exceeds each of the five rainfall thresholds for rain-sourced tracer emission, vs time.

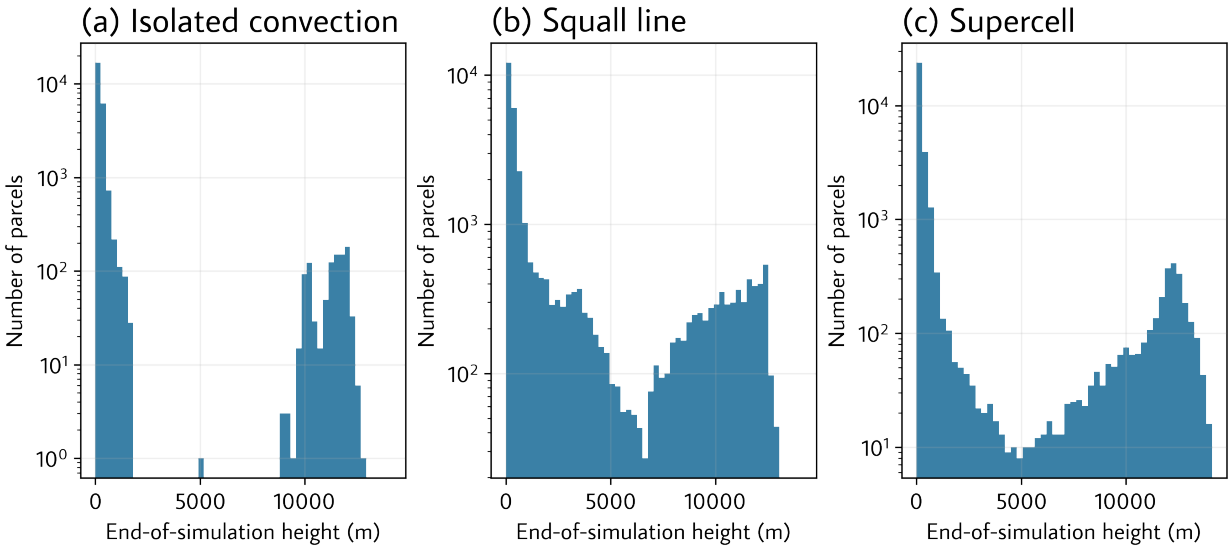

Figure 6.4 Distribution of heights of all parcels in each storm at t=180 minutes.

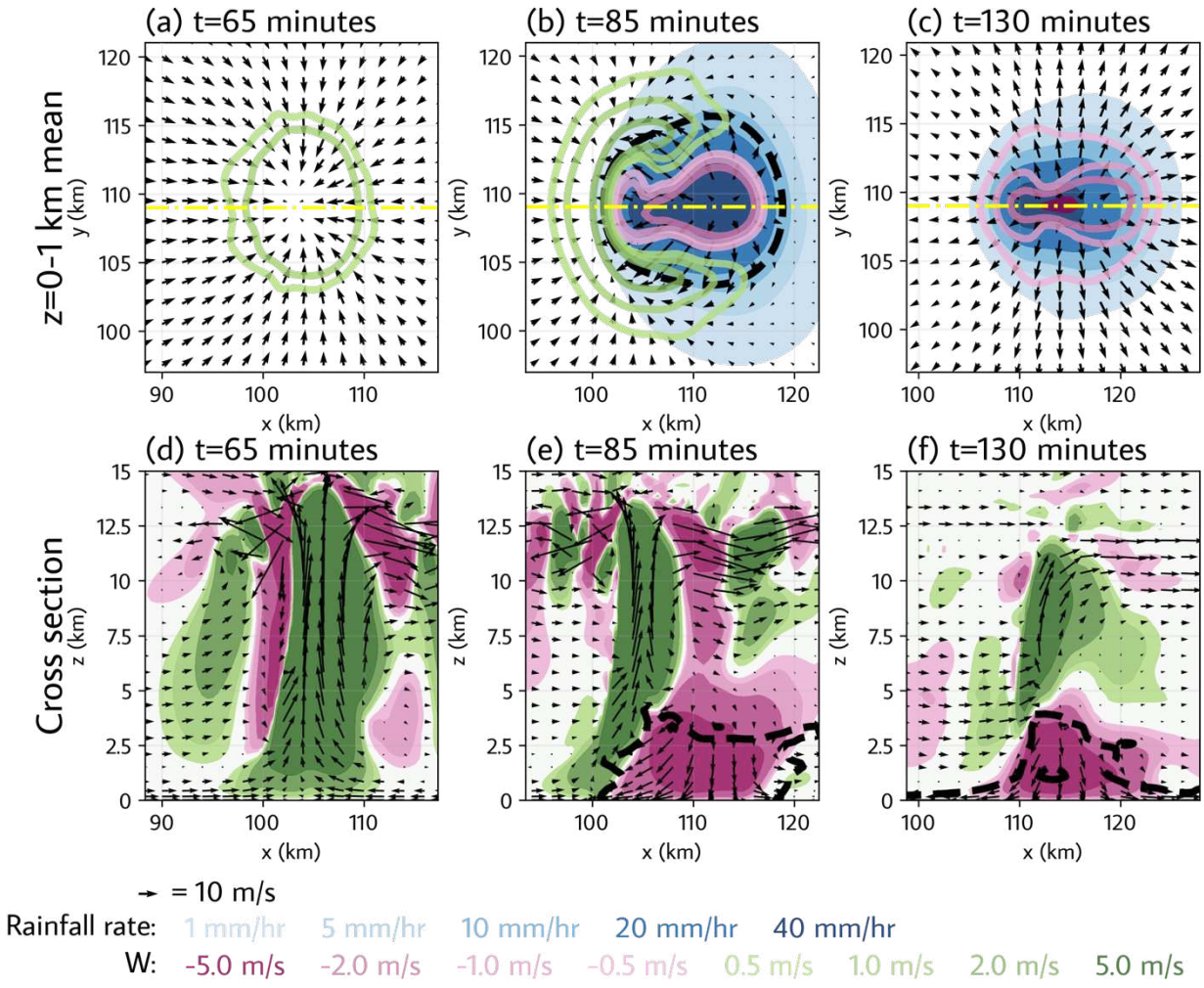

Figure 6.5 Simulated development of the isolated convective storm. Panels (a-c) show a plan view of the low-level storm features. The green and pink contours show the z=0-1 km mean vertical motion. The filled blue contours show the rain rate, with the contours corresponding to each of the five rainfall threshold values (i.e. ranging from 1 mm/hr in light blue to 40 mm/hr in dark blue). The arrows show the z=0-1 km mean horizontal winds. Panels (d-f) show a cross section through the dot-dashed yellow line in panels a-c. The filled contours show the vertical motion as in panels a-c. The arrows show the U and W winds. In all panels, the dashed black contour is the -0.04 m^2s^{-1} buoyancy contour, which we use to show the cold pool following Seigel and van den Heever (2012) and Tompkins et al. (2001).

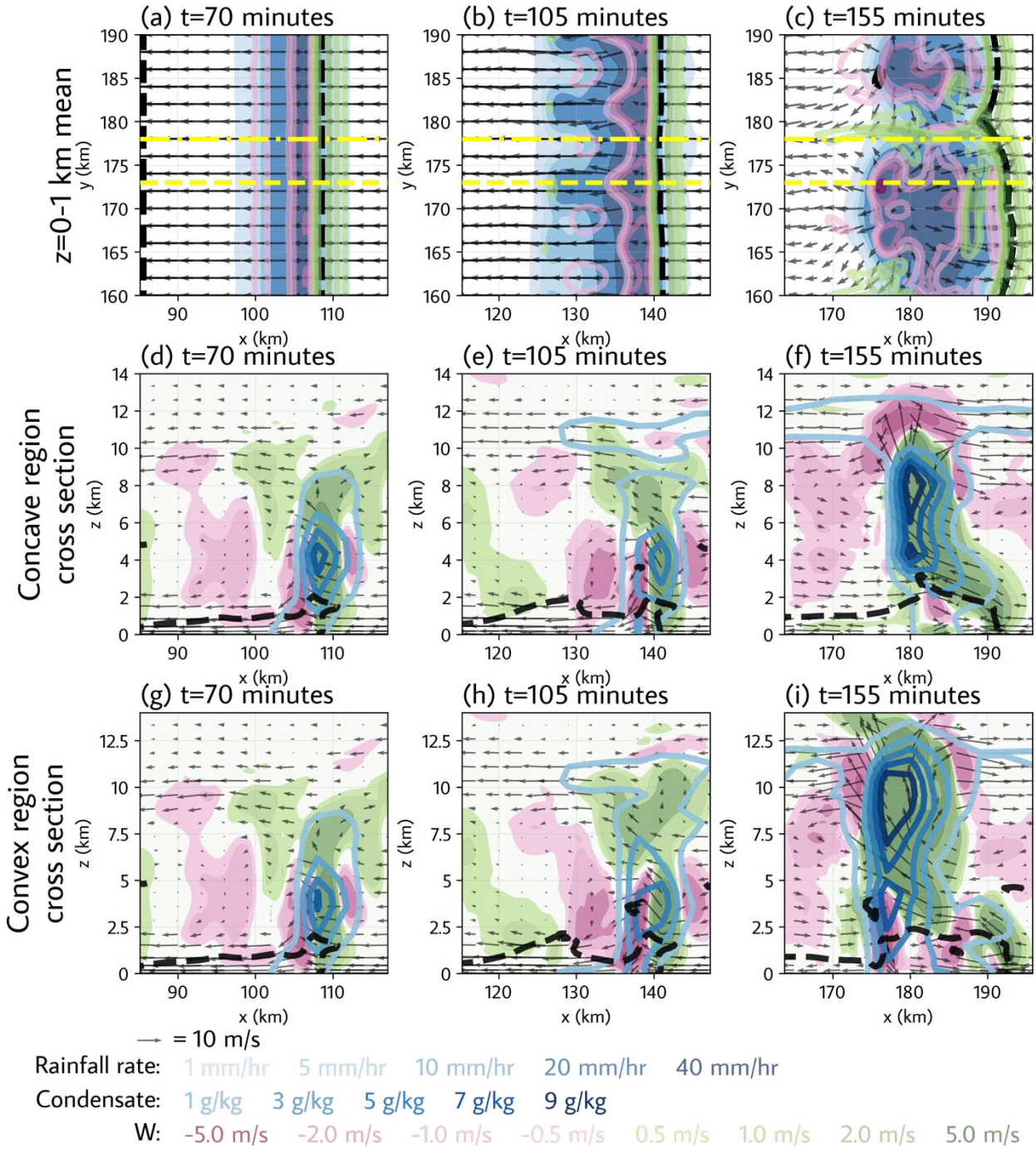

Figure 6.6 Simulated development of the squall line. Panels (a-c) are as in Figure 6.5 (a-c). Panels (d-f) show a cross section through one of the convex regions that develop along the line, the y value of which is indicated by the yellow dashed line (the more southerly of the two yellow lines) in panels (a-c). The filled green-to-pink contours and arrows are as in Figure 6.5 (d-f). The dashed purple contours show the condensate mixing ratio. Panels (g-i) are as in panels (d-f), but through the concave regions indicated by the dot-dashed yellow line (the more northerly of the two yellow lines) in panels (a-c). The cold pool is shown by the dashed black contour in all panels as in Figure 6.5.

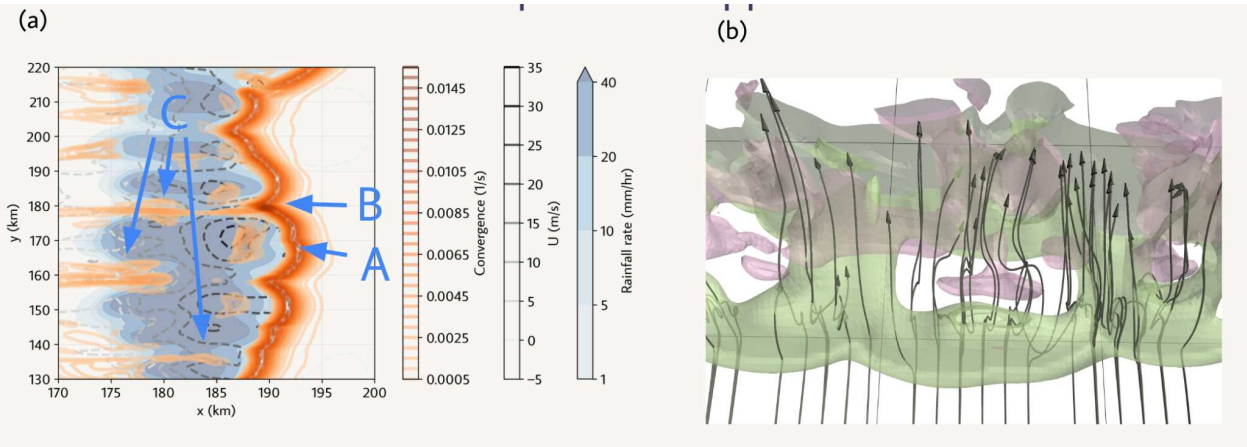

Figure 6.7 Significant along-line variation in the structure of the squall line influences the entrainment or lack thereof of parcels. Panel (a) shows a plan view of the squall line at t=155 minutes. The orange contours indicate the z=0-1 km mean horizontal convergence, the grey dashed contours indicate the 0-1km mean U velocity, and the filled blue contours indicate the rain rate, with the contour levels corresponding to the rainfall thresholds of the rain-sourced tracers. Panel (b) shows a 3D view of trajectories of parcels at the same time and location as panel (a). These trajectories are all eventually lofted to at least z=6km, which is our criterion for entrainment. The green contour is the 3 m/s updraft isosurface and the pink contour is the 3 m/s downdraft isosurface. Panel (b)'s view is rotated 90° relative to panel (a), i.e. the rear of the squall line is at the top of panel b. The lettered annotations in the figures are referenced in the text.

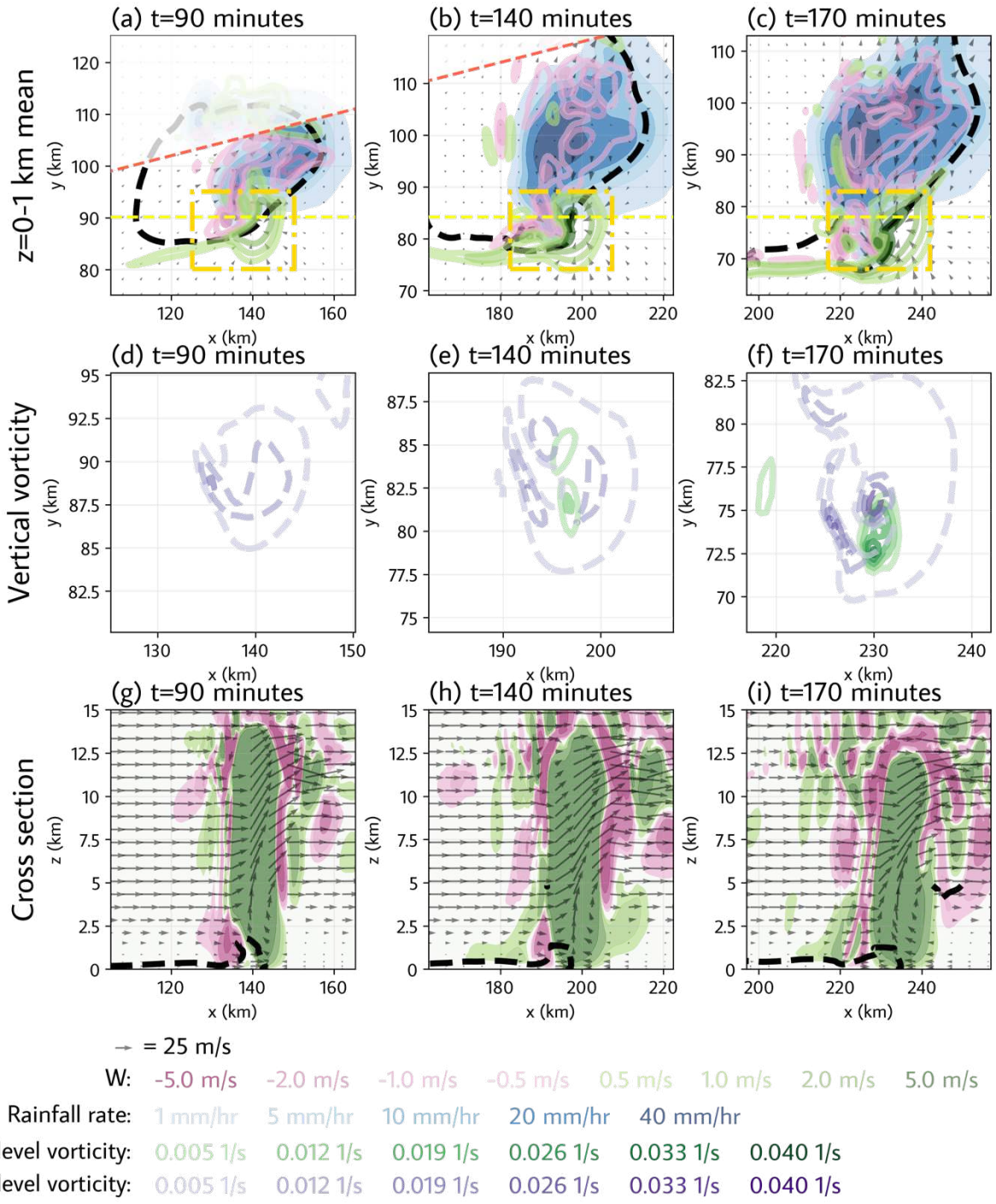

Figure 6.8 Simulated development of the supercell. Panels (a-c) are as in Figure 6.5 (a-c). The shaded-out region above the dashed red line in panels (a-b) indicates the portion of the domain that contains the left-mover and which was excluded from analysis. The dot-dashed orange rectangle indicates the region that is shown in panels (d-f). Panels (d-f) show the positive vertical vorticity near the updraft, with the green contours showing the z=0-1km mean positive vertical vorticity and the dashed purple contours showing the positive vertical vorticity at z=5 km. Panels

(g-i) show a cross section through the dashed yellow line in panels (a-c), as in Figure 6.5 (d-f). The cold pool is shown in panels (a-c) and (g-i) as in Figure 6.5.

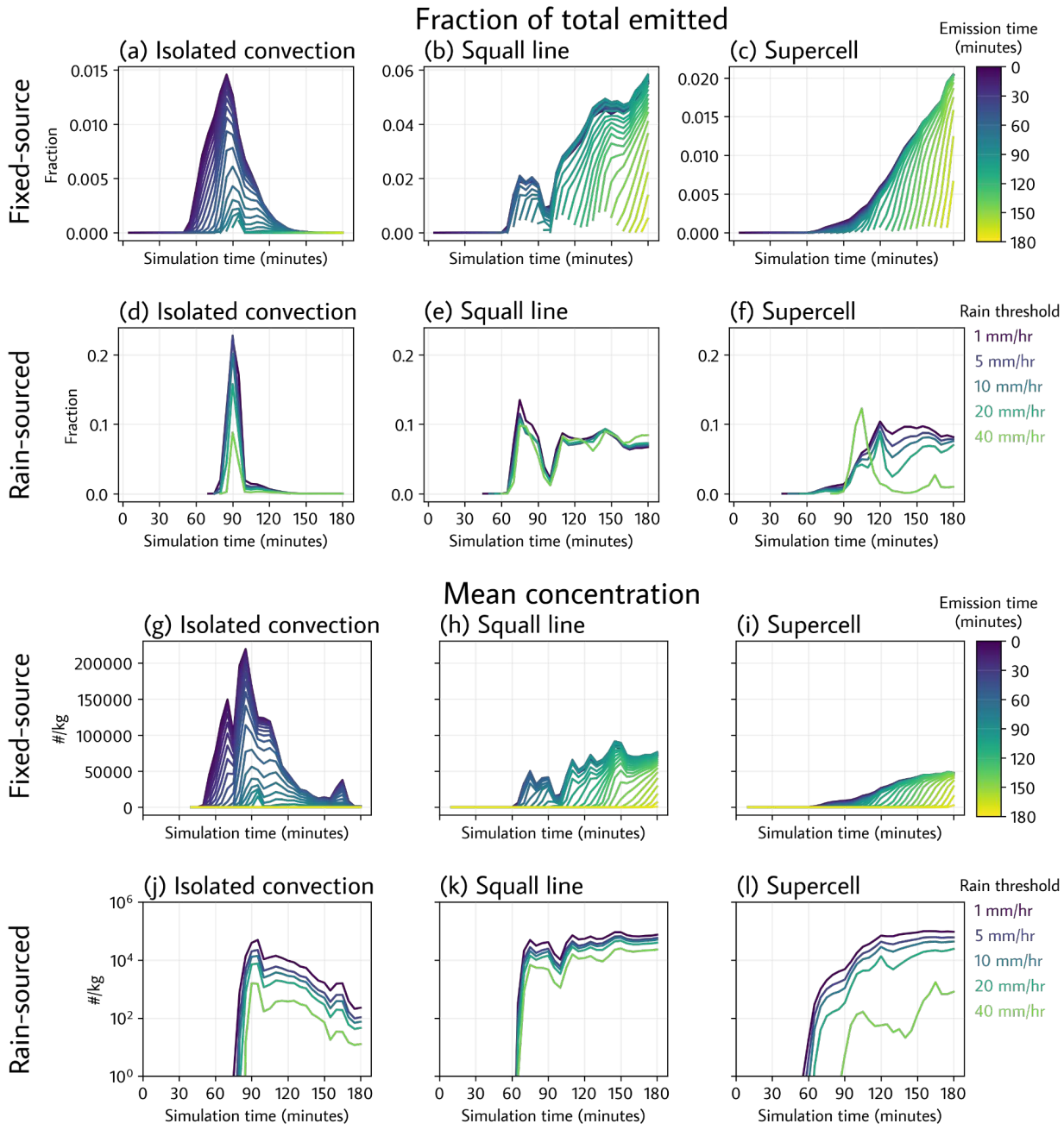

Figure 6.9 In-updraft tracer vs time, by tracer emission mechanism and species, and by storm morphology. Panels (a-c) shows the in-updraft concentrations of each fixed-source tracer species as a fraction of the total amount of that species that has been emitted at each point in time, with each color corresponding to a different tracer species (i.e. to a tracer emitted during a different period of time). Panels (d-f) show the same for each of the five rain-sourced tracer species, with each color corresponding to the different rain-sourced tracer species (and therefore different rain rate thresholds for emission). Panels (g-i) show the same as panels a-c but in mean number concentration terms rather than as a fraction of the total emitted. Panels (j-l) shows the same for the rain-sourced tracer species.

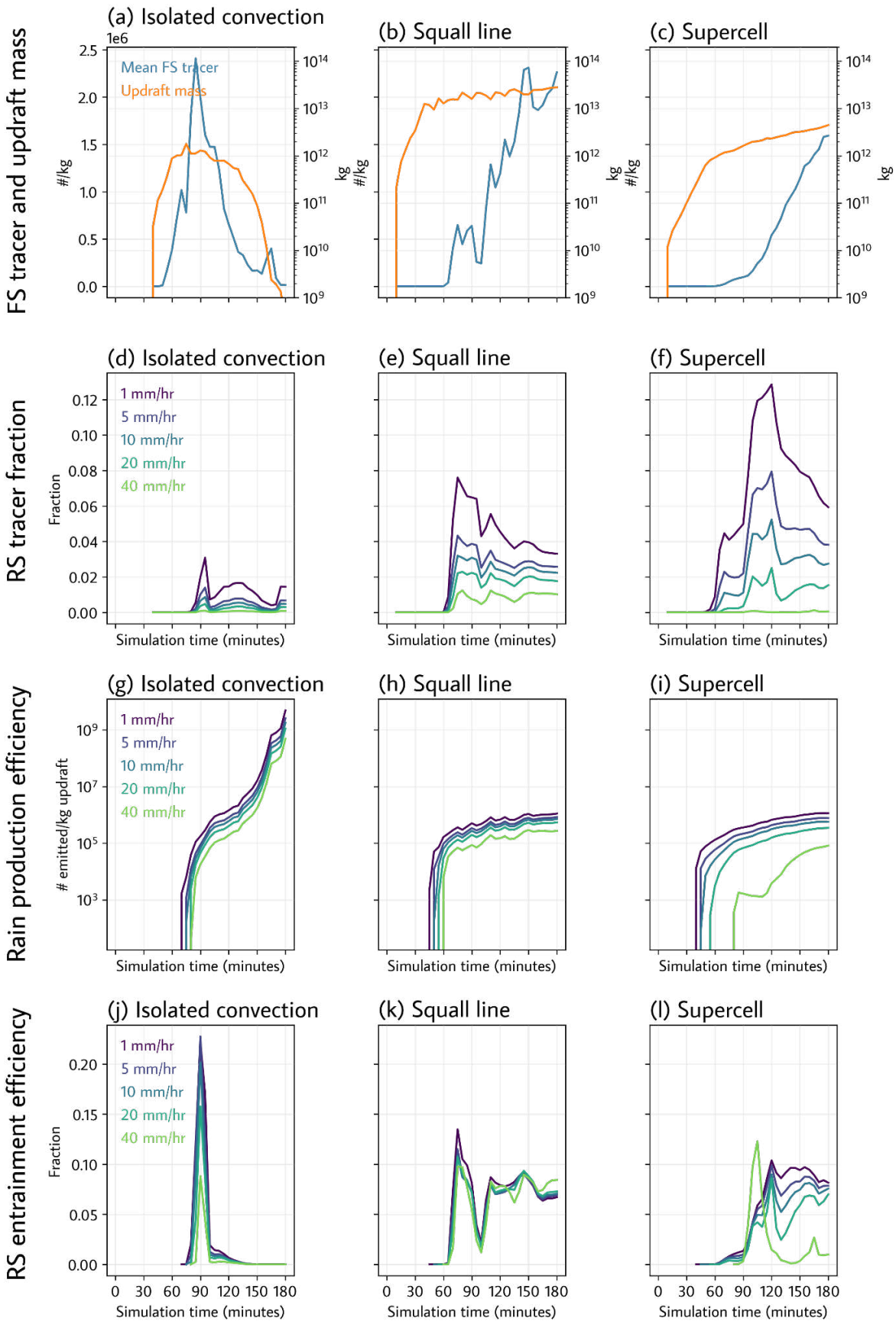
FS tracer and updraft mass
RS tracer fraction
Rain production efficiency
RS entrainment efficiency
(a) Isolated convection
(b) Squall line
(c) Supercell
(d) Isolated convection
(e) Squall line
(f) Supercell
(g) Isolated convection
(h) Squall line
(i) Supercell
(j) Isolated convection
(k) Squall line
(l) Supercell
Mean FS tracer
Updraft mass
1e6
#/kg
kg
Fraction
emitted/kg updraft
1 mm/hr
5 mm/hr
10 mm/hr
20 mm/hr
40 mm/hr
Simulation time (minutes)

Figure 6.10 Factors contributing to the mean in-updraft rain-sourced tracer mixing ratio as a function of time. Panels (a-c) show both the mean in-updraft fixed-source tracer mixing ratio and the total mass of the updraft; the total in-updraft fixed-source tracer is the product of these two quantities. Panels (d-f) depict the ratio of the total in-updraft rain-sourced tracer to the total in-updraft-fixed-source tracer, for each of the five rain-sourced tracers. Panels (g-i) show the ratio of the total emitted rain-sourced tracer to the mass of the updraft for each of the five rain-sourced tracers. Panels (j-l) show the entrained fraction of each of the five rain-sourced tracers, i.e. the ratio of the total in-updraft tracer to the total amount of that tracer emitted.

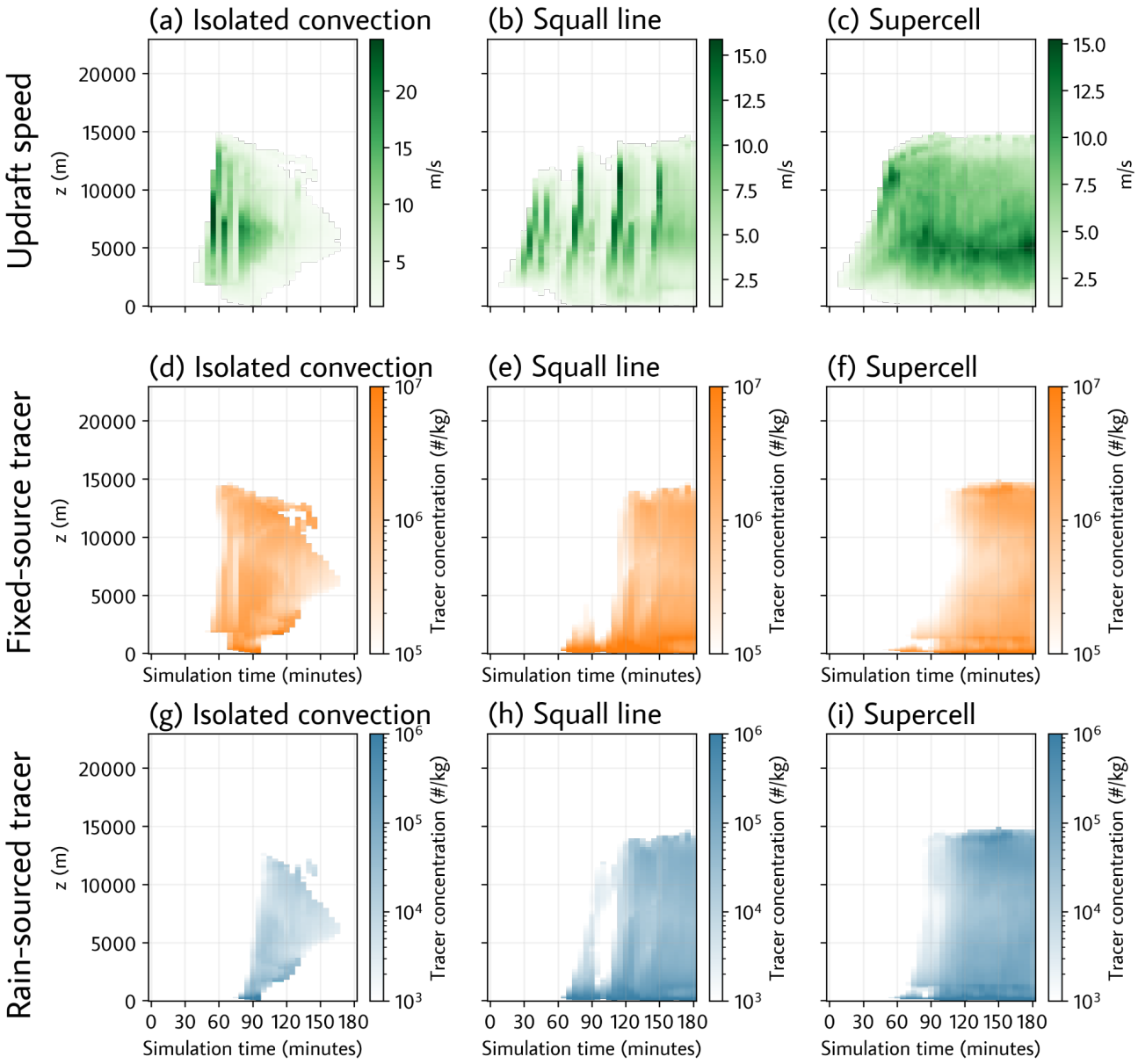

Figure 6.11 Mean in-updraft vertical and temporal distributions of updraft speed and tracer concentrations, by storm. Panels (a-c) shows mean updraft speed of in-updraft points at each vertical level and time. Panels (d-f) depict the same for the total mixing ratio of all fixed-source tracer species. Panels (g-i) shows the same for the rain-sourced tracer corresponding to the lowest rain threshold for emission (1 mm/hr).

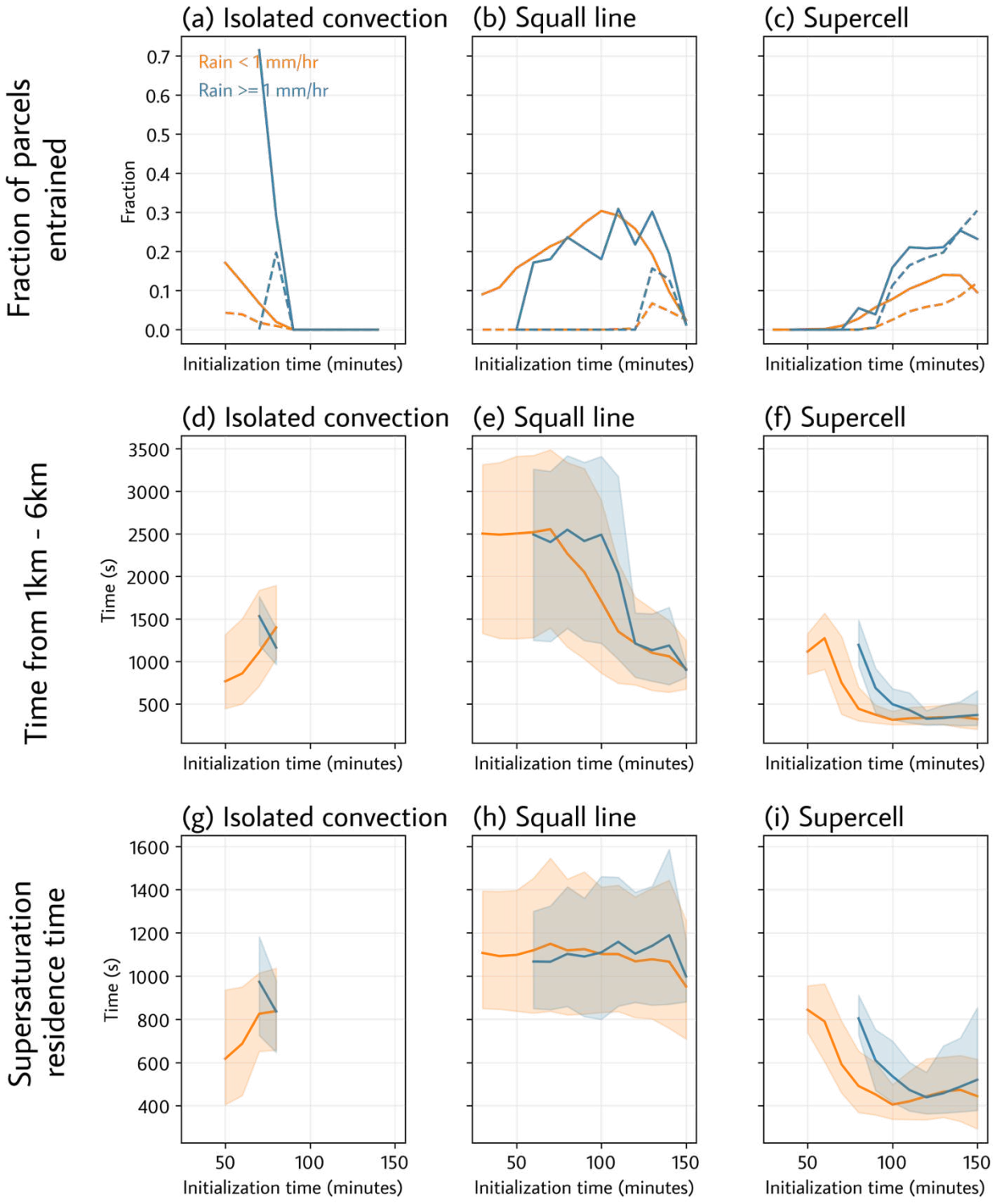

Figure 6.12 Statistics of parcel entrainment and supersaturation residence times. In all panels, the gold line corresponds to parcels not initialized in rain (< 1 mm/hr), and the blue line corresponds to parcels initialized in rainfall of >= 1 mm/hr. Panels (a-c) show the proportion of parcels entrained by each storm as a function of rain at initialization and initialization time. Panels (d-f)

show the length of time between entrained parcels first reaching z=1 km and first reaching z=6 km (i.e. reaching the height by which we define entrainment). The solid line is the mean and the shading covers the 10^{th} through 90^{th} percentiles. Panels (g-i) are as in panels (d-f) but depict the mean time spent by entrained parcels in supersaturated environments.

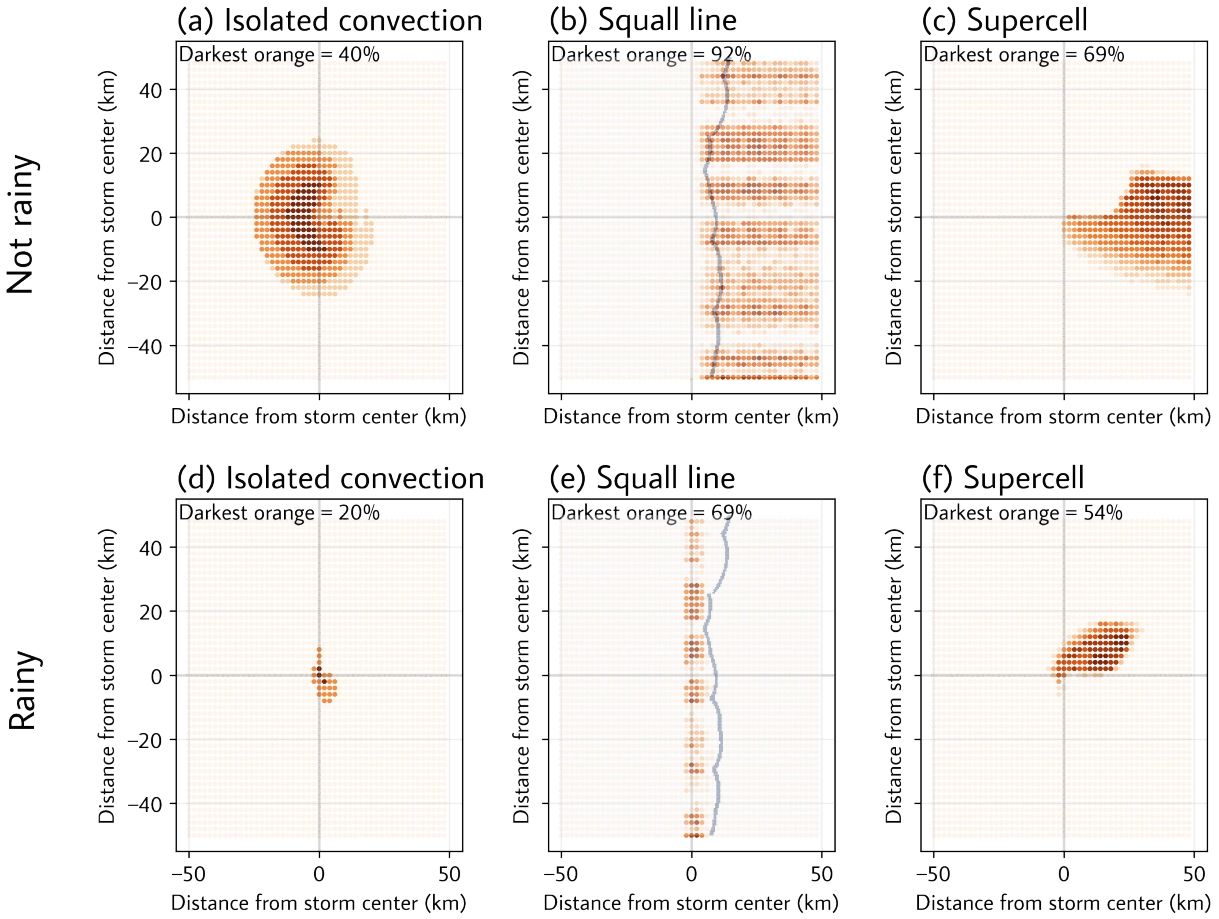

Figure 6.13 Composite of the initial positions of lofted parcels across all initialization times showing percentage entrainment. The centroid of the storm is indicated by the dashed lines that cross at (0, 0). The x and y axes show the storm-relative initialization location, and the color of each dot represents the fraction of parcels initialized at that storm-relative location that were entrained across all initialization times. As an example, the color of the dot one to the right of center gives the proportion of the parcels initialized 2 km to the right of the storm centroid (wherever that may have been in an absolute sense at their initialization time) that were entrained across all initialization times. Panels (a-c) show this only for parcels not initialized in rain, and panels (d-f) show this for parcels initialized in rain. Panels (b) and (e) also indicate the locations of concave and convex regions of the squall line to give a sense of how they align with higher/lower entrainment rates. The blue highlight covers the region where the z=0-1 km vertical velocity is at least 3 m/s at t=155 minutes, which is intended to indicate the position and shape of the gust front.

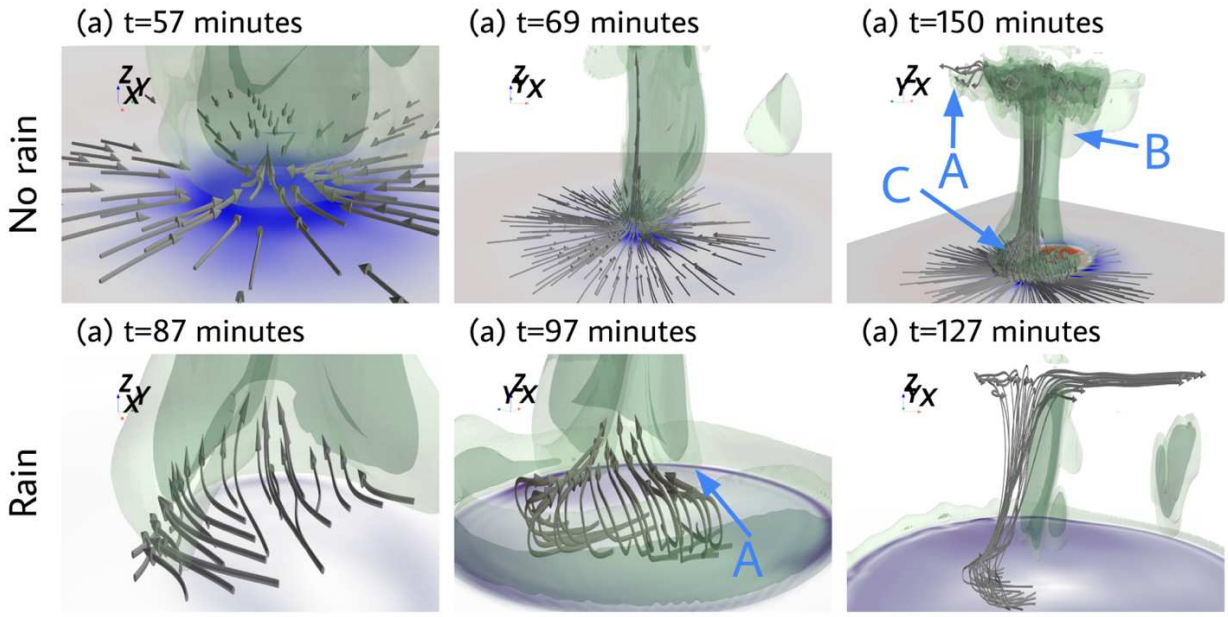

Figure 6.14 Non-rainy parcels are entrained into the isolated storm by convergence and direct uplift, and rainy parcels are entrained by the circulation in the edge of the cold pool and subsequent lifting into the updraft. Green contours are 2 m/s and 5 m/s updraft isosurfaces. The blue-to-red shading on the surface in panels a-c shows the z=0-1 km mean horizontal convergence (blue)/divergence (red), ranging from -0.005 s^{-1} to 0.005 s^{-1}. The purple shading in panels d-f shows the z= 0-1km mean magnitude of the horizontal vorticity (i.e. the norm of the x and y vorticity vectors added together) with darkest purple corresponding to a magnitude of 0.06 s^{-1}. The lettered annotations in the figures are referenced in the text.

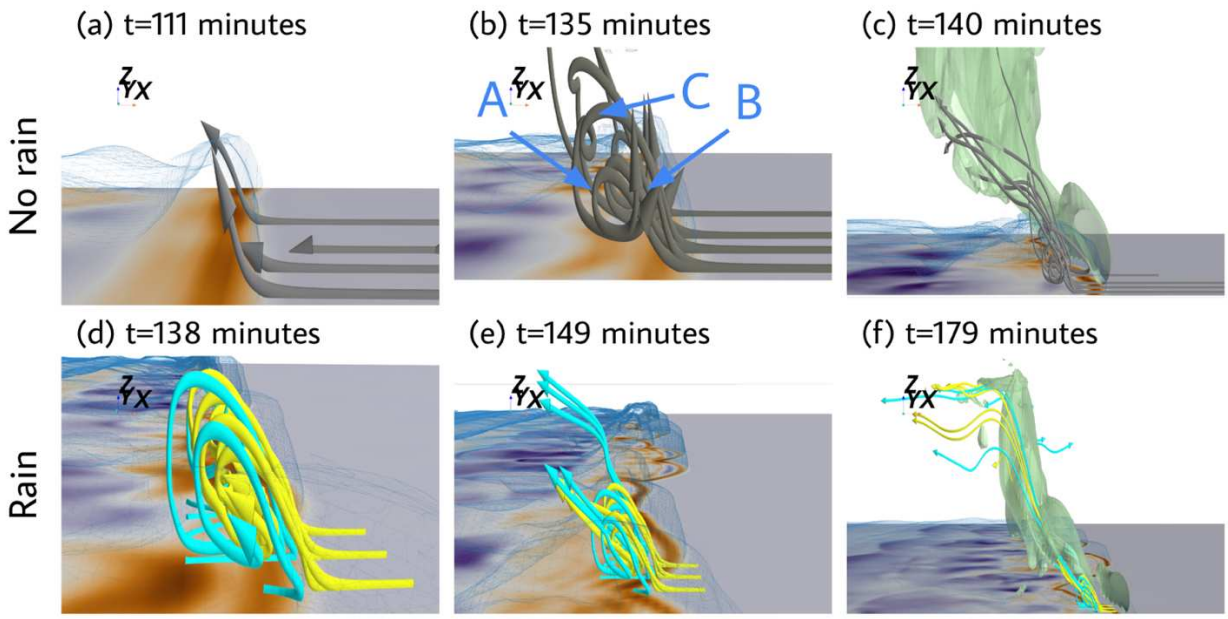

Figure 6.15 Non-rainy parcels are entrained into the squall line by lofting over the gust front, circulation in the horizontal vorticity in the head of the cold pool, and lifting by the upshear-tilted main updraft. Rainy parcels are entrained by the same mechanism if they originate in front of the cold pool, and by the same mechanism but without the need for the gust front lofting if they originate inside the cold pool. Green contours in panels (c) and (f) are the 3 m/s updraft isosurfaces. These contours are omitted in panels (a), (b), (d), and (e) to show the motion of the trajectories more clearly. The z=0-1km mean y vorticity is shown by the shading on the surface, with the darkest orange corresponding to a value of -0.03 s^{-1} and the darkest purple corresponding to 0.03 s^{-1}. In panels (d-f), the light blue trajectory arrows are those originating in rain inside of the cold pool, while the yellow arrows are those originating in rain ahead of the cold pool. The transparent blue wiremesh contour in all panels is the 2 K potential temperature deficit relative to the base state. Lettered annotations in the figures are referenced in the text.

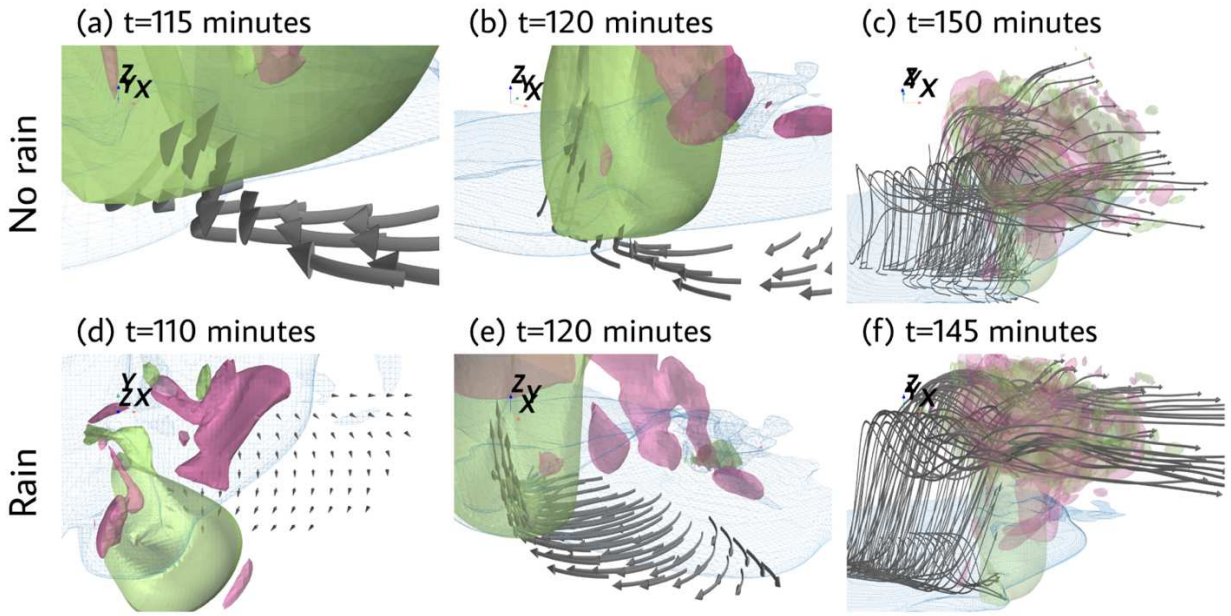

Figure 6.16 Non-rainy parcels are entrained into the supercell via gust-front lofting by the RFD's cold pool at the updraft, and rainy parcels are entrained both via this mechanism and by direct entrainment. Rainy parcels entrained via gust-front lofting originate in a narrow band of rain just ahead of the FFD's cold pool, and those entrained directly from within the cold pool originate in a narrow band of rain just inside the leading edge of the FFD's cold pool. The green and pink contours are the 5 m/s updraft and downdraft isosurfaces, respectively. Note that the transparency of these contours is varied between the panels, which is done for clarity and is not physically meaningfully. The transparent blue wiremesh contour in all panels is the 2 K potential temperature deficit relative to the base state.

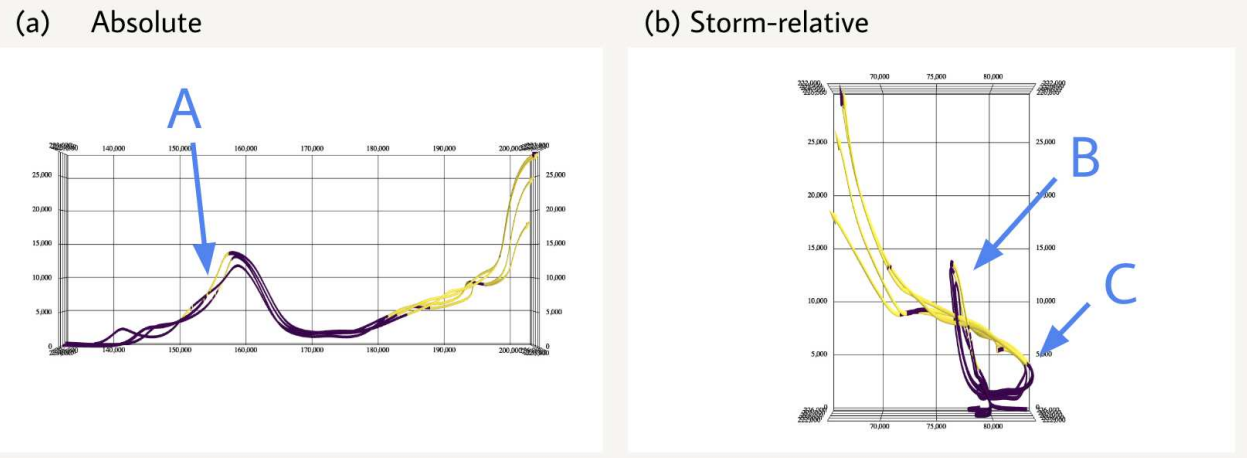

Figure 6.17 Some lofted squall-line trajectories spend more than 1800 s in supersaturated environments. The yellow regions of the trajectories indicate supersaturated environments. Panel (a) shows the unmodified trajectories, and panel (b) shows the storm-relative path of the trajectories. The orientation of these depictions is like that of a cross section, i.e. the y axis is into the page. Annotations are referenced in the text.

REFERENCES

Aitken, J., 1881: XII.—On Dust, Fogs, and Clouds. *Earth Environ. Sci. Trans. R. Soc. Edinb.*, **30**, 337–368, https://doi.org/10.1017/S0080456800029069.

Akila, M., H. Priyamvada, R. Ravikrishna, and S. S. Gunthe, 2018: Characterization of bacterial diversity and ice-nucleating ability during different monsoon seasons over a southern tropical Indian region. *Atmos. Environ.*, **191**, 387–394, https://doi.org/10.1016/j.atmosenv.2018.08.026.

Albrecht, B. A., 1989: Aerosols, Cloud Microphysics, and Fractional Cloudiness. *Science*, **245**, 1227–1230, https://doi.org/10.1126/science.245.4923.1227.

Andreae, M. O., D. Rosenfeld, P. Artaxo, A. A. Costa, G. P. Frank, K. M. Longo, and M. A. F. Silva-Dias, 2004: Smoking Rain Clouds over the Amazon. *Science*, https://doi.org/10.1126/science.1092779.

Ångström, A., 1929: On the Atmospheric Transmission of Sun Radiation and on Dust in the Air. Geografiska Annaler, 11, 156–166, https://doi.org/10.1080/20014422.1929.11880498.

Ariya, P. A., J. Sun, N. A. Eltouny, E. D. Hudson, C. T. Hayes, and G. Kos, 2009: Physical and chemical characterization of bioaerosols – Implications for nucleation processes. *Int. Rev. Phys. Chem.*, **28**, 1–32, https://doi.org/10.1080/01442350802597438.

Bluestein, H. B., and M. H. Jain, 1985: Formation of Mesoscale Lines of Pirecipitation: Severe Squall Lines in Oklahoma during the Spring. *J. Atmospheric Sci.*, **42**, 1711–1732, https://doi.org/10.1175/1520-0469(1985)042<1711:FOMLOP>2.0.CO;2.

Browning, K. A., 1964: Airflow and Precipitation Trajectories Within Severe Local Storms Which Travel to the Right of the Winds. Journal of the Atmospheric Sciences, 21, 634–639, https://doi.org/10.1175/1520-0469(1964)021<0634:AAPTWS>2.0.CO;2.

Browning, K. A., 1977: The Structure and Mechanisms of Hailstorms. *Hail: A Review of Hail Science and Hail Suppression*, G.B. Foote and C.A. Knight, Eds., American Meteorological Society, 1–47.

Bryan, G. H., and H. Morrison, 2012: Sensitivity of a Simulated Squall Line to Horizontal Resolution and Parameterization of Microphysics. *Mon. Weather Rev.*, **140**, 202–225, https://doi.org/10.1175/MWR-D-11-00046.1.

Byers, H. R., and R. R. Braham, 1949: *The Thunderstorm: Report of the Thunderstorm Project*. U.S. Government Printing Office, 308 pp.

Charlson, R. J., S. E. Schwartz, J. M. Hales, R. D. Cess, J. A. Coakley, J. E. Hansen, and D. J. Hofmann, 1992: Climate Forcing by Anthropogenic Aerosols. *Science*, **255**, 423–430, https://doi.org/10.1126/science.255.5043.423.

Coakley, J. A., R. D. Cess, and F. B. Yurevich, 1983: The Effect of Tropospheric Aerosols on the Earth's Radiation Budget: A Parameterization for Climate Models. Journal of the Atmospheric Sciences, 40, 116–138, https://doi.org/10.1175/1520-0469(1983)040<0116:TEOTAO>2.0.CO;2.

Coffer, B. E., M. D. Parker, J. M. Peters, and A. R. Wade, 2023: Supercell Low-Level Mesocyclones: Origins of Inflow and Vorticity. https://doi.org/10.1175/MWR-D-22-0269.1.

Corr, C. A., and Coauthors, 2016: Observational evidence for the convective transport of dust over the Central United States. *J. Geophys. Res. Atmospheres*, **121**, 1306–1319,

https://doi.org/10.1002/2015JD023789.
Cotton, W. R., and Coauthors, 2003: RAMS 2001: Current status and future directions. *Meteorol. Atmospheric Phys.*, **82**, 5–29, https://doi.org/10.1007/s00703-001-0584-9.
Cotton, W. R., G. H. Bryan, and S. C. van den Heever, 2010: Storm and Cloud Dynamics. Elsevier Inc., 809 pp.
Creamean, J. M., and Coauthors, 2013: Dust and Biological Aerosols from the Sahara and Asia Influence Precipitation in the Western U.S. *Science*, **339**, 1572–1578, https://doi.org/10.1126/science.1227279.
——, R. M. Kirpes, K. A. Pratt, N. J. Spada, M. Maahn, G. de Boer, R. C. Schnell, and S. China, 2018: Marine and terrestrial influences on ice nucleating particles during continuous springtime measurements in an Arctic oilfield location. *Atmospheric Chem. Phys.*, **18**, 18023–18042, https://doi.org/10.5194/acp-18-18023-2018.
Creamean, J. M., and Coauthors, 2019: Ice Nucleating Particles Carried From Below a Phytoplankton Bloom to the Arctic Atmosphere. *Geophys. Res. Lett.*, **46**, 8572–8581, https://doi.org/10.1029/2019GL083039.
Dahl, J. M. L., M. D. Parker, and L. J. Wicker, 2012: Uncertainties in Trajectory Calculations within Near-Surface Mesocyclones of Simulated Supercells. *Mon. Weather Rev.*, **140**, 2959–2966, https://doi.org/10.1175/MWR-D-12-00131.1.
D'Amato, G., and Coauthors, 2016: Thunderstorm-related asthma: what happens and why. *Clin. Exp. Allergy*, **46**, 390–396, https://doi.org/10.1111/cea.12709.
Davies-Jones, R., 1984: Streamwise Vorticity: The Origin of Updraft Rotation in Supercell Storms. Journal of the Atmospheric Sciences, 41, 2991–3006, https://doi.org/10.1175/1520-0469(1984)041<2991:SVTOOU>2.0.CO;2.
——, 2015: A review of supercell and tornado dynamics. *Atmospheric Res.*, **158–159**, 274–291, https://doi.org/10.1016/j.atmosres.2014.04.007.
DeMott, P. J., D. C. Rogers, and S. M. Kreidenweis, 1997: The susceptibility of ice formation in upper tropospheric clouds to insoluble aerosol components. *J. Geophys. Res. Atmospheres*, **102**, 19575–19584, https://doi.org/10.1029/97JD01138.
——, ——, ——, Y. Chen, C. H. Twohy, D. Baumgardner, A. J. Heymsfield, and K. R. Chan, 1998: The role of heterogeneous freezing nucleation in upper tropospheric clouds: Inferences from SUCCESS. *Geophys. Res. Lett.*, **25**, 1387–1390, https://doi.org/10.1029/97GL03779.
DeMott, P. J., D. J. Cziczo, A. J. Prenni, D. M. Murphy, S. M. Kreidenweis, D. S. Thomson, R. Borys, and D. C. Rogers, 2003a: Measurements of the concentration and composition of nuclei for cirrus formation. *Proc. Natl. Acad. Sci.*, **100**, 14655–14660, https://doi.org/10.1073/pnas.2532677100.
DeMott, P. J., K. Sassen, M. R. Poellot, D. Baumgardner, D. C. Rogers, S. D. Brooks, A. J. Prenni, and S. M. Kreidenweis, 2003b: African dust aerosols as atmospheric ice nuclei. *Geophys. Res. Lett.*, **30**, 2003GL017410, https://doi.org/10.1029/2003GL017410.
DeMott, P. J., and Coauthors, 2010: Predicting global atmospheric ice nuclei distributions and their impacts on climate. *Proc. Natl. Acad. Sci.*, **107**, 11217–11222, https://doi.org/10.1073/pnas.0910818107.
DeMott, P. J., and Coauthors, 2011: Resurgence in Ice Nuclei Measurement Research. Bulletin of the American Meteorological Society, 92, 1623–1635, https://doi.org/10.1175/2011BAMS3119.1.
——, and Coauthors, 2016: Sea spray aerosol as a unique source of ice nucleating particles.

Proc. Natl. Acad. Sci., **113**, 5797–5803, https://doi.org/10.1073/pnas.1514034112.
Després, V. R., and Coauthors, 2012: Primary biological aerosol particles in the atmosphere: a review. *Tellus B Chem. Phys. Meteorol.*, **64**, https://doi.org/10.3402/tellusb.v64i0.15598.
Diehl, K., S. Matthias-Maser, R. Jaenicke, and S. K. Mitra, 2002: The ice nucleating ability of pollen:: Part II. Laboratory studies in immersion and contact freezing modes. *Atmospheric Res.*, **61**, 125–133, https://doi.org/10.1016/S0169-8095(01)00132-6.
Engström, A., A. M. L. Ekman, R. Krejci, J. Ström, M. de Reus, and C. Wang, 2008: Observational and modelling evidence of tropical deep convective clouds as a source of mid-tropospheric accumulation mode aerosols. *Geophys. Res. Lett.*, **35**, https://doi.org/10.1029/2008GL035817.
Fan, J., R. Zhang, G. Li, and W. Tao, 2007: Effects of aerosols and relative humidity on cumulus clouds. *J. Geophys. Res. Atmospheres*, **112**, 2006JD008136, https://doi.org/10.1029/2006JD008136.
——, and Coauthors, 2009: Dominant role by vertical wind shear in regulating aerosol effects on deep convective clouds. *J. Geophys. Res. Atmospheres*, **114**, https://doi.org/10.1029/2009JD012352.
——, L. R. Leung, D. Rosenfeld, Q. Chen, Z. Li, J. Zhang, and H. Yan, 2013: Microphysical effects determine macrophysical response for aerosol impacts on deep convective clouds. *Proc. Natl. Acad. Sci.*, **110**, E4581–E4590, https://doi.org/10.1073/pnas.1316830110.
——, and Coauthors, 2018: Substantial convection and precipitation enhancements by ultrafine aerosol particles. *Science*, **359**, 411–418, https://doi.org/10.1126/science.aan8461.
Fierro, A. O., J. Simpson, M. A. LeMone, J. M. Straka, and B. F. Smull, 2009: On How Hot Towers Fuel the Hadley Cell: An Observational and Modeling Study of Line-Organized Convection in the Equatorial Trough from TOGA COARE. Journal of the Atmospheric Sciences, 66, 2730–2746, https://doi.org/10.1175/2009JAS3017.1.
Findeisen, W., 1938: Colloidal meteorological processes in the formation of precipitation. *Meteorol. Z.*, **24**, 443–454, https://doi.org/10.1127/metz/2015/0675.
Flowers, E. C., R. A. McCormick, and K. R. Kurfis, 1969: Atmospheric Turbidity over the United States, 1961–1966. Journal of Applied Meteorology and Climatology, 8, 955–962, https://doi.org/10.1175/1520-0450(1969)008<0955:ATOTUS>2.0.CO;2.
Foote, G. B., and J. C. Fankhauser, 1973: Airflow and Moisture Budget Beneath a Northeast Colorado Hailstorm. *Journal of Applied Meteorology and Climatology*, **12**, 1330–1353, https://doi.org/10.1175/1520-0450(1973)012<1330:AAMBBA>2.0.CO;2.
Franc, Gary D., and Paul J. DeMott. "Cloud Activation Characteristics of Airborne Erwinia Carotovora Cells." *Journal of Applied Meteorology and Climatology* 37, no. 10 (October 1, 1998): 1293–1300. https://doi.org/10.1175/1520-0450(1998)037<1293:CACOAE>2.0.CO;2.
Fröhlich-Nowoisky, J., T. C. J. Hill, B. G. Pummer, P. Yordanova, G. D. Franc, and U. Pöschl, 2015: Ice nucleation activity in the widespread soil fungus *Mortierella alpina*. *Biogeosciences*, **12**, 1057–1071, https://doi.org/10.5194/bg-12-1057-2015.
Froyd, K. D., D. M. Murphy, T. J. Sanford, D. S. Thomson, J. C. Wilson, L. Pfister, and L. Lait, 2009: Aerosol composition of the tropical upper troposphere. *Atmospheric Chem. Phys.*, **9**, 4363–4385, https://doi.org/10.5194/acp-9-4363-2009.
Fujita, Tetsuya, and Hector Grandoso. "Split of a Thunderstorm into Anticyclonic and Cyclonic Storms and Their Motion as Determined from Numerical Model Experiments." *Journal of the Atmospheric Sciences* 25, no. 3 (May 1, 1968): 416–39.

https://doi.org/10.1175/1520-0469(1968)025<0416:SOATIA>2.0.CO;2.
Gowan, T. M., 2018: Using Idealized Large-Eddy Simulations to Understand the Impact of Downstream Terrain on Lake-Effect Snowfall. 18th Conference on Mountain Meteorology, AMS https://ams.confex.com/ams/18Mountain/webprogram/Paper346052.html (Accessed October 25, 2024).
Grabowski, Wojciech W. "Untangling Microphysical Impacts on Deep Convection Applying a Novel Modeling Methodology." *Journal of the Atmospheric Sciences* 72, no. 6 (June 1, 2015): 2446–64. https://doi.org/10.1175/JAS-D-14-0307.1.
Grabowski, Wojciech W. "Can the Impact of Aerosols on Deep Convection Be Isolated from Meteorological Effects in Atmospheric Observations?" *Journal of the Atmospheric Sciences* 72, no. 10 (October 1, 2018): 3347–63. https://doi.org/10.1175/JAS-D-18-0105.1.
Grant, L. D., and S. C. van den Heever, 2014: Microphysical and Dynamical Characteristics of Low-Precipitation and Classic Supercells. *J. Atmospheric Sci.*, **71**, 2604–2624, https://doi.org/10.1175/JAS-D-13-0261.1.
Grant, Leah D., and Susan C. van den Heever. "Cold Pool and Precipitation Responses to Aerosol Loading: Modulation by Dry Layers." *Journal of the Atmospheric Sciences* 72, no. 4 (April 1, 2015): 1398–1408. https://doi.org/10.1175/JAS-D-14-0260.1.
Grell, G. A., S. E. Peckham, R. Schmitz, S. A. McKeen, G. Frost, W. C. Skamarock, and B. Eder, 2005: Fully coupled "online" chemistry within the WRF model. *Atmos. Environ.*, **39**, 6957–6975, https://doi.org/10.1016/j.atmosenv.2005.04.027.
Hallett, J., and S. C. Mossop, 1974: Production of secondary ice particles during the riming process. *Nature*, **249**, 26–28, https://doi.org/10.1038/249026a0.
van den Heever, S. C., G. G. Carrió, W. R. Cotton, P. J. DeMott, and A. J. Prenni, 2006: Impacts of Nucleating Aerosol on Florida Storms. Part I: Mesoscale Simulations. *Journal of the Atmospheric Sciences*, **63**, 1752–1775, https://doi.org/10.1175/JAS3713.1.
van den Heever, S. C., G. L. Stephens, and N. B. Wood, 2011: Aerosol Indirect Effects on Tropical Convection Characteristics under Conditions of Radiative–Convective Equilibrium. *Journal of the Atmospheric Sciences*, **68**, 699–718, https://doi.org/10.1175/2010JAS3603.1.
van den Heever, S. C., S. M. Saleeby, L. D. Grant, A. L. Igel, and S. W. Freeman, 2022: RAMS - the Regional Atmospheric Modeling System. https://doi.org/10.5281/zenodo.6869798.
Heo, K. J., H. B. Kim, and B. U. Lee, 2014: Concentration of environmental fungal and bacterial bioaerosols during the monsoon season. *J. Aerosol Sci.*, **77**, 31–37, https://doi.org/10.1016/j.jaerosci.2014.07.001.
Herbener, S. R., S. M. Saleeby, S. C. van den Heever, and C. H. Twohy, 2016: Tropical storm redistribution of Saharan dust to the upper troposphere and ocean surface. *Geophys. Res. Lett.*, **43**, 10,463-10,471, https://doi.org/10.1002/2016GL070262.
Hill, G. E., 1974: Factors Controlling the Size and Spacing of Cumulus Clouds as Revealed by Numerical Experiments. *Journal of the Atmospheric Sciences*, **31**, 646–673, https://doi.org/10.1175/1520-0469(1974)031<0646:FCTSAS>2.0.CO;2.
Hoffmann, F., S. Raasch, and Y. Noh, 2015: Entrainment of aerosols and their activation in a shallow cumulus cloud studied with a coupled LCM–LES approach. *Atmospheric Res.*, **156**, 43–57, https://doi.org/10.1016/j.atmosres.2014.12.008.
Hoose, C., and O. Möhler, 2012: Heterogeneous ice nucleation on atmospheric aerosols: a

review of results from laboratory experiments. *Atmospheric Chem. Phys.*, **12**, 9817–9854, https://doi.org/10.5194/acp-12-9817-2012.
Hoose, C., J. E. Kristjánsson, and S. M. Burrows, 2010: How important is biological ice nucleation in clouds on a global scale? *Environ. Res. Lett.*, **5**, 024009, https://doi.org/10.1088/1748-9326/5/2/024009.
Huffman, J. A., and Coauthors, 2013: High concentrations of biological aerosol particles and ice nuclei during and after rain. *Atmospheric Chem. Phys.*, **13**, 6151–6164, https://doi.org/10.5194/acp-13-6151-2013.
Hughes, D. D., C. B. A. Mampage, L. M. Jones, Z. Liu, and E. A. Stone, 2020: Characterization of Atmospheric Pollen Fragments during Springtime Thunderstorms. *Environ. Sci. Technol. Lett.*, **7**, 409–414, https://doi.org/10.1021/acs.estlett.0c00213.
Igel, A. L., and S. C. Van Den Heever, 2021: Invigoration or Enervation of Convective Clouds by Aerosols? *Geophys. Res. Lett.*, **48**, e2021GL093804, https://doi.org/10.1029/2021GL093804.
Isono, K., and T. Tanaka, 1966: Sudden Increase of Ice Nucleus Concentration Associated with Thunderstorm. *J. Meteorol. Soc. Jpn. Ser II*, **44**, 255–259, https://doi.org/10.2151/jmsj1965.44.5_255.
Jaenicke, R., 2005: Abundance of Cellular Material and Proteins in the Atmosphere. *Science*, **308**, 73–73, https://doi.org/10.1126/science.1106335.
Jensen, M. P., and Coauthors, 2023: *Tracking Aerosol Convection Interactions Experiment (TRACER) Field Campaign Report*. Oak Ridge National Laboratory (ORNL), Oak Ridge, TN (United States). Atmospheric Radiation Measurement (ARM) Data Center,. https://doi.org/10.2172/2202672
Joly, M., P. Amato, L. Deguillaume, M. Monier, C. Hoose, and A.-M. Delort, 2014: Quantification of ice nuclei active at near 0 °C temperatures in low-altitude clouds at the Puy de Dôme atmospheric station. *Atmospheric Chem. Phys.*, **14**, 8185–8195, https://doi.org/10.5194/acp-14-8185-2014.
Jones, A. M., and R. M. Harrison, 2004: The effects of meteorological factors on atmospheric bioaerosol concentrations—a review. *Sci. Total Environ.*, **326**, 151–180, https://doi.org/10.1016/j.scitotenv.2003.11.021.
Jorgensen, D. P., M. A. LeMone, and S. B. Trier, 1997: Structure and Evolution of the 22 February 1993 TOGA COARE Squall Line: Aircraft Observations of Precipitation, Circulation, and Surface Energy Fluxes. *Journal of the Atmospheric Sciences*, **54**, 1961–1985, https://doi.org/10.1175/1520-0469(1997)054<1961:SAEOTF>2.0.CO;2.
Joung, Y. S., Z. Ge, and C. R. Buie, 2017: Bioaerosol generation by raindrops on soil. *Nat. Commun.*, **8**, 14668, https://doi.org/10.1038/ncomms14668.
Kanji, Z. A., L. A. Ladino, H. Wex, Y. Boose, M. Burkert-Kohn, D. J. Cziczo, and M. Krämer, 2017: Overview of Ice Nucleating Particles. *Meteorol. Monogr.*, **58**, 1.1-1.33, https://doi.org/10.1175/AMSMONOGRAPHS-D-16-0006.1.
Khain, A., and A. Pokrovsky, 2004: Simulation of Effects of Atmospheric Aerosols on Deep Turbulent Convective Clouds Using a Spectral Microphysics Mixed-Phase Cumulus Cloud Model. Part II: Sensitivity Study. *Journal of the Atmospheric Sciences*, **61**, 2983–3001, https://doi.org/10.1175/JAS-3281.1.
Khain, A., D. Rosenfeld, and A. Pokrovsky, 2005: Aerosol impact on the dynamics and microphysics of deep convective clouds. *Q. J. R. Meteorol. Soc.*, **131**, 2639–2663, https://doi.org/10.1256/qj.04.62.

Khain, A. P., N. BenMoshe, and A. Pokrovsky, 2008: Factors Determining the Impact of Aerosols on Surface Precipitation from Clouds: An Attempt at Classification. *Journal of the Atmospheric Sciences*, **65**, 1721–1748, https://doi.org/10.1175/2007JAS2515.1.

Kingsmill, D. E., and R. M. Wakimoto, 1991: Kinematic, Dynamic, and Thermodynamic Analysis of a Weakly Sheared Severe Thunderstorm over Northern Alabama. *Monthly Weather Review*, **119**, 262–297, https://doi.org/10.1175/1520-0493(1991)119<0262:KDATAO>2.0.CO;2.

Koehler, K. A., S. M. Kreidenweis, P. J. DeMott, M. D. Petters, A. J. Prenni, and O. Möhler, 2010: Laboratory investigations of the impact of mineral dust aerosol on cold cloud formation. *Atmospheric Chem. Phys.*, **10**, 11955–11968, https://doi.org/10.5194/acp-10-11955-2010.

Koenig, L. R., 1963: The Glaciating Behavior of Small Cumulonimbus Clouds. *Journal of the Atmospheric Sciences*, **20**, 29–47, https://doi.org/10.1175/1520-0469(1963)020<0029:TGBOSC>2.0.CO;2.

Köhler, H., 1936: The nucleus in and the growth of hygroscopic droplets. *Trans. Faraday Soc.*, **32**, 1152–1161, https://doi.org/10.1039/TF9363201152.

Kollias, P., E. Luke, and K. Lamer, 2023: *Experiment of Sea Breeze Convection, Aerosols, Precipitation, and Environment (ESCAPE) C-band Radar Deployment Field Campaign Report*. U.S. Department of Energy, Atmospheric Radiation Measurement user facility, Richland, Washington,. DOI: 10.2172/2202258

Koren, I., G. Dagan, and O. Altaratz, 2014: From aerosol-limited to invigoration of warm convective clouds. *Science*, **344**, 1143–1146, https://doi.org/10.1126/science.1252595.

Korolev, A., 2007: Limitations of the Wegener–Bergeron–Findeisen Mechanism in the Evolution of Mixed-Phase Clouds. *Journal of the Atmospheric Sciences*, **64**, 3372–3375, https://doi.org/10.1175/JAS4035.1.

——, and G. Isaac, 2003: Phase transformation of mixed-phase clouds. *Q. J. R. Meteorol. Soc.*, **129**, 19–38, https://doi.org/10.1256/qj.01.203.

Korolev, A. V., M. P. Bailey, J. Hallett, and G. A. Isaac, 2004: Laboratory and In Situ Observation of Deposition Growth of Frozen Drops. *Journal of Applied Meteorology and Climatology*, **43**, 612–622, https://doi.org/10.1175/1520-0450(2004)043<0612:LAISOO>2.0.CO;2.

Lasher-Trapp, S., E. Jo, L. R. Allen, B. N. Engelsen, and R. J. Trapp, 2021: Entrainment in a Simulated Supercell Thunderstorm. Part I: The Evolution of Different Entrainment Mechanisms and Their Dilutive Effects. *Journal of the Atmospheric Sciences*, **78**, 2725–2740, https://doi.org/10.1175/JAS-D-20-0223.1.

Lau, K. M., and H. T. Wu, 2003: Warm rain processes over tropical oceans and climate implications. *Geophys. Res. Lett.*, **30**, https://doi.org/10.1029/2003GL018567.

Lawson, R. P., S. Woods, and H. Morrison, 2015: The Microphysics of Ice and Precipitation Development in Tropical Cumulus Clouds. *Journal of the Atmospheric Sciences*, **72**, 2429–2445, https://doi.org/10.1175/JAS-D-14-0274.1.

Lebo, Z. J., 2014: The Sensitivity of a Numerically Simulated Idealized Squall Line to the Vertical Distribution of Aerosols. *Journal of the Atmospheric Sciences*, **71**, 4581–4596, https://doi.org/10.1175/JAS-D-14-0068.1.

Lebo, Z. J., and H. Morrison, 2014: Dynamical Effects of Aerosol Perturbations on Simulated Idealized Squall Lines. *Monthly Weather Review*, **142**, 991–1009, https://doi.org/10.1175/MWR-D-13-00156.1.

Lee, S. S., L. J. Donner, V. T. J. Phillips, and Y. Ming, 2008: The dependence of aerosol effects on clouds and precipitation on cloud-system organization, shear and stability. *J. Geophys. Res. Atmospheres*, **113**, https://doi.org/10.1029/2007JD009224.

Lemon, L. R., and C. A. Doswell, 1979: Severe Thunderstorm Evolution and Mesocyclone Structure as Related to Tornadogenesis. *Monthly Weather Review*, **107**, 1184–1197, https://doi.org/10.1175/1520-0493(1979)107<1184:STEAMS>2.0.CO;2.

Lilly, D. K., 1962: On the numerical simulation of buoyant convection. Tellus, 14, 148–172, https://doi.org/10.1111/j.2153-3490.1962.tb00128.x.

Lilly, D. K., 1982: The Development and Maintenance of Rotation in Convective Storms. *Intense Atmospheric Vortices*, L. Bengtsson and J. Lighthill, Eds., Berlin, Heidelberg, Springer, 149–160. https://doi.org/10.1007/978-3-642-81866-0_12

——, 1983: Dynamics of Rotating Thunderstorms. *Mesoscale Meteorology — Theories, Observations and Models*, D.K. Lilly and T. Gal-Chen, Eds., Springer Netherlands, 531–543. https://doi.org/10.1007/978-94-017-2241-4_28

Lohmann, U., and J. Feichter, 2005: Global indirect aerosol effects: a review. *Atmospheric Chem. Phys.*, **5**, 715–737, https://doi.org/10.5194/acp-5-715-2005.

Maddox, R. A., 1980: Mesoscale Convective Complexes. *Bulletin of the American Meteorological Society*, **61**, 1374–1387, http://www.jstor.org/stable/26221473.

Marinescu, P. J., and Coauthors, 2021: Impacts of Varying Concentrations of Cloud Condensation Nuclei on Deep Convective Cloud Updrafts—A Multimodel Assessment. *J. Atmospheric Sci.*, **78**, 1147–1172, https://doi.org/10.1175/JAS-D-20-0200.1.

Markowski, P., and Y. Richardson, 2010: *Mesoscale Meteorology in Midlatitudes*. 1st ed. Wiley,.

Matthews, B. H., A. N. Alsante, and S. D. Brooks, 2023: Pollen Emissions of Subpollen Particles and Ice Nucleating Particles. *ACS Earth Space Chem.*, **7**, 1207–1218, https://doi.org/10.1021/acsearthspacechem.3c00014.

McCluskey, C. S., and Coauthors, 2018: A Mesocosm Double Feature: Insights into the Chemical Makeup of Marine Ice Nucleating Particles. *Journal of the Atmospheric Sciences*, **75**, 2405–2423, https://doi.org/10.1175/JAS-D-17-0155.1.

McGee, C. J., and S. C. van den Heever, 2014: Latent Heating and Mixing due to Entrainment in Tropical Deep Convection. *J. Atmospheric Sci.*, **71**, 816–832, https://doi.org/10.1175/JAS-D-13-0140.1.

Mendenhall, C. e., and L. r. Ingersoll, 1908: XVII. On certain phenomena exhibited by small particles on a Nernst glower. *Lond. Edinb. Dublin Philos. Mag. J. Sci.*, **15**, 205–214, https://doi.org/10.1080/14786440809463760.

Meyers, M. P., R. L. Walko, J. Y. Harrington, and W. R. Cotton, 1997: New RAMS cloud microphysics parameterization. Part II: The two-moment scheme. Atmospheric Research, 45, 3–39, https://doi.org/10.1016/S0169-8095(97)00018-5.

Miltenberger, A. K., S. Pfahl, and H. Wernli, 2013: An online trajectory module (version 1.0) for the nonhydrostatic numerical weather prediction model COSMO. *Geosci. Model Dev.*, **6**, 1989–2004, https://doi.org/10.5194/gmd-6-1989-2013.

Moroda, Y., K. Tsuboki, S. Satoh, K. Nakagawa, T. Ushio, and S. Shimizu, 2021: Structure and Evolution of Precipitation Cores in an Isolated Convective Storm Observed by Phased Array Weather Radar. *J. Meteorol. Soc. Jpn. Ser II*, **99**, 765–784, https://doi.org/10.2151/jmsj.2021-038.

Morris, C. E., D. G. Georgakopoulos, and D. C. Sands, 2004: Ice nucleation active bacteria and

their potential role in precipitation. *J. Phys. IV Proc.*, **121**, 87–103, https://doi.org/10.1051/jp4:2004121004.
Morris, C. E., F. Conen, J. Alex Huffman, V. Phillips, U. Pöschl, and D. C. Sands, 2014: Bioprecipitation: a feedback cycle linking Earth history, ecosystem dynamics and land use through biological ice nucleators in the atmosphere. *Glob. Change Biol.*, **20**, 341–351, https://doi.org/10.1111/gcb.12447.
Mossop, S. C., 1985: Secondary ice particle production during rime growth: The effect of drop size distribution and rimer velocity. *Q. J. R. Meteorol. Soc.*, **111**, 1113–1124, https://doi.org/10.1002/qj.49711147012.
——, A. Ono, and E. R. Wishart, 1970: Ice particles in maritime clouds near Tasmania. *Q. J. R. Meteorol. Soc.*, **96**, 487–508, https://doi.org/10.1002/qj.49709640910.
Mulholland, J. P., S. W. Nesbitt, and R. J. Trapp, 2019: A Case Study of Terrain Influences on Upscale Convective Growth of a Supercell. *Monthly Weather Review*, **147**, 4305–4324, https://doi.org/10.1175/MWR-D-19-0099.1.
Mulholland, J. P., J. M. Peters, and H. Morrison, 2021: How Does Vertical Wind Shear Influence Entrainment in Squall Lines? *Journal of the Atmospheric Sciences*, **78**, 1931–1946, https://doi.org/10.1175/JAS-D-20-0299.1.
Newson, R., D. Strachan, E. Archibald, J. Emberlin, P. Hardaker, and C. Collier, 1997: Effect of thunderstorms and airborne grass pollen on the incidence of acute asthma in England, 1990-94. *Thorax*, **52**, 680–685, https://doi.org/10.1136/thx.52.8.680.
Newton, C. W., 1950: STRUCTURE AND MECHANISM OF THE PREFRONTAL SQUALL LINE. *Journal of the Atmospheric Sciences*, **7**, 210–222, https://doi.org/10.1175/1520-0469(1950)007<0210:SAMOTP>2.0.CO;2.
Newton, C. W., and S. Katz, 1958: Movement of Large Convective Rainstorms in Relation to Winds Aloft. *Bulletin of the American Meteorological Society*, **39**, 129–136, https://doi.org/10.1175/1520-0477-39.3.129.
Patade, S., and Coauthors, 2022: The influence of multiple groups of biological ice nucleating particles on microphysical properties of mixed-phase clouds observed during MC3E. *Atmospheric Chem. Phys.*, **22**, 12055–12075, https://doi.org/10.5194/acp-22-12055-2022.
Packe, G. E., and Jon G. Ayres, 1985: ASTHMA OUTBREAK DURING A THUNDERSTORM. The Lancet, 326, 199–204, https://doi.org/10.1016/S0140-6736(85)91510-7.
Penner, J. E., and Coauthors, 2001: Aerosols, their direct and indirect effects. *Climate change 2001: the scientific basis. Contribution of working group I to the third assessment report of the intergovernmental panel on climate change*, Cambridge University Press, 289–348.
Pinsky, M., A. Khain, and A. Korolev, 2014: Analytical Investigation of Glaciation Time in Mixed-Phase Adiabatic Cloud Volumes. *Journal of the Atmospheric Sciences*, **71**, 4143–4157, https://doi.org/10.1175/JAS-D-13-0359.1.
Pope, F. D., 2010: Pollen grains are efficient cloud condensation nuclei. *Environ. Res. Lett.*, **5**, 044015, https://doi.org/10.1088/1748-9326/5/4/044015.
Pruppacher, H. R., and J. D. Klett, 2010: *Microphysics of Clouds and Precipitation*. Springer Netherlands,.
Riehl, H., and J. S. Malkus, 1958: On the Heat Balance in the Equatorial Trough Zone. Geophysica, 6, 503–538.
Rogers, D. C., P. J. DeMott, S. M. Kreidenweis, and Y. Chen, 1998: Measurements of ice nucleating aerosols during SUCCESS. *Geophys. Res. Lett.*, **25**, 1383–1386,

https://doi.org/10.1029/97GL03478.
Romps, D. M., K. Latimer, Q. Zhu, T. Jurkat-Witschas, C. Mahnke, T. Prabhakaran, R. Weigel, and M. Wendisch, 2023: Air Pollution Unable to Intensify Storms via Warm-Phase Invigoration. *Geophys. Res. Lett.*, **50**, e2022GL100409, https://doi.org/10.1029/2022GL100409.
Rosenfeld, D., U. Lohmann, G. B. Raga, C. D. O'Dowd, M. Kulmala, S. Fuzzi, A. Reissell, and M. O. Andreae, 2008: Flood or Drought: How Do Aerosols Affect Precipitation? *Science*, **321**, 1309–1313, https://doi.org/10.1126/science.1160606.
Rotunno, R., and J. B. Klemp, 1982: The Influence of the Shear-Induced Pressure Gradient on Thunderstorm Motion. *Monthly Weather Review*, **110**, 136–151, https://doi.org/10.1175/1520-0493(1982)110<0136:TIOTSI>2.0.CO;2.
——, and J. Klemp, 1985: On the Rotation and Propagation of Simulated Supercell Thunderstorms. *J. Atmospheric Sci.*, **42**, 271–292, https://doi.org/10.1175/1520-0469(1985)042<0271:OTRAPO>2.0.CO;2.
Rotunno, R., J. B. Klemp, and M. L. Weisman, 1988: A Theory for Strong, Long-Lived Squall Lines. *Journal of the Atmospheric Sciences*, **45**, 463–485, https://doi.org/10.1175/1520-0469(1988)045<0463:ATFSLL>2.0.CO;2.
Rotunno, R., P. M. Markowski, and G. H. Bryan, 2017: "Near Ground" Vertical Vorticity in Supercell Thunderstorm Models. *Journal of the Atmospheric Sciences*, **74**, 1757–1766, https://doi.org/10.1175/JAS-D-16-0288.1.
Saleeby, S. M., and W. R. Cotton, 2004: A Large-Droplet Mode and Prognostic Number Concentration of Cloud Droplets in the Colorado State University Regional Atmospheric Modeling System (RAMS). Part I: Module Descriptions and Supercell Test Simulations. J. Appl. Meteor., 43, 182–195, https://doi.org/10.1175/1520-0450(2004)043<0182:ALMAPN>2.0.CO;2.
Saleeby, S. M., and S. C. van den Heever, 2013: Developments in the CSU-RAMS Aerosol Model: Emissions, Nucleation, Regeneration, Deposition, and Radiation. *J. Appl. Meteorol. Climatol.*, **52**, 2601–2622, https://doi.org/10.1175/JAMC-D-12-0312.1.
Saleeby, S. M., S. R. Herbener, S. C. van den Heever, and T. L'Ecuyer, 2015: Impacts of Cloud Droplet–Nucleating Aerosols on Shallow Tropical Convection. *Journal of the Atmospheric Sciences*, **72**, 1369–1385, https://doi.org/10.1175/JAS-D-14-0153.1.
Schlesinger, R. E., 1978: A Three-Dimensional Numerical Model of an Isolated Thunderstorm: Part I. Comparative Experiments for Variable Ambient Wind Shear. *Journal of the Atmospheric Sciences*, **35**, 690–713, https://doi.org/10.1175/1520-0469(1978)035<0690:ATDNMO>2.0.CO;2.
Seigel, R. B., and S. C. van den Heever, 2012: Dust Lofting and Ingestion by Supercell Storms. *Journal of the Atmospheric Sciences*, **69**, 1453–1473, https://doi.org/10.1175/JAS-D-11-0222.1.
——, and ——, 2013: Squall-Line Intensification via Hydrometeor Recirculation. *J. Atmospheric Sci.*, **70**, 2012–2031, https://doi.org/10.1175/JAS-D-12-0266.1.
Seigel, R. B., S. C. van den Heever, and S. M. Saleeby, 2013: Mineral dust indirect effects and cloud radiative feedbacks of a simulated idealized nocturnal squall line. *Atmospheric Chem. Phys.*, **13**, 4467–4485, https://doi.org/10.5194/acp-13-4467-2013.
Seiki, T., and T. Nakajima, 2014: Aerosol Effects of the Condensation Process on a Convective Cloud Simulation. *Journal of the Atmospheric Sciences*, **71**, 833–853, https://doi.org/10.1175/JAS-D-12-0195.1.

Shabbott, C. J., and P. M. Markowski, 2006: Surface In Situ Observations within the Outflow of Forward-Flank Downdrafts of Supercell Thunderstorms. *Monthly Weather Review*, **134**, 1422–1441, https://doi.org/10.1175/MWR3131.1.

Sheffield, A. M., S. M. Saleeby, and S. C. van den Heever, 2015: Aerosol-induced mechanisms for cumulus congestus growth. *J. Geophys. Res. Atmospheres*, **120**, 8941–8952, https://doi.org/10.1002/2015JD023743.

Simpson, J. E., 1969: A comparison between laboratory and atmospheric density currents. *Q. J. R. Meteorol. Soc.*, **95**, 758–765, https://doi.org/10.1002/qj.49709540609.

Smagorinsky, J., 1963: GENERAL CIRCULATION EXPERIMENTS WITH THE PRIMITIVE EQUATIONS. *Monthly Weather Review*, **91**, 99–164, https://doi.org/10.1175/1520-0493(1963)091<0099:GCEWTP>2.3.CO;2.

Smull, B. F., and R. A. Houze, 1987: Rear Inflow in Squall Lines with Trailing Stratiform Precipitation. *Monthly Weather Review*, **115**, 2869–2889, https://doi.org/10.1175/1520-0493(1987)115<2869:RIISLW>2.0.CO;2.

Solomos, S., G. Kallos, E. Mavromatidis, and J. Kushta, 2012: Density currents as a desert dust mobilization mechanism. *Atmospheric Chem. Phys.*, **12**, 11199–11211, https://doi.org/10.5194/acp-12-11199-2012.

Stier, P., and Coauthors, 2024: Multifaceted aerosol effects on precipitation. *Nat. Geosci.*, **17**, 719–732, https://doi.org/10.1038/s41561-024-01482-6.

Stone, E. A., C. B. A. Mampage, D. D. Hughes, and L. M. Jones, 2021: Airborne sub-pollen particles from rupturing giant ragweed pollen. *Aerobiologia*, **37**, 625–632, https://doi.org/10.1007/s10453-021-09702-x.

Storer, R. L., and S. C. van den Heever, 2013: Microphysical Processes Evident in Aerosol Forcing of Tropical Deep Convective Clouds. *Journal of the Atmospheric Sciences*, **70**, 430–446, https://doi.org/10.1175/JAS-D-12-076.1.

——, S. C. Van Den Heever, and G. L. Stephens, 2010: Modeling Aerosol Impacts on Convective Storms in Different Environments. *J. Atmospheric Sci.*, **67**, 3904–3915, https://doi.org/10.1175/2010JAS3363.1.

Storer, R. L., S. C. Van Den Heever, and T. S. L'Ecuyer, 2014: Observations of aerosol-induced convective invigoration in the tropical east Atlantic. *J. Geophys. Res. Atmospheres*, **119**, 3963–3975, https://doi.org/10.1002/2013JD020272.

Subba, T., Y. Zhang, and A. L. Steiner, 2023: Simulating the Transport and Rupture of Pollen in the Atmosphere. *J. Adv. Model. Earth Syst.*, **15**, e2022MS003329, https://doi.org/10.1029/2022MS003329.

Sun, J., and P. A. Ariya, 2006: Atmospheric organic and bio-aerosols as cloud condensation nuclei (CCN): A review. *Atmos. Environ.*, **40**, 795–820, https://doi.org/10.1016/j.atmosenv.2005.05.052.

Szoke, E. J., and E. J. Zipser, 1986: A Radar Study of Convective Cells in Mesoscale Systems in GATE. Part II: Life Cycles of Convective Cells. *Journal of the Atmospheric Sciences*, **43**, 199–218, https://doi.org/10.1175/1520-0469(1986)043<0199:ARSOCC>2.0.CO;2.

Tao, W.-K., X. Li, A. Khain, T. Matsui, S. Lang, and J. Simpson, 2007: Role of atmospheric aerosol concentration on deep convective precipitation: Cloud-resolving model simulations. *J. Geophys. Res. Atmospheres*, **112**, https://doi.org/10.1029/2007JD008728.

——, J.-P. Chen, Z. Li, C. Wang, and C. Zhang, 2012: Impact of aerosols on convective clouds and precipitation. *Rev. Geophys.*, **50**, https://doi.org/10.1029/2011RG000369.

Taylor, P. E., R. C. Flagan, R. Valenta, and M. M. Glovsky, 2002: Release of allergens as

respirable aerosols: A link between grass pollen and asthma. *J. Allergy Clin. Immunol.*, **109**, 51–56, https://doi.org/10.1067/mai.2002.120759.
Testa, B., and Coauthors, 2021: Ice Nucleating Particle Connections to Regional Argentinian Land Surface Emissions and Weather During the Cloud, Aerosol, and Complex Terrain Interactions Experiment. *J. Geophys. Res. Atmospheres*, **126**, e2021JD035186, https://doi.org/10.1029/2021JD035186.
Tobo, Y., and Coauthors, 2013: Biological aerosol particles as a key determinant of ice nuclei populations in a forest ecosystem. *J. Geophys. Res. Atmospheres*, **118**, https://doi.org/10.1002/jgrd.50801.
Tompkins, A. M., 2001: Organization of Tropical Convection in Low Vertical Wind Shears: The Role of Cold Pools. *Journal of the Atmospheric Sciences*, **58**, 1650–1672, https://doi.org/10.1175/1520-0469(2001)058<1650:OOTCIL>2.0.CO;2.
Tulet, P., K. Crahan-Kaku, M. Leriche, B. Aouizerats, and S. Crumeyrolle, 2010: Mixing of dust aerosols into a mesoscale convective system: Generation, filtering and possible feedbacks on ice anvils. *Atmospheric Res.*, **96**, 302–314, https://doi.org/10.1016/j.atmosres.2009.09.011.
Twohy, C. H., and M. R. Poellot, 2005: Chemical characteristics of ice residual nuclei in anvil cirrus clouds: evidence for homogeneous and heterogeneous ice formation. *Atmospheric Chem. Phys.*, **5**, 2289–2297, https://doi.org/10.5194/acp-5-2289-2005.
Twohy, C. H., and Coauthors, 2009: Saharan dust particles nucleate droplets in eastern Atlantic clouds. *Geophys. Res. Lett.*, **36**, 2008GL035846, https://doi.org/10.1029/2008GL035846.
Twomey, S., 1977: The Influence of Pollution on the Shortwave Albedo of Clouds. *Journal of the Atmospheric Sciences*, **34**, 1149–1152, https://doi.org/10.1175/1520-0469(1977)034<1149:TIOPOT>2.0.CO;2.
——, and P. Squires, 1959: The Influence of Cloud Nucleus Population on the Microstructure and Stability of Convective Clouds. *Tellus*, **11**, 408–411, https://doi.org/10.3402/tellusa.v11i4.9331.
Uebel, M., and A. Bott, 2015: Mesoscale air transport at a midlatitude squall line in Europe – a numerical analysis. *Q. J. R. Meteorol. Soc.*, **141**, 3297–3311, https://doi.org/10.1002/qj.2610.
Vali, G., 1971: Quantitative Evaluation of Experimental Results an the Heterogeneous Freezing Nucleation of Supercooled Liquids. *Journal of the Atmospheric Sciences*, **28**, 402–409, https://doi.org/10.1175/1520-0469(1971)028<0402:QEOERA>2.0.CO;2.
Varble, A., 2018: Erroneous Attribution of Deep Convective Invigoration to Aerosol Concentration. *Journal of the Atmospheric Sciences*, **75**, 1351–1368, https://doi.org/10.1175/JAS-D-17-0217.1.
Varble, A. C., A. L. Igel, H. Morrison, W. W. Grabowski, and Z. J. Lebo, 2023: Opinion: A critical evaluation of the evidence for aerosol invigoration of deep convection. *Atmospheric Chem. Phys.*, **23**, 13791–13808, https://doi.org/10.5194/acp-23-13791-2023.
Vonnegut, B., 1948: Variation with temperature of the nucleation rate of supercooled liquid tin and water drops. *J. Colloid Sci.*, **3**, 563–569, https://doi.org/10.1016/S0095-8522(48)90049-X.
Wakimoto, R. M., 1982: The Life Cycle of Thunderstorm Gust Fronts as Viewed with Doppler Radar and Rawinsonde Data. *Monthly Weather Review*, **110**, 1060–1082, https://doi.org/10.1175/1520-0493(1982)110<1060:TLCOTG>2.0.CO;2.
Wang, C., 2005: A modeling study of the response of tropical deep convection to the increase of

cloud condensation nuclei concentration: 1. Dynamics and microphysics. *J. Geophys. Res. Atmospheres*, **110**, https://doi.org/10.1029/2004JD005720.

Weisman, M. L., 1992: The Role of Convectively Generated Rear-Inflow Jets in the Evolution of Long-Lived Mesoconvective Systems. *Journal of the Atmospheric Sciences*, **49**, 1826–1847, https://doi.org/10.1175/1520-0469(1992)049<1826:TROCGR>2.0.CO;2.

Weisman, M. L., and J. B. Klemp, 1982: The Dependence of Numerically Simulated Convective Storms on Vertical Wind Shear and Buoyancy. *Mon. Weather Rev.*, **110**, 504–520, https://doi.org/10.1175/1520-0493(1982)110<0504:TDONSC>2.0.CO;2.

Weisman, M. L., and J. B. Klemp, 1984: The Structure and Classification of Numerically Simulated Convective Stormsin Directionally Varying Wind Shears. *Mon. Weather Rev.*, **112**, 2479–2498, https://doi.org/10.1175/1520-0493(1984)112<2479:TSACON>2.0.CO;2.

——, and R. Rotunno, 2004: "A Theory for Strong Long-Lived Squall Lines" Revisited. *J. Atmospheric Sci.*, **61**, 361–382, https://doi.org/10.1175/1520-0469(2004)061<0361:ATFSLS>2.0.CO;2.

Weisman, M. L., J. B. Klemp, and R. Rotunno, 1988: Structure and Evolution of Numerically Simulated Squall Lines. *Journal of the Atmospheric Sciences*, **45**, 1990–2013, https://doi.org/10.1175/1520-0469(1988)045<1990:SAEONS>2.0.CO;2.

——, W. C. Skamarock, and J. B. Klemp, 1997: The Resolution Dependence of Explicitly Modeled Convective Systems. *Mon. Weather Rev.*, **125**, 527–548, https://doi.org/10.1175/1520-0493(1997)125<0527:TRDOEM>2.0.CO;2.

Werchner, S., E. Gute, C. Hoose, Ch. Kottmeier, A. Pauling, H. Vogel, and B. Vogel, 2022: When Do Subpollen Particles Become Relevant for Ice Nucleation Processes in Clouds? *J. Geophys. Res. Atmospheres*, **127**, e2021JD036340, https://doi.org/10.1029/2021JD036340.

Wernli, H., and H. C. Davies, 1997: A Lagrangian-based analysis of extratropical cyclones. I: The method and some applications. *Q. J. R. Meteorol. Soc.*, **123**, 467–489, https://doi.org/10.1002/qj.49712353811.

Wilhelmson, R., 1974: The Life Cycle of a Thunderstorm in Three Dimensions. *Journal of the Atmospheric Sciences*, **31**, 1629–1651, https://doi.org/10.1175/1520-0469(1974)031<1629:TLCOAT>2.0.CO;2.

Wozniak, M. C., F. Solmon, and A. L. Steiner, 2018: Pollen Rupture and Its Impact on Precipitation in Clean Continental Conditions. *Geophys. Res. Lett.*, **45**, 7156–7164, https://doi.org/10.1029/2018GL077692.

Xie, W., Y. Li, W. Bai, J. Hou, T. Ma, X. Zeng, L. Zhang, and T. An, 2020: The source and transport of bioaerosols in the air: A review. *Front. Environ. Sci. Eng.*, **15**, 44, https://doi.org/10.1007/s11783-020-1336-8.

Yang, J., Z. Wang, A. J. Heymsfield, and J. R. French, 2016: Characteristics of vertical air motion in isolated convective clouds. *Atmospheric Chem. Phys.*, **16**, 10159–10173, https://doi.org/10.5194/acp-16-10159-2016.

Zhang, Y., and A. L. Steiner, 2022: Projected climate-driven changes in pollen emission season length and magnitude over the continental United States. *Nat. Commun.*, **13**, 1234, https://doi.org/10.1038/s41467-022-28764-0.

——, T. Subba, B. H. Matthews, C. Pettersen, S. D. Brooks, and A. L. Steiner, 2024: Effects of Pollen on Hydrometeors and Precipitation in a Convective System. *J. Geophys. Res. Atmospheres*, **129**, e2023JD039891, https://doi.org/10.1029/2023JD039891.